ANALYSIS OF SIDE END PRESSURIZED BUMP TYPE GAS FOIL BEARINGS: A MODEL ANCHORED TO TEST DATA

A Dissertation

by

TAE HO KIM

Submitted to the Office of Graduate Studies of
Texas A&M University
in partial fulfillment of the requirements for the degree of

DOCTOR OF PHILOSOPHY

December 2007

Major Subject: Mechanical Engineering

ANALYSIS OF SIDE END PRESSURIZED BUMP TYPE GAS FOIL BEARINGS: A MODEL ANCHORED TO TEST DATA

A Dissertation

by

TAE HO KIM

Submitted to the Office of Graduate Studies of
Texas A&M University
in partial fulfillment of the requirements for the degree of

DOCTOR OF PHILOSOPHY

Approved by:

Chair of Committee,	Luis San Andrés
Committee Members,	Dara W. Childs
	Daejong Kim
	Carl Pearcy
Head of Department,	Dennis L. O'Neal

December 2007

Major Subject: Mechanical Engineering

ABSTRACT

Analysis of Side End Pressurized Bump Type Gas Foil Bearings: A Model
Anchored to Test Data. (December 2007)
Tae Ho Kim, B.S., Hanyang University in Seoul;
M.S., Hanyang University
Chair of Advisory Committee: Dr. Luis San Andrés

Comprehensive modeling of gas foil bearings (GFBs) anchored to reliable test data will enable the widespread usage of GFBs into novel turbomachinery applications, such as light weight business aircraft engines, hybrid fuel cell-turbine power systems, and micro-engines recharging battery packs for clean hybrid electric vehicles. Pressurized air is often needed to cool GFBs and to carry away heat conducted from a hot turbine in oil-free micro turbomachinery. Side end pressurization, however, demonstrates a profound effect on the rotordynamic performance of GFBs. This dissertation presents the first study that devotes considerable attention to the effect of side end pressurization on delaying the onset rotor speed of subsynchronous motions.

GFB performance depends largely on the support elastic structure, i.e. a smooth foil on top of bump strips. The top foil on bump strips layers is modeled as a two dimensional (2D), finite element (FE) shell supported on axially distributed linear springs. The structural model is coupled to a unique model of the gas film governed by modified Reynolds equation with the evolution of gas flow circumferential velocity, a function of the side end pressure. Predicted direct stiffness and damping increase as the pressure raises, while the difference in cross-coupled stiffnesses, directly related to rotor-bearing system stability, decreases. Prediction also shows that side end pressurization delays the threshold speed of instability.

Dynamic response measurements are conducted on a rigid rotor supported on GFBs. Rotor speed-up tests first demonstrate the beneficial effect of side end pressurization on delaying the onset speed of rotor subsynchronous motions. The test data are in agreement with predictions of threshold speed of instability and whirl frequency ratio, thus validating the model of GFBs with side end pressurization. Rotor speed coastdown tests at a low pressure of 0.35 bar evidence nearly uniform normalized rotor motion amplitudes and phase angles with small and moderately large imbalance masses, thus implying a linear rotor response behavior.

A finite element rotordynamic model integrates the linearized GFB force coefficients to predict the synchronous responses of the test rotor. A comparison of predictions to test data demonstrates an excellent agreement and successfully validates the rotordynamic model.

DEDICATION

To my wife Eunsu and children Seohyeon and Seoin, for their love and sacrifice,
my parents, for their love, advice, and support,
my sister Jin Sil and brother Tae Young, for their encouragement,
and all my friends for their friendship.

"I never had a policy; I have just tried to do my very best each and every day"

- Abraham Lincoln

ACKNOWLEDGEMENTS

I would like to thank my academic advisor, Dr. Luis San Andrés for his guidance and support. His words of encouragement are greatly appreciated. Thank Dr. Dara W. Childs for the many valuable recommendations and comments and to Daejong Kim and Dr. Carl Pearcy, members of my advisory committee, for their time and interest.

Thanks to Dario Rubio for setting up the original experimental facility. The technical support from Mr. Eddy Denk and Adolfo Delgado is very much appreciated. Sincere thanks to Keun Ryu, Sang Hyeon Park, and Anthony Breedlove for their kind discussion on this research at times.

I acknowledge the friendship and support of my friends, Yeonseok Kim, Kyuho Shim, Christopher Sparks, Hyeokjin Oh, Juhoon Kim, Dongkeun Kim, Clint Carter, and other friends at the Turbomachinery Laboratory.

This material is based upon work supported by the National Science Foundation (NSF) under Grant 0322925 and Turbomachinery Research Consortium (TRC). I also acknowledge the scholarship awarded by Korea Science and Engineering Foundation (KOSEF).

TABLE OF CONTENTS

Page

CHAPTER

LIST OF FIGURES

Page

Page

Page

Page

Page

Page

Page

LIST OF TABLES

NOMENCLATURE

$C_{\alpha\beta}$	Damping coefficients; $\alpha,\beta = X,Y$ [N·s/m]
C_{eff}	Effective damping coefficient[N·s/m]
c	Nominal radial clearance [m]
c_J	Measured journal radial travel [m]
c_m	Assembly radial clearance [m]
c_{DE} , c_{FE}	Nominal radial clearance for the drive and free end GFBs, respectively [m]
D	Top foil (bearing) diameter, $D = 2\times R$ [m]
DV, DH	Drive end bearing, vertical and horizontal planes
E	Top foil elastic modulus [Pa] or [N/ m^2]
e_X, e_Y	Journal eccentricity component [m], $e=\sqrt{e_X^2+e_Y^2}$
FV, FH	Free end bearing, vertical and horizontal planes
F^e , F^G	FE element nodal force vector and global nodal force vector
f^1	Normal load vector for a four-node finite shell element.
g	Gravity
h	Gas film thickness [m]
h_t	Shell thickness [m]
h_b	Bump height [m]
I	Moment of inertia [m^4]
i	Imaginary unit, $\sqrt{-1}$
j	Node number along circumferential direction
K^e, K^G	FE top foil element stiffness matrix and global nodal stiffness matrix
K^s	FE bump element stiffness matrix
K_{eff}	Effective stiffness coefficient [N/m]
K_f	Structural stiffness per unit area [N/m^3]
K'_f	Complex structural stiffness per unit area, $K'_f = K_f\left(1+i\gamma\right)$ [N/m^3]
K_l	Structural stiffness per unit bump element [N/m]

$K_{\alpha\beta}$	Stiffness coefficients; $\alpha,\beta = X,Y$ [N/m]
k	Node number along the axial direction
k^{ij}	Stiffness matrices for a four-node finite element plate stiffness matrix
k_t	Shear correction coefficient (=5/6) in a shear deformable plate model [-]
L	Bearing axial width [m]
l_x	Pad circumferential length, $R(\Theta_t - \Theta_l)$ [m]
l_0	Half bump length [m]
l_{ex}	FE thin foil length in the circumferential direction [m]
l_{ey}	FE thin foil length in the axial direction [m]
M	Fraction of the rotor mass that each bearing supports [kg]
M_{MN}	Bending moment per unit element length in a thin shell [N]
m_e	Mass imbalance [mg]
$m^{1,2}$	bending moment vectors for a four-node finite shell element
$\dot{m}_z$	axial flow rate through the film [m^3/s]
N_{MN}	Membrane or in-plane force per unit element length in a thin shell [N/m]
N_b	Number of bumps [-]
N_{os}	Onset speed of subsynchronous rotor motions [rpm]
p	Hydrodynamic pressure in gas film [Pa]
p_a	Ambient pressure [Pa]
p_A	Average pressure along axial direction [Pa]
p_s	End gas pressure [N/m^2]
p_{sub}	Gas pressure in outer gap [N/m^2]
Q_m	Shear force per unit element length in a thin shell [N/m]
$Q^e_{1,2}$	Shear forces at the boundary of a FE element
$Q^e_{3,4}$	Bending moments at the boundary of a FE element
q	Transversely distributed load [N/m^2].
R	Top foil (bearing) radius [m]
r	Radius for location of imbalance masses [m]

r_P	Preload on bearing [m]
S_{fa} , S_{fc}	Stiffening factors for elastic modulus in the axial and circumferential directions [-]
s_0	Bump pitch [m]
T	Temperature [K]
t	Time [s]
t_b	Bump foil thickness [m]
t_t	Top (thin) foil thickness [m]
U^e , U^G	FE nodal displacement vector and global nodal displacement vector
u	Shell circumferential displacement (x direction)
u_c	Mean circumferential flow velocity [m/s]
u_e	$m_e\, r/M$, Imbalance displacement [μm]
u^e	FE nodal displacement
w_d	top foil transverse deflection [m]
X,Y	Coordinate system for the inertial axes [m]
x,z	Coordinate system on plane of bearing [m]
α	Inlet flow pre-swirl factor
ϕ_x , ϕ_y	Shell rotation angles about the y and x axes
Φ	Journal attitude angle, $\tan^{-1}(e_x/e_y)$ [rad]
γ	Structural damping loss factor [-]
μ	Gas viscosity [Pa-s]
v	Shell axial displacement (y direction)
$v_{1,2}$	Weight function for FE formulae
v_p	Poisson's ratio [-]
ψ^e	Hermite cubic interpolation function
$\Re$	Ideal gas constant [J/Kg-K]
Θ	Top foil angular coordinate [rad]
Θ_p	Preload offset position [rad]

Ω	Rotor angular velocity [rad]
$\Omega_{threshold}$	Threshold speed of instability [Hz]
ω	Whirl frequency [rad]
ω_{cr}	Critical speed [rad/s]
$\omega_{threshold}$	Whirl frequency of unstable motions[Hz]
ω_n	Natural frequency of system [Hz]
ξ	Damping ratio [-]
WFR	$\omega_{threshold} / \Omega_{threshold}$ .Whirl frequency ratio [-]

Subscripts

$\alpha, \beta = X, Y$	Directions of perturbation for first order pressure fields
$M, N = x, y$	Directions of shell membrane and moment force

Superscripts

α, β	Directions of perturbation for first order pressure fields (X, Y)
i,j =1-3	Row and column numbers for a four-node finite element plate stiffness matrix
DE,FE	Rotor drive and free end, respectively.

CHAPTER I

INTRODUCTION

Implementing gas foil bearings (GFBs) in micro turbomachinery reduces system complexity and maintenance costs, and increases efficiency and operating life [1,2]. Since the 1960s, tension tape GFBs and multiple leaf GFBs with and without backing springs, as well as corrugated bump GFBs, have been implemented as low friction supports in oil-free (small size) rotating machinery. In comparison to rolling element bearings and for operation with high surface speeds, both leaf GFBs and bump GFBs have demonstrated superior reliability in Air Cycle Machines (ACMs) of aircraft environmental control systems [3-6], for example. Figure 1 depicts two typical GFB configurations; one is a multiple-leaf type bearing and the other is a corrugated-bump-strip type bearing.

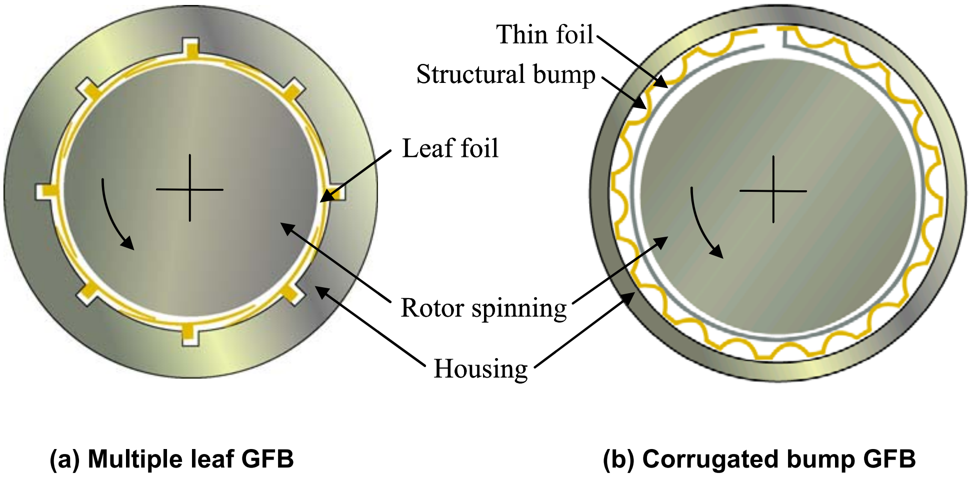

Figure 1 Schematic views of two typical gas foil bearing.

Gas foil bearings (GFBs) are compliant-surface hydrodynamic bearings that use ambient air or any process gas as the lubricating fluid. A hydrodynamic pressure builds up within the small gap or film between the rotating shaft and the smooth foil. In

---

This dissertation follows the style of the ASME Journal of Engineering for Gas Turbines and Power.

multiple leaf GFBs, the compliance to bending from staggered structural foils and the dry-friction at the contact lines define their operational characteristics [5]. In corrugated bump GFBs, bump-strip layers supporting a (thin) top foil render a tunable support. In this type of bearing, dry-friction effects arising between the bumps and top foil and the bumps and the bearing inner surface provide the energy dissipation or damping characteristics [6]. The published literature notes that multiple leaf GFBs are not the best supports in high performance turbomachinery, primarily because of their inherently low load capacity [6]. A corrugated bump type GFB fulfills most of the requirements of highly efficient oil-free turbomachinery, with demonstrated ultimate load capacity up to 680 kPa (100 psi) [7, 8].

The forced performance of a GFB depends upon the material properties and geometrical configuration of its support structure (the top foil and bump strip layers), as well as the hydrodynamic film pressure generated within the bearing clearance. In particular, the underlying support structure dominates the static and dynamic performance of high speed heavily loaded GFBs [9]. For example, due to the elastic deflection of the bump strip layers, GFBs show relatively small changes in film thickness as compared to those in journal eccentricity. The GFB overall stiffness depends mainly on the softer support structure, rather than on that of the gas film, which "hardens" as the shaft speed and applied load increase. Material hysteresis and dry-friction dissipation mechanisms between the bumps and top foil, as well as between the bumps and the bearing inner surface, appear to enhance the bearing damping [10].

Comprehensive modeling of GFBs anchored to relevant test data will enable the widespread usage of GFBs into novel turbomachinery applications, such as hybrid fuel cell-turbine power systems and micro-engines recharging battery packs for clean hybrid electric vehicles [11,12]. Engineered GFBs must have a dimensionless load capacity larger than unity, i.e. specific pressure $(W/LD)/\,p_a > 1$ [13]. Modeling of GFBs is difficult due to the mechanical complexity of the bump strip layers and top foil structure, further aggravated by the lack of simple, though physically realistic, energy dissipation models at the contact surfaces where dry-friction is prevalent.

The static load capacity and dynamic forced performance of GFBs depends largely on the material properties of the support elastic structure, i.e. a smooth foil on top of bump strips. Conventional models include only the bumps as an equivalent stiffness uniformly distributed around the bearing circumference. More complex models couple directly the elastic deformations of the top foil to the bump underlying structure as well as to the hydrodynamics of the gas film.

Introducing mechanical preloads into GFBs enhances the hydrodynamic wedge to generate a pressure field, producing a centering stiffness even in the absence of an applied static load [14]. Mechanical preloads can be given to GFBs with a differential height of the elastic support, by introducing "lobe" shape inner profile of the machined GFB bore, or by performing the top foil and elastic support layers to have larger radius of curvature than that of the GFB bore [14,15]. However, the easiest and most cost effective way is by inserting metal shims underneath a bump strip and in contact with the bearing housing [14].

In addition to heat conduction through the support structure consisting of the top foil and elastic support layers, GFBs often need a cooling gas flow, axially fed through one end of the bearing, to transport the heat conducted from a hot turbine, for example [16]. Introducing the cooling flow prevents hot-spots in the GFB and extends its life. End gas pressurization, however, shows a paramount effect on reducing amplitudes of motion, synchronous and subsynchronous [17].

Chapter II discusses previous works related to (1) predictive models of bump-type GFBs, (2) underlying structural bump models and experimental investigations, (3) rotordynamic response measurements of a rotor supported on GFBs, (4) rotordynamic parameter identifications, (5) high temperature operations of GFBs, and (6) models of GFBs with side end pressurization.

Chapter III details a 2D FE anisotropic shell model for the top foil supported on bump strips. Computationally effective simpler model, i.e. a 1D beam-like structure is also introduced. Top foil models are integrated with the bump strip layers and in conjunction with the hydrodynamic gas film to predict the static and dynamic load performance of GFBs. The Cholesky decomposition of the stiffness matrix representing the top foil and bump strips is performed off-line prior to computations coupling it to the gas film analysis governed by Reynolds equation. The procedure greatly enhances the computational efficiency of the numerical scheme. Predictions for two types of top foil structures, one and two dimensional, are compared for validation to limited test results available in the literature.

Chapter IV describes experimental results of the rotordynamic performance of a rotor supported on two GFBs with side end pressurization. Installation of three metal shims into GFBs reveals the effect of mechanical preload on the dynamic performance. A series of rotor speed-up tests to 50 krpm identify the onset speeds of subsynchronous motion for GFBs with side end pressurization. Phase angle and amplitude of synchronous rotor responses for increasing in-phase and out-of-phase imbalance masses are recorded during coastdown tests. Normalization[1] of the rotor amplitudes after baseline subtraction aids to evaluate the linearity of the rotor – GFB system. A single degree of freedom model estimates the effective stiffness and damping coefficients from the measured rotor responses. Rotor speed versus time data obtained during rotor coastdown tests serves to identify speed ranges where "viscous" drag is dominant.

Chapter V presents a physical model for prediction of the forced performance of GFBs supplied with end gas pressurization. The gas film model includes the evolution of gas circumferential velocity as a function of the imposed side end pressure. The gas film equation for hydrodynamic pressure generation is coupled to the 2D FE structural model developed in Chapter III. A simple stability analysis [18] gives the rotordynamic characteristics of the test GFB with side end pressurization. The predicted threshold speed of instability is in close agreement with test measurements.

---

[1] The normalization procedure multiplies a recorded amplitude response by the ratio of the smallest imbalance mass to the actual imbalance mass.

A model for GFBs with machined mechanical preload predicts the performance of shimmed GFBs. A sinusoidal function approximately depicts the assembly radial clearance modified due to installation of three shims. The shimmed GFB generates significant hydrodynamic pressures with peaks at the three shim locations, while the original GFB shows much lower film pressures. Installation of shims into the GFBs leads to an increase in direct stiffness and damping coefficients. Changes in cross-coupled force coefficients are relatively small.

A linear finite element rotordynamic analysis (XLTRC2®) models the test rotor supported on GFBs and predicts the system rotordynamic stability and synchronous rotor responses. The predicted amplitude and phase angle of the synchronous responses show good agreement with the test measurements recorded during rotor coastdown tests with small to moderate imbalance masses.

CHAPTER II

LITERATURE REVIEW

In 1953 Blok and van Rossum [19] introduced the concept of Foil Bearings (FBs). The authors point out that a foil bearing film thickness, larger than that of rigid gas bearings, can improve operational reliability and provide a solution for problems related to thermal expansion of both a journal and its bearing. Field experience has proved, since the late 1960's, that Gas Foil Bearings (GFBs) are far more reliable than ball bearings previously used in Air Cycle Machines (ACMs) installed in aircrafts. Therefore, GFBs have since been used in almost every new ACM installed in both civil and military aircraft [1]. Implementation of GFBs into high performance turbomachinery applications demands accuracy in modeling capabilities. This literature review discusses previously published works regarding bump type GFB models and relevant experimental tests.

Predictive GFB Models

Heshmat et al. [9,20] first present analyses of bump type GFBs and detail the bearings static load performance. The predictive model couples the gas film hydrodynamic pressure (p) generation to a local deflection (w_d) of the support bumps. In this simplest of all models, the top foil is altogether neglected and the elastic displacement, $w_d = \alpha\ (p\text{-}p_a)$, is proportional to the local pressure difference ($p\text{-}p_a$) through a structural compliance (α) coefficient which depends on the bump material, thickness and geometric configuration. This model, ubiquitous in the literature of GFBs, is hereby named as the *simple elastic foundation model*.

Peng and Carpino [21,22] present finite difference formulations to calculate the linearized stiffness and damping force coefficients of GFBs. The model integrates both fluid (gas) film and structural bump equivalent stiffness to simultaneously solve the Reynolds equation. In the model of the underlying foil structure, a perfectly extensible foil is placed on top of the corrugated bumps. In [22], the model includes the equivalent viscous damping of dry-friction between the bumps and the bearing housing. As the dry-friction coefficient increases, the direct damping coefficients significantly increase.

Iordanoff [23] introduces a simple method of enabling the rapid design of thrust GFBs. The model is based on results obtained with rigid gas bearing profiles and determines an optimum compliant profile to produce a maximum load capacity, i.e. the determined optimum pressures and film thicknesses for rigid gas bearings render the gas film profile for GFBs by using a compliance parameter. Therefore, this unique model does not use the iterative numerical scheme to find simultaneous solutions for the Reynolds equations and a simple equation for the gas film thickness of GFBs, thus significantly reducing computational cost. The proposed simple formulations calculate the compliance parameters for both the welded and the free bumps of the GFBs. This method is successfully applied to the design of an 80 mm outer diameter - 40 mm inner diameter thrust bearing, which shows a greatly improved load capacity when compared to previously reported configurations. Note that this unique method is presently considered valid only for thrust GFBs with a specified operating rotor speed.

San Andrés [10] presents an analysis of the turbulent bulk-flow of a cryogenic liquid foil bearing (FB) for turbopump applications. The model uses an axially averaged pressure to couple the flow field to the structural bump deflection. An example of a three pad liquid oxygen FB is taken directly from the literature [24]. The foil structure model consists of a complex structural stiffness with a structural loss factor arising from material hysteresis and dry-frictional effects between the bumps and top foil, and the bumps and the bearing’s inner surface. The predictions show that the liquid oxygen FB reduces the undesirable cross-coupled stiffness coefficients and gets rid of potentially harmful half rotating frequency whirl. This paper reveals an important advantage of the FB that it has nearly uniform force coefficients and increasing damping coefficients at low excitation frequencies.

Carpino et al. [25-28] have advanced the most complete computational models to date, including detailed descriptions of membrane and bending effects of the top foil, and accounting for the sub-foil structure elastic deformation. In [25,26], the authors build FE models for the gas film and the foil structure, couple both models through the pressure field and get solutions using an iterative numerical scheme. The bending and membrane rigidity terms of the FE model for the foil structure are not coupled so that the former and the latter render both the displacements for the bending plate and elastic plane (or membrane) models, respectively [25,26]. On the other hand, Refs. [27,28] introduce a fully coupled finite element formulation, with membrane and bending stresses in a cylindrical shell coupled through moment, tension, curvature, and strain expressions. The model incorporates both the pressure developed by the gas film flow and the structural deflections of the top and bump foils into a single finite element. The predictions exhibit irregular shapes of pressure and film thickness due to foil detachment in the exit region of the gas film. Note that references [25-27] model the structural bump layers as a simple elastic foundation. Reference [28] models the bump strip layer as a continuous elastic foundation which accounts for the radial and circumferential deflections of the bumps, but does not show the sagging effect of the top foil between adjacent bumps. In the model, one half of a symmetric bump is analyzed while ignoring the curvature of the bump strip layer. The energy dissipation is calculated using the equivalent viscous damping model for dry-frictional effects between the top foil and bumps, and between the bumps and the bearing housing. The effects of whirl orbit amplitude and frequency and dry-friction parameters on predicted bearing stiffness and damping coefficients are studied for a low load application. According to the authors' predictions, the direct damping coefficients decrease as the dry-friction coefficient increases because there is stick of the bumps against the bearing, for example. These are opposite to those in [22]; however, the physical phenomenon is different.

Heshmat et al. [29] predict the static load performance of thrust GFBs. The numerical procedure couples a finite element model of the structural supports, generated by a commercial code, to the gas film hydrodynamics modeled with finite differences. Shells model the top foils, which are supported on a simple elastic foundation representing the bump strips. Comparison of predicted static load capacity to measurements shows good agreement. Heshmat et al. [30] predict the static performance of journal GFBs to investigate the feasibility of a hybrid foil–magnetic bearing configuration. The numerical model in [29] is enhanced by efficiently using a structural influence coefficient matrix representing the combined action of top foil and bumps.

Kim and San Andrés [31], in comparisons with limited experimental test data by Ruscitto et al. [32], validate GFB forced performance prediction implementing the simple elastic foundation model. The model uses an axially averaged pressure enabling a journal to move beyond its nominal clearance when supporting large static loads. The predictions demonstrate that a heavily loaded gas foil bearing may have journal eccentricities over three times greater than its nominal clearance. Predictions for film thickness and journal attitude angle for increasing static loads are in good agreement with test data for moderately to heavily loaded GFBs with journal eccentricities greater than the nominal clearance. In lightly loaded regions, there are obvious discrepancies between predictions and experimental data because of the fabrication inaccuracy of test GFBs [32,33]. At the ultimate load condition, the predictions show a nearly constant GFB static stiffness, indifferent to rotor speed, and with magnitudes close to the underlying bump support stiffness determined in contact conditions without rotor spinning.

Lee et al. [34] present the effects of bump stiffness on the static and dynamic force performance of GFBs. The top foil is modeled as an elastic beam-like model while a bump is represented by a linear spring coefficient. Predictions call for optimal bump stiffness magnitudes at specific rotor speeds to maximize the bearing load capacity. Furthermore, individual bump stiffnesses affect GFB stability for operation at high rotor speeds.

Lee et al. [35] advance a computational model integrating the foil sub-structure. The FE models for the top foil and bump strip layer are coupled to the gas film pressure hydrodynamic model and predicts the bearing minimum film thickness, attitude angle, and force coefficients. The authors also conduct experiments to identify frequency-independent stiffness and damping coefficients of a test floating GFB from measurements of an applied impact load and ensuing bearing motions (impedance formulation). Predicted direct stiffnesses agree reasonably with test data for operation between 15 to 25 krpm; while predicted and test-derived damping coefficients decrease as rotor speed increases. Unfortunately, this publication does not provide enough information on the bearing tested (geometry, materials, etc) and, in the writer's point of view, implements an identification method not appropriate for GFBs.

A gas foil bearing has an ultimate load capacity at a journal eccentricity well in excess of its *nominal* bearing clearance. In actuality, the *nominal* clearance in a GFB is a vague concept. Peng and Khonsari [36] introduce a unique analysis for the ultimate load capacity of GFBs at *infinite* speed number operation. A bearing clearance and underlying stiffness of the foil support determine this load. In practice, however, either by design or due to inaccurate manufacturing, GFBs do not possess an actual clearance, i.e. an *air gap* between the journal and its support structure. For mechanical integrity, GFBs are usually preloaded (assembly interference or shimmed), with the journal diameter being larger than that of the top foil. The preload ensures even contact at the static condition (no shaft speed) with uniform pressures pushing on the elastic structure. Radil et al. [37] find a strong correlation of GFB measured load capacity to the bearing clearance. In operation, the journal grows due to thermal and centrifugal effects, thus exacerbating the effects of the largely unknown GFB "clearance."

Kim and San Andrés [13] update the analysis in [36], including the effect of an assembly preload, and provide analytical formulae for estimation of load capacity, minimum film thickness and stiffness coefficients for operation at large shaft speeds, *infinite* in theory. The underlying elastic structure (bump foil strip) determines the ultimate load capacity of a GFB as well as its stiffnesses, along with the limiting journal displacement and structural deformation. Thus, an accurate estimation of the actual *minimum film thickness* is found prior to performing calculations with a complex computational model, even for the case of large loads that result in a journal eccentricity well exceeding the nominal clearance, if applicable. An initial assembly preload (interference between shaft and foil) increases the GFB static stiffness at both null and infinite rotor speeds. Their predictions reproduce with exactness the measured structural stiffness and elastic deformation for the contact condition between shaft and foil, i.e. without journal rotation.

Adequate thermal management is necessary when incorporating GFBs into high temperature applications, such as in a gas turbine engine [38]. A side end cooling flow aids to prevent GFBs from encountering thermal seizure, thus maintaining an adequate load capacity and stability [26]. Salehi et al. [39] predict GFB static load performance and temperature fields by using Reynolds and gas film energy transport equations coupled to the *simple elastic foundation model* [9]. The Couette flow approximation [40] simplifies the energy equation by neglecting the work done by pressure, and effectively uncouples it from the Reynolds equation. Thus, the analysis calculates only the circumferential temperature distribution at the bearing mid-plane. The axial temperature distribution is assumed to linearly decrease toward the bearing edges. Experiments aid to estimate the temperature-raise of the cooling flow passing through the GFB by measuring the flow inlet and outlet temperatures using thermocouples installed on the outer side of the top foil. The measurements reveal that the GFB has a greater temperature in the static load direction rather than in the opposite direction. The temperature grows with increasing rotor speed and static load. A comparison of the predicted temperature-rise of the cooling flow to the experimental measurement shows good agreement within a deviation of ~20 %.

Peng and Khonsari [41] introduce a THD model to predict the steady-state performance of GFBs. A simple elastic foundation represents the foil structure with coupled Reynolds and thermal energy transport equations solved simultaneously for prediction of the gas film pressure and temperature fields. Heat convection coefficients based on the cooling flow regime are obtained. Predictions reveal a nearly uniform film temperature along the bearing axial direction; and with an increase in load capacity since typical gas viscosity increases with temperature. Comparison of predicted temperatures to test data in [39] is noted as excellent. However, Radil and Zeszotek [42] find a decrease of ~30 % in load capacity for a GFB tested at increasing temperatures ranging from 25ºC to 650 ºC. Apparently, temperature-dependent mechanical properties of the structural components and actual dimensions (thermal growth) need be accounted for to obtain reliable predictions.

Structural Stiffness and Damping Models and Experiments

Gas film stiffness coefficients change significantly with rotor speed, while those of the structural bumps of GFBs do not. Typically, high operating speeds of a rotor supported on GFBs lead to relatively stiffer gas films in relation to structural bumps. Thus, GFB stiffness characteristics mainly depend upon the nature of the structural bumps. The direct stiffness coefficients of GFBs are most important since they largely determine the critical speed of the rotor – GFB system and the corresponding machine's operating speed regions. Note that the structural bump stiffness does not produce a cross-coupled stiffness which would, in turn, lead to hydrodynamic instability of the rotor supported on the GFBs. Damping in the GFBs is a most difficult issue to resolve because the frictional damping arising from material hysteresis and dry-frictional effects between the underlying structural bumps has not yet been clearly disclosed theoretically and experimentally. Because of a stiff gas film, implying a low level of viscous film damping, at operating speeds, the damping from the underlying structural bumps becomes important.

Ku and Heshmat [43,44] present a theoretical model to predict the synchronous stiffness and damping coefficients of the structural bump strips in GFBs. The stiffness coefficients are calculated based on the perturbation of the shaft center with respect to its equilibrium static position. The equivalent viscous damping coefficients are determined based upon the area of a closed hysteresis loop of the shaft center motion. The transmitted forces to neighboring bumps are calculated using equations for the static force and moment equilibrium of one bump. The governing equations for determining radial and tangential deflection of the elastic curved beam calculate the deflection of one bump using the equations presenting the bending moments and stresses. With boundary conditions for these deflections, the reactive bump deflections to loads at the bump top centers are calculated from the first bump to the last bump. Iterative numerical scheme calculations determine the reactive force of a GFB to the imposed load, using the initial guessed values for the bump's tangential deflection. After the shaft center reaches its static equilibrium position, perturbations of the shaft center calculate the stiffness and damping coefficients of the structural bump strips in the GFB. Predictions show that stiffness and damping coefficients are highly nonlinear and anisotropic. The dynamic coefficients increase with increasing static journal eccentricity, decreasing perturbation amplitude, and decreasing excitation frequency. The direct damping coefficients increase with the increasing friction coefficients, but the damping coefficients reach their asymptotic values when friction coefficients approach an optimum value. The ratio of the dimensionless direct damping to the dimensionless direct stiffness shows approximately 0.25 to 0.3, implying that the equivalent structural loss factor, i.e., the ratio of effective damping to effective stiffness, is between 0.25 and 0.3.

Ku and Heshmat [33] perform an experimental investigation on bump deflections in GFBs. An optical tracking system for a wide range of operating conditions verifies the feasibility of the theoretical model [45]. The effects of GFB parameters such as bump configuration, load profile, and surface coating and lubricant on the structural characteristics of the bump foil strip are investigated. The observations of the phenomena reveal that the horizontal deflection of the segment between the bumps is negligible when compared to the horizontal deflection of the bumps and the surface contact between the top smooth foil and the bump layer is a line contact rather than a point contact. A series of load – deflection tests using the optical tracking system shows bumps separating from the lower pad before the load is applied cause the nonlinearity of the hysteresis loop in the lightly loaded region, and that the bump layer provides more Coulomb damping in the lightly loaded region than in the heavily loaded region. A comparison of test data for bare and surface-coated bump layers demonstrates that the existence of friction forces between the contact surfaces and the local interactive forces between bumps causes the local stiffness to be dependent upon both amplitude and load.

Heshmat and Ku [46] investigate through experiments, the dynamic characteristics of the structural bumps used in GFBs. The authors employed two shakers to impose dynamic forces acting on the structural bump strips installed in the GFB’s housing, which floats on a non-rotating shaft. The dynamic structural stiffness and equivalent viscous damping coefficients are calculated according to a wide range of excitation frequencies. The paper compares the test results to the analytical predictions obtained by the theoretical model described in [43-45]. Both the test results and the predictions present evidence that direct stiffness and damping decrease with an increase in the dynamic vibration amplitudes induced by the shakers. An increase in the shaker excitation frequency decreases the direct damping and increases the direct stiffness. Thus, the paper demonstrates that the structural bump of the GFBs has forced the creation of nonlinear characteristics. The results are obvious for a dry-friction model, i.e. $C \sim \gamma/\omega$.

Salehi et al. [47] develop a semi-empirical single degree of freedom model to estimate an equivalent frictional force between individual bump and surface interfaces, providing the GFBs with a damping ability. A comparison between the two separate data evaluation techniques, namely the hysteretic and the single degree of freedom models, shows good agreement between the equivalent damping coefficients. The variation in damping and dynamic coefficients of friction depends primarily upon three factors: vibration frequency, amplitude of motion, and applied static loads. These parameters were tested within the range of 50 Hz to 1400 Hz, 2.54 μm to 12.7 μm and 45 N to 135 N, respectively. Both the hysteretic and the single degree of freedom model methods show that damping coefficients decrease dramatically up to ~200 Hz (the structural resonance frequency band), after which the damping decreases at a slower pace. The damping coefficients drop exponentially with an increase in the vibration amplitude and increase proportionally with the static load. The operating tests of a high-speed gas turbine engine simulator with extremely high levels of shaft imbalance at room and high (538 °C) ambient temperatures under both dry and vapor phase lubricated conditions validate the potential of wide applications of these GFBs or foil dampers for gas turbine engines and high-speed rotating machinery.

Rubio and San Andrés [48] conducted static load versus deflection test on test GFB structure for three test shafts of different diameter, i.e. varying degrees of preload, to investigate the effect of a mechanical interference between the shaft and bearing on GFB structural stiffness. Experimental test data demonstrate nonlinear bearing deflections and show that increasing preload causes a higher structural stiffness. A predictive GFB structural model assembles linear springs of the individual bumps. The model does not include a top foil, because top foil deflections along the axial direction are necessarily unique, and hence membrane forces and bending moments are negligible [31]. The model predictions are in good agreement with experimentally estimated structural stiffness.

Rubio and San Andrés [49] conduct shaker tests to estimate the structural stiffness and equivalent viscous damping coefficients of GFBs. Energy dissipated during one cycle excitation with a single frequency identifies the bearing structural parameters using the mechanical impedance identification method. The test measurements show that bearing stiffness decreases and equivalent viscous damping coefficient increase as the amplitude of dynamic load increases. The dry friction coefficient increases as the load amplitude increases, ranging from 0.05 to 0.2.

Rotordynamic Measurements

GFBs are distinguished from rigid gas bearings by their high operating speeds, superior stability characteristics, and high temperature endurance using solid lubricants (or coatings).

Heshmat et al. [15] test two types of the second generation [7] bump type GFBs: single pad GFBs and three-pad GFBs. The 35mm diameter – 44 mm length bump type GFBs have a single top foil and a single split-staggered bump layer, or three top foils and three split-staggered bump layers for the single and three pad GFBs, respectively. To improve frictional characteristics, the rubbing surfaces of the smooth top foil and bump layers were sputter coated with copper. The thickness of the sputtered coating was 3.8 μm on the back side of the top foil and on the top of the bump layers. The load versus deflection tests along the pad location reveal that the three pad GFB has variable structural bump stiffnesses along the pad: the largest stiffness is near the weld, and the smallest stiffness is near the free end of the bump layer. This variable-bump stiffness provides the three pad GFBs with a varying preload along the pad. Four eddy current sensors measure the rotor vibration at the driven turbine and free ends. Sudden increases in the overall rotor orbit size determine the maximum operating speeds for the single and three pad GFBs. The test results with the three pad GFBs demonstrate that the GFBs are more stable and have a greater operating speed when they have the rotor rotating direction from the free end of the pad to the welded end. Four levels of in-phase unbalanced rotor tests reveal that the onset speed of instability is, to some degree, inversely proportional to the magnitude of the unbalance level. The single-pad GFB with sputtered copper coated top and bump foils operates up to the maximum rotor speed of 120,000 rpm, and has the maximum static load capacity of 533.8 N (120 lb) or 352 KPa (51 psi) specific load for the projected bearing area at 68,000 rpm, demonstrating that sputtered copper coated top and bump foils improve the performance of the GFBs.

Heshmat [8] introduces single top foil, multistage bump strip layers to engineer tunable bearing support stiffness along the radial and circumferential directions. See Fig. 2. The designed stiffness gradient ensures a hydrodynamic wedge or a lobe-like effect for enhanced generation of hydrodynamic pressure. As the shaft speed increases, gas pressure pushes the top foil and bumps outwards, thus forming a converging wedge film shape. In the experiments, a multistage bump strips GFB, 35 mm in diameter and 31 mm in length, achieves an impressive ultimate load capacity of 728 N [6.73 bar (98 psi) specific pressure]. Heshmat also demonstrates the successful operation of GFBs to a maximum speed of 132 krpm, i.e. 4.61×10^6 DN value; albeit the vibration measurements show large-amplitude subsynchronous whirl motions related to the test rotor rigid body mode natural frequencies. However, in spite of the subsynchronous whirl, the rotor reached a stable limit cycle operation.

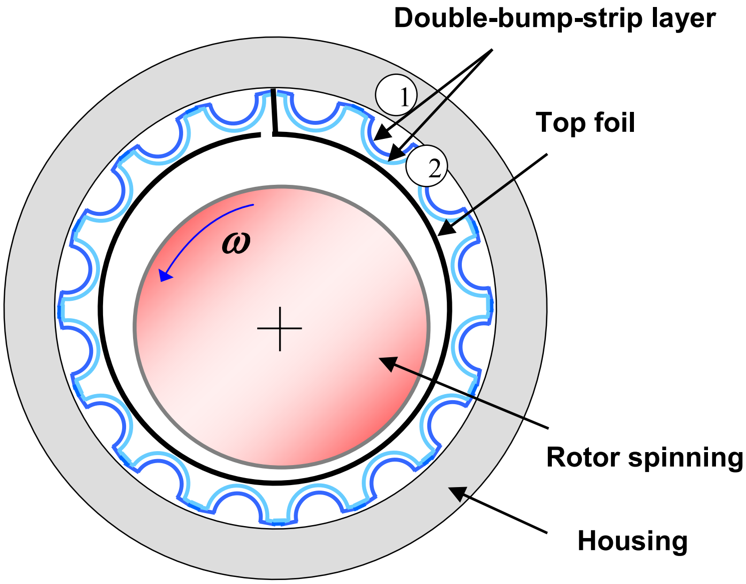

Figure 2 Schematic view of multistage-bump-strip GFB. Based on Ref. [8].

Heshmat [50] demonstrates the super critical bending mode operation for a flexible rotor supported on bump type GFBs. Super critical bending mode operation for GFBs refer to highly efficient, oil free turbomachinery with very high rotating speeds. He used three GFBs treated differently from one other: a GFB with only one layer of bare bump foil, a GFB with staggered (multiple) layers of bare bump foils, and a GFB with staggered (multiple) layers of 2.5 µm – copper - coated bump foils. The multiple layers imply the largest bearing structural stiffness. The half power method estimates a GFB equivalent damping confidents from peak-hold amplitude data and a rotordynamics computer code that calculates the corresponding values of log decrement to the empirical bearing equivalent damping coefficients. The rotor unbalance responses are synchronous with rotating speed before passing the rotor bending critical speed of 34 krpm. Then, large subsynchronous vibrations at the rigid-body-mode natural frequency appear while passing the bending critical speed and continuing to speed up to 85 krpm.

Nevertheless, the recorded unbalance responses show no evidence of rotordynamic instability, but the limit cycle orbital vibrations. From the calculated equivalent damping data, Heshmat concludes that there are no clear improvements in the GFB performance by treating the bearing in different ways and that a correct rotor - bearing span is more effective in enhancing the stability characteristics of the system.

Lee et al. [51,52] introduce a viscoelastic-bump foil bearing to improve the damping characteristics of GFBs. Structural tests using shakers estimate the structural equivalent damping coefficients of the two types of GFBs: a GFB with one layer of 5 μm – copper - coated bump foils and a GFB with one layer of bare bump foil and an additional viscoelastic layer, named viscoelastic – bump foil bearing. The authors find experimentally that the latter demonstrates a more significant equivalent damping from the viscoelastic layer than the former. A series of super critical bending mode operations using the two types of GFBs compare their unbalance responses during a coastdown from 50,000 rpm. The flexible rotor passes through its bending critical speed near 30,000 rpm. Test results with the GFB with one layer of 5 μm – copper - coated bump foils demonstrate the same type of limit cycle orbital vibrations as those presented in [50] at rotor speeds higher than the rotor bending critical speed. The comparison of test results with the two different types of GFBs reveals that the viscoelastic-bump foil bearings not only aid in attenuating the large amplitudes of motion near the rotor bending critical speed, but also suppress subsynchronous vibrations at rotor speeds higher than the rotor bending critical speed. Note that this novel improvement is presently restricted to low and moderate temperature applications.

Lee et al. [53] perform high speed operation tests on a two stage, centrifugal compressor supported by GFBs in an aerodynamic surge condition. Two gas foil journal bearings and one gas foil thrust bearing support a 55 mm diameter – 425 mm length rigid rotor with two impellers at both ends. The rotor is driven by a 75 kW induction motor operating at a maximum speed of 39,000 rpm. The rotor is designed to have operating speeds higher than cylindrical and conical, rigid-body-mode critical speeds, and lower than the 1st bending critical speed. The compressor housing contains two pairs of eddy current sensors to measure the rotor vibrations near the two journal bearings and an optical type tachometer to measure the rotor speed. The inlet air goes through the two compressors and then exits. The compressor exit pipe has an air flow control valve and static and dynamic pressure sensors to measure the static and dynamic pressures near the exit of the compressor. Closing the control valve reduces the exit air flow and eventually causes an aerodynamic surge; [30] details the compressor performance. A series of operating tests at 39,000 krpm with two different types of GFBs: GFBs with one layer of 5 μm – copper - coated bump foils and GFBs with one layer of a bare bump foil and an additional viscoelastic layer, named viscoelastic – bump foil bearings were used to compare the rotordynamic performances of the GFBs. In the compressor steady pressure region, the rotor shows only synchronous vibrations. However, in the surge region unsteady aerodynamic pressures at the multiple frequencies of 9 Hz excite the rotor. The rotor supported on the GFBs with one layer of 5 μm – copper - coated bump foil shows larger level of subsynchronous vibrations at multiple frequencies of 9 Hz than the synchronous vibrations, and the largest value of subsynchronous vibrations around the rigid-body-mode's natural frequencies. On the other hand, replacing the GFBs with viscoelastic bump GFBs significantly reduce the subsynchronous vibrations, especially near the rotor rigid body mode natural frequencies. A comparison of the whole frequency range of vibrations of both two GFB cases at 39,000 rpm demonstrates that enhanced viscous damping from the viscoelastic layer significantly reduces rigid body resonant subsynchronous vibrations. [8,50,51] show large subsynchronous vibrations associated with rigid-body-mode natural frequencies at the maximum operating speed, implying that the resonant subsynchronous vibrations eventually induce instability in the GFBs. Therefore, getting rid of the source of the subsynchronous vibrations may improve the stability characteristics of the GFBs.

Ruscitto et al. [32] perform a series of load capacity tests of "first generation" bump type foil bearings [7]. The test bearing, 38 mm in diameter and 38 mm in length, has a single top foil and a single bump strip layer. The authors note that the actual bearing clearance for the test bearing is unknown. Thus, the journal radial travel (c_J) was estimated by performing a static load-bump deflection test. The authors installed displacement sensors inside the rotor and measure the gap between the rotor and the top foil at the bearing's center plane and near the bearing edge. As the static load increases, for a fixed rotational speed, the minimum film thickness and journal attitude angle decrease exponentially. The test data for film thickness is the only one available in the open literature.

DellaCorte et al. [54] performs load capacity tests on GFBs with various combinations of shaft coatings and top foil coatings. Various coating conditions (sprayed, heat treated, ground, and polished) are tested to compare their ability to improve the GFB load capacity. PS304 coatings on the shaft were overcoated with either polyimide, or Molybdenum Disulphide (MoS_2) for additional solid lubrication. PS304 is a NICr based Cr_2O_3 coating with silver and barium fluoride/calcium fluoride solid lubricant. Test results reveal that an effective solid lubricant film such as MoS_2 must be present on the top foil surface to achieve a satisfactory load capacity upon initial installation of a PS304 coated shaft, i.e. an as-ground PS304 coated shaft. Non-galling wear resistant coatings such as PS304 on the shaft and Al-Cu on the foil enhance performance even further. To prevent bearing failure, the material selected must not produce large, hard debris particles as was the case with the polyimide, especially upon thermal decomposition (burn-off). Thus, the combination of the PS304 coated shaft with sacrificial MoS_2 running against Al-Cu coated top foil works synergistically to give a maximum load capacity from the first installation to fully run-in GFB operations.

Radil and DellaCorte [55] examine the effects of journal roughness and foil coatings on the performance of heavily loaded GFBs. PS304 coating protect the top foil surface of GFBs from serious wear during start up and shut down in the absence of an air film. The 3rd generation GFB [7] exhibits a load coefficient, Đ of 1.0. The load coefficient is defined based on a Rule of Thumb (ROT) model proposed in DellaCorte and Valco [7]. The paper compares the load capacity coefficients of GFBs with three different solid lubricant coatings on the top foil, which present different initial coating roughness values. Two different shaft coating conditions, as-grounded PS304 and run-in PS304 coated shafts are tested to evaluate the load capacity coefficient, *Đ*. Test results and comparison of these test results yield several observations: break-in foil coatings that inhibit galling can, at varying degrees, increase *Đ*. Coatings that possess solid lubricant properties further increase the load coefficient by providing a solid lubrication component when the bearing is operating under both boundary and mixed lubrication conditions. Note that Radil and DellaCorte mention that the current practice of using plasma spraying to apply the PS304 material results in a porous coating on the shaft surface. To maximize performance, foil bearings operating against PS304 coated shafts must undergo high temperature start up and shut down operations to produce the smooth oxide layer, conforming surface, and lubricious transfer film on the GFB top foil.

Chen et al. [14] replace a tape-type foil bearing with a bump-type foil bearing in a helium turbocompressor. The paper describes the design and fabrication of a bump-type foil bearing, and presents a comparison in rotordynamic performance tests for the original tape-type foil bearings and the replacement bearings. The bump-type foil bearings have one top foil supported on three bump strip layers. To enhance the dynamic stability of a compressor rotor operating in the vertical direction, a shim was installed at the middle of each bump layer, thus providing a radial preload to the foil bearings. The frictional torque of the foil bearings is significant before rotor lift-off and decreases once the rotor speed is high enough to generate a hydrodynamic film pressure. Steady state and speed transient tests show that the implementation of the bump-type foil bearing increased the critical speed of the original system because the bearing stiffness is greater than that of the original rotor supported on tape-type bearings.

San Andrés et al. [17] investigate the rotordynamic performance of a rotor supported on GFBs. A series of coastdown tests with small to large imbalance masses inserted in a hollow rotor demonstrate that large imbalance masses induce subsynchronous motions of large amplitude and associated with low frequency rigid body modes. Rotordynamic model predictions do not correlate well with the test data. A comparison of normalized imbalance response amplitudes reveals a nonlinear rotor behavior since the GFB stiffness and damping coefficients are amplitude and frequency dependent. External air pressurization through the bearing ends reduces the amplitude of synchronous motions while crossing a critical speed. Incidentally, the tests also demonstrate that increasing air pressurization ameliorates the amplitudes of subsynchronous motions.

Rotordynamic Parameter Identification

Howard [56] and Howard et al. [57] examine trends in static stiffness of GFBs as a function of rotor speed and static load in ambient and high temperature operating conditions. The high temperature GFB test rig measures the bearing displacement in the low and high temperature test conditions to identify static and dynamic stiffness and damping coefficients. The static stiffness is identified by applying a known weight to the GFB in a vertical direction and by measuring the resulting GFB displacement in the same direction, i.e. its direct stiffness. Optical probes measure the bearing displacement because they are able to withstand temperatures up to 700 ºC. The relatively small perturbations of the test GFB around the operating shaft ensure accurate identification. Test results indicate that the static stiffness of GFBs increases as the static load increases, and as the rotor speed decreases. The static stiffness decreases, in general, as the temperature increases from 25 ºC to 538 ºC. The change in stiffness with temperature is most significant.

Howard et. al. [58] perform an impact test on a GFB and characterize its dynamic direct stiffness and damping at various temperatures, loads and speed conditions. Cross-coupled stiffness and damping were not identified in the test procedure. Transient response calculations using experimental test data are compared with both exponential (viscous damping behavior) and linear (Coulomb damping behavior) decays to find the dominant energy dissipation mechanism. Experimental results demonstrate that, at high temperatures and low static loads, the gas film is soft (compared to the foil structure) thus showing viscous damping behavior. Conversely, at low temperatures and high static loads the bearing behaves like a dry friction system due to the gas film being stiffer than the foil structure.

Recently, Lee et al. [35] conducted experiments to identify frequency-independent stiffness and damping coefficients of a test floating GFB from measurements of an applied impact load and ensuing bearing motions (impedance formulation). A complementing computational model integrating the foil sub-structure and gas film predicts the bearing minimum film thickness, attitude angle, and force coefficients. Predicted direct stiffnesses agree reasonably with test data for operation between 15 to 25 krpm, while predicted and test-derived damping coefficients decrease as rotor speed increases.

High Temperature Operations

DellaCorte et al. [59] develop a high temperature GFB test rig which measures bearing torques during start up and shut down operations, and load capacity in moderate to high temperature test conditions during high speed operations up to 70,000 rpm. Measured bearing toque versus rotor speed clearly shows a mixed boundary – hydrodynamic lubrication region and the purely hydrodynamic region, showing the peak value of the measured torque during both the start up and the shut down stages. The GFB toque is a linear function of the static load and the GFB load capacity is a linear function of the rotor speed. In general, the load capacity decreases as the ambient temperature increases.

DellaCorte et al. [60] perform durability tests on GFBs with a PS304 (high temperature solid lubricant) coating [61-64] for operations between 25 ºC and 650 ºC. PS304 high temperature solid lubricant coating is applied to the shaft by a plasma-spraying coating technique. The GFB experiences sliding contact (rubbing) with the shaft during initial start up and shut down operations. The authors measured the start/stop torque, friction coefficients, and bearing wear rates during 100,000 start/stop cycles. The test results reveal that wear is a linear function of the bearing static load. The research demonstrates a suitable static performance of gas foil bearings in moderate to high temperature applications.

Bauman [16] introduces a thrust GFB test rig for use in future oil-free gas turbines being developed at NASA. The test rotor supported on a thrust GFB and two journal GFBs operates to a top speed of 80,000 rpm and temperatures up to 650 ºC (1200 ºF). A hydrostatic loader piston provides an axial load to the shaft, and a magnetic thrust bearing counteracts the test thrust GFB loads ensuring a steady motion of the thrust runner. Cooling air is supplied into the test rig housing to carry away waste heat from the magnetic thrust bearing as well as the heat conducted from a hot turbine to the journal GFB. The axially fed cooling flow prevents hot-spots in the GFB and extends its life. Measurement parameters of the test rig include bearing torque, load capacity, and bearing temperature, which will be used to validate computational models of GFBs.

Lubell et al. [65] evaluate high temperature coatings for GFBs used in oil-free micro gas turbine engines. The solid lubricant not only reduces friction torque during the start-up and shut-down of turbomachinery supported on GFBs, but also prevents failures related to coating degradation of the shaft and bearings at high temperatures, well above 500 ºC (930 ºF). The paper describes a micro gas turbine engine test with a shaft coated using PS304 developed by NASA. The shaft is supported on a GFB in the hot section. During endurance engine tests, two coating related failures were recorded. Subsequently, new coating procedures were adopted, i.e. plasma spray on the shaft with an oblique angle at both shaft end locations and simple heat treatment of coated parts prior to final surface grinding. These procedures coat the shaft surface uniformly and enhance the coating adherence, thus improving the coating micro-structural stability characteristics at high temperature operation. Further engine tests demonstrated successful operation at 500°C (930°F) for over 2,500 hours and 2,900 start-stop cycles without damage or loss of performance.

Models of GFBs with Side End Pressurization

Pressurized feed air is often needed to cool GFBs as well as the integral drive motor (or generator) mounted between GFBs in oil-free rotating machinery, for example [66]. However, for sufficiently high pressures, the end gas flow will affect the rotordynamic performance of GFBs. Measurements in [17] demonstrate that the external air pressurization through a bearing end not only reduces the amplitude of synchronous motions while crossing a critical speed, but ameliorates the amplitudes of subsynchronous motion for operation at shaft speeds about two times the critical speed.

The effect of side end pressurization on GFB force performance may be derived from similitude to annular pressure seals, for example. Allaire et al. [67] analyze short length annular liquid seals, $L/D = 0.16$, considering the circumferential flow is relatively small relative to the axial flow. Thus, a circumferential momentum equation is not considered in the analysis, i.e. the continuity and axial momentum equations are used to evaluate the seal forced performance. Pressure boundary conditions are determined by considering a Bernoulli type non-isentropic head loss. Perturbed pressures, axial flow velocity, and film thickness about a rotor equilibrium position determine the stiffness and damping coefficients as well as the load capacity of short seals. The model predictions show that short seals produce large stiffness and damping coefficients; and due to the slow development of circumferential flow, small cross-coupled stiffness coefficients. In general, the whirl frequency ratio, an indicator of bearing stability, equals the inlet swirl ratio in short length seals [68].

Black et al. [69] present the effects of fluid inlet swirl velocity on the force performance of annular liquid seals. Prior models incorrectly assume a fully developed circumferential flow over the whole seal axial length. Black et al., on the other hand, show that the circumferential velocity approaches one half of rotor surface speed as the seal axial length increases. Model predictions note that the proper amount of anti-swirl inlet velocity strongly reduces or even eliminates seal cross-coupled stiffness coefficients.

CHAPTER III

ANALYSIS OF GFBS USING 1D AND 2D FE TOP FOIL MODELS

Introduction

Application of GFBs into midsize gas turbine engines demands accurate performance predictions anchored to reliable test data. Modeling of GFBs is difficult due to the mechanical complexity of the bump strip layers and top foil structure, further aggravated by the lack of simple, though physically realistic, energy dissipation models at the contact surfaces where dry-friction is prevalent.

High operating speeds of a rotor supported on GFBs lead to relatively stiffer gas films in relation to the stiffness of the support bump strip layers. Thus, the overall stiffness of GFBs depends mainly on the sub-foil structure stiffness, and the damping arises from material hysteresis and dry-friction effects at the contact surfaces between bumps and top foil and bumps and bearing casing. An accurate modeling of the sub-foil structure is necessary to advance a more realistic predictive tool for the performance of GFBs.

In this chapter, the top foil, modeled as a 2D structural shell using Finite Elements, is integrated with the bump strip layers and in conjunction with the hydrodynamic gas film to predict the static and dynamic load performance of GFBs. A simpler model, i.e. a 1D beam-like structure is also introduced. For validation, predictions of GFB performance implementing a 1D top foil and a 2D top foil models are compared to limited test results available in the literature.

Description of Gas Foil Bearings

Figure 3 shows the configuration of a “first generation” bump type GFB [7]. The GFB consists of a thin (top) foil and a series of corrugated bump strip supports. The leading edge of the thin foil is free, and the foil trailing edge is welded to the bearing housing. Beneath the top foil, a bump structure is laid on the inner surface of the bearing. The top foil of smooth surface is supported by a series of bumps acting as springs, thus making the bearing compliant. The bump strip provides a tunable structural stiffness [9]. Damping arises due to material hysteresis and dry-friction between the bumps and top foil, and between the bumps and the bearing inner surface [10].

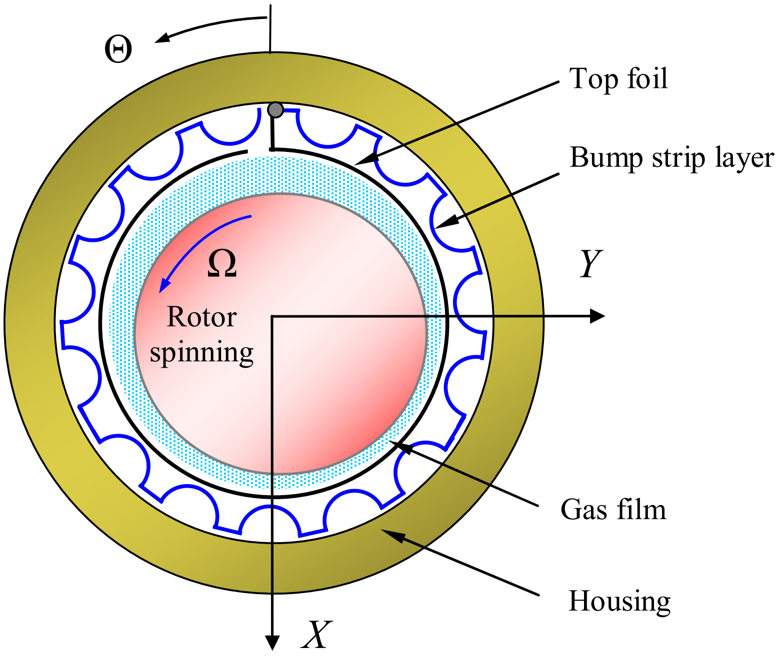

Figure 3 Schematic view of "first generation" bump type foil bearing.

The Reynolds equation describes the generation of the gas pressure (p) within the film thickness (h). For an isothermal, isoviscous ideal gas this equation is

$$\frac{\partial}{\partial x}\left(ph^3\frac{\partial p}{\partial x}\right)+\frac{\partial}{\partial z}\left(ph^3\frac{\partial p}{\partial z}\right)=6\mu\Omega R\frac{\partial(ph)}{\partial x}+12\mu\frac{\partial(ph)}{\partial t} \tag{1}$$

where (x, z) are the circumferential and axial coordinates on the plane of the bearing. The pressure takes ambient value (p_a) on the side boundaries of the bearing. The film thickness (h) for a perfectly aligned journal configuration is

$$h = c - r + e_X \cos(\Theta) + e_Y \sin(\Theta) + w_d \tag{2}$$

where c and r are the assembled clearance and assembly interference, respectively; and (e_X, e_Y) are the journal center displacements. w_d is the elastic deflection field of the underlying support structure, a function of the acting pressure field and the material and geometric characteristics of the support structure comprised of the top foil and the bump strip layers.

Modeling of Top Foil Support Structure

Simple elastic foundation model

Most published models for the elastic support structure in a GFB are based on the original work of Heshmat et al. [9,20]. This analysis relies on several assumptions which other researchers [10,21,22,31] also reproduce:

(1) The stiffness of a bump strip is uniformly distributed throughout the bearing surface, i.e. the bump strip is regarded as a uniform elastic foundation.

(2) A bump stiffness is constant, independent of the actual bump deflection, not related or constrained by adjacent bumps.

(3) The top foil does not sag between adjacent bumps; Figure 4 shows the top foil sagging in actual GFBs. The top foil does not have either bending or membrane stiffness, and its deflection follows that of the bump.

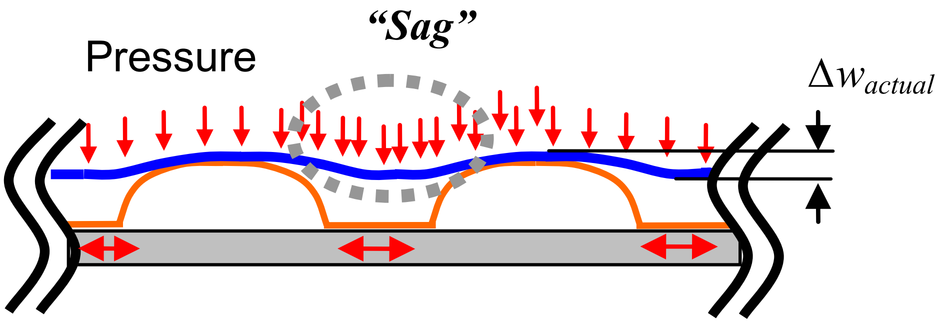

Figure 4 Schematic representation of pressure field acting on top foil and showing top foil "sagging" between two adjacent bumps.

With these considerations, the local deflection of a bump (w_d) depends on the bump structural stiffness (K_f) and the average pressure (δp_A) across the bearing width, i.e.,

$$w_d = \delta p_A / K_f \tag{3}$$

where $\delta p_A = {}^{1}\!/\!_{L} \int_0^L (p - p_a)\, dz$, and p_a is the ambient pressure beneath the foil.

Coupling of the simple model, Eq. (3), with the solution of Reynolds Eq. (1) is straightforward, leading to fast computational models for prediction of the static and dynamic force performance of GFBs, see [9,10,31] for example.

Presently, the predictive analysis is extended to account for and integrate with the elastic deformation of the top foil. The top foil is modeled as a beam-like structure (1D model) and a flat shell (2D model), i.e. without curvature effects since the transverse deflections are roughly ~0.001 of the top foil assembled radius of curvature. The first model is simpler and less computationally intensive. Both top foil structural models incorporate the bump strip layer as a series of linear springs, not connected with each other. Interactions between adjacent bumps are altogether neglected, as in most predictive models. The stiffness of each bump is regarded as constant (irrespective of the load), thus denoting no change in the nominal or manufactured bump pitch.

One dimensional model for top foil

In their extensive GFB experimental work, Ruscitto et al. [32] report relatively small differences in axial gas film (minimum) thickness for heavily loaded conditions. This means that an average pressure causes a uniform elastic deformation along the top foil of width (L). Hence, a one dimensional structural model, with infinite stiffness along the bearing width, may suffice to model the top foil, as shown in Fig. 5. One end of the top foil is fixed, i.e. with transverse deflection and rotation equal to zero; while the other end is free. Figure 5 also shows the idealization of the 1D model with its degrees of freedom, namely transverse deflections (w_d) and rotations (ϕ_x).

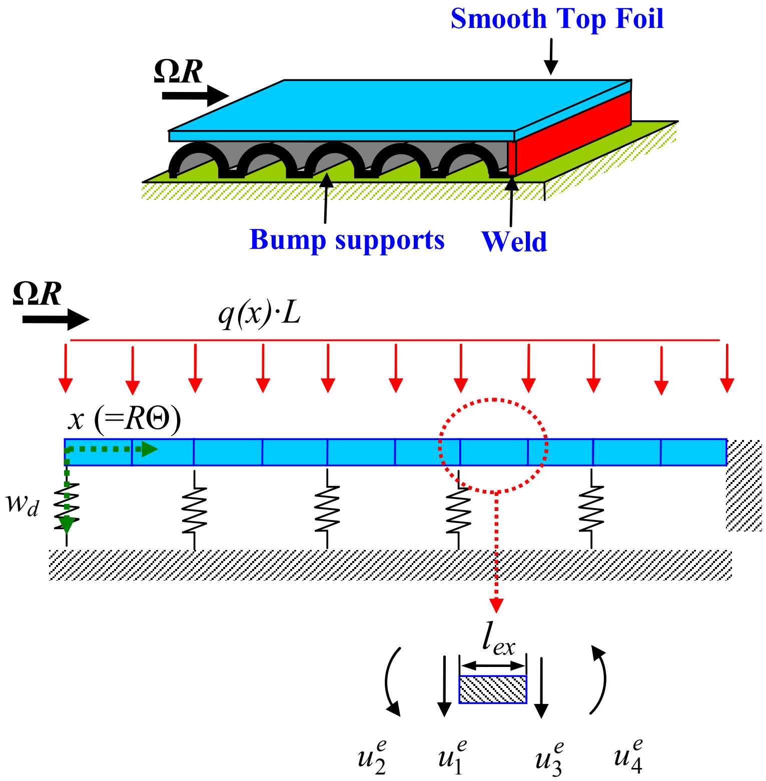

Figure 5 Configuration of top foil supported on a bump strip and its 1D structural model. Generalized displacements: $u_1^e = \boldsymbol{v_1}$, $u_2^e = \boldsymbol{\phi_{x1}}$, $u_3^e = \boldsymbol{v_2}$, **and** $u_4^e = \boldsymbol{\phi_{x2}}$.

The top foil transverse deflection (w_d) along the circumferential coordinate (x) is governed by the fourth order differential equation:

$$\frac{d^2}{dx^2}\left(E_t I \frac{d^2 w_d}{dx^2}\right) = q\left(x\right)\cdot L \tag{4}$$

where E_t and I are the plate elastic modulus and area moment of inertia, and $q{\cdot}L{=}(p{-}p_a)\cdot L$ is the distributed load per unit circumferential length. Note that Eq. (4) is the typical formulation for the deflections of an *Euler beam-like* model. Reference [70] details the weak form of Eq. (4) when integrated over the domain of a finite element. Presently, the elastic modulus for the top foil (E_t) is artificially increased, $E_t{}^* = E_t \times S_{fc}$, where ($S_{fc}$) is a stiffening factor along the circumferential direction. Rationale for its implementation is detailed below.

Two dimensional model for top foil

The second model regards the top foil as a two dimensional flat shell supported on axially distributed linear springs located at every bump pitch, as shown in Fig. 6. Figure 7 depicts the membrane stress (N) on graph (a); and shear (Q) and bending (M) stresses on graph (b), due to pressure difference ($q{=}p{-}p_a$) acting on the shell element OABC. The generic displacements are denoted as u, v and w along the x, y and z directions, respectively.

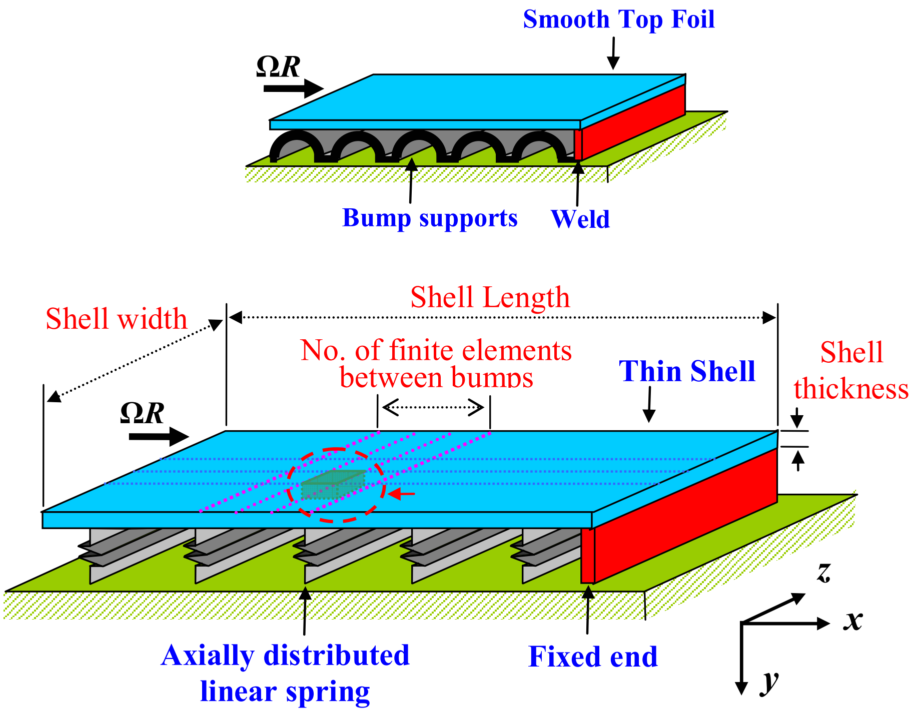

Figure 6 Configuration of top foil supported on a bump strip and its 2D structural model.

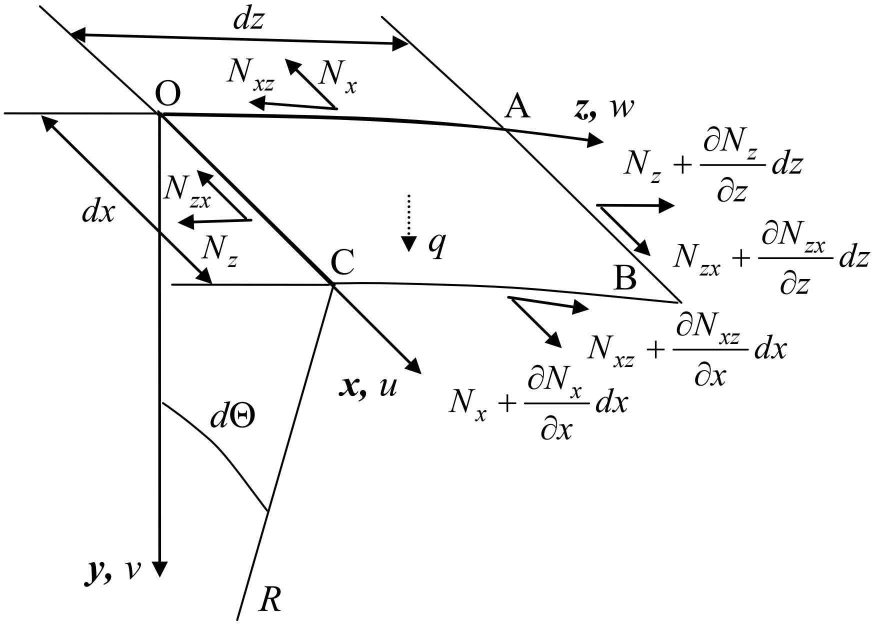

(a) Normal plane (membrane) stresses

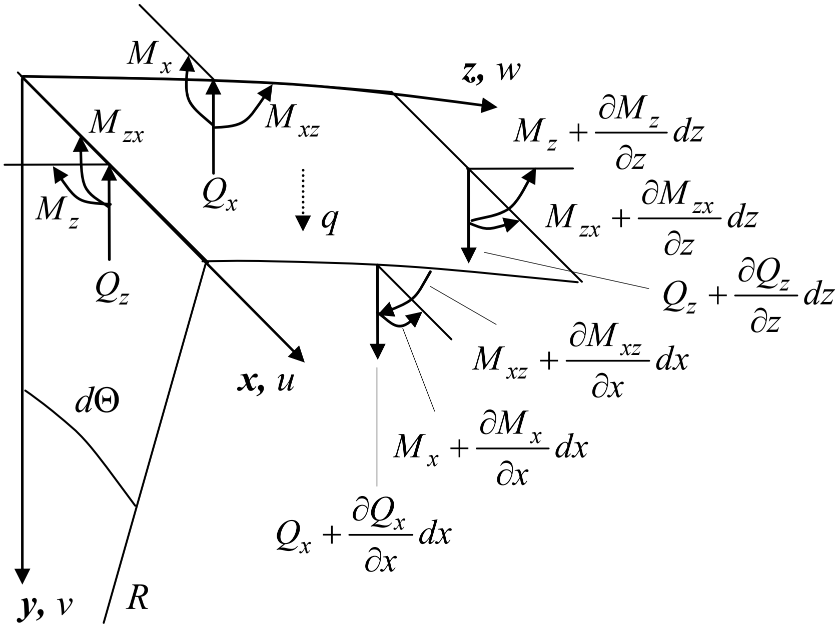

(b) Bending and shear stresses

Figure 7 Resultant membrane forces and bending moments per unit shell element length for a distributed load in the domain of a shell finite element.

Timoshenko and Woinowsky-Krieger [71] detail the elasticity equations for the general cases of deformation in a cylindrical shell. In the present structural configuration, membrane or in-plane forces (N) are negligible since the axial (side) ends of the top foil are regarded as free (not constrained) and because the gas film pressure acts normal to the top foil. Gas film shear forces between the film and top foil, and dry-friction forces between the top foil and bumps underneath do induce membrane forces. However, these are neglected for simplicity.

Figure 8 displays schematic representations of the actual and idealized structural deformations for the top foil and adjacent bumps. In actual operation, the bumps are flattened under the action of the acting pressure, the contact area with the top foil increases, and this effect increases locally the stiffness of the top foil. Hence, an anisotropic elastic model using $E_t{}^* = E_t \times S_{fc}$ compensates for the overestimation of top foil deflections between adjacent bumps. Note that the curvature radius of the top foil deflected shape (*sagging*) cannot exceed that of the original bumps shapes, thus suggesting the appropriate range of stiffening factors for known GFB configurations.

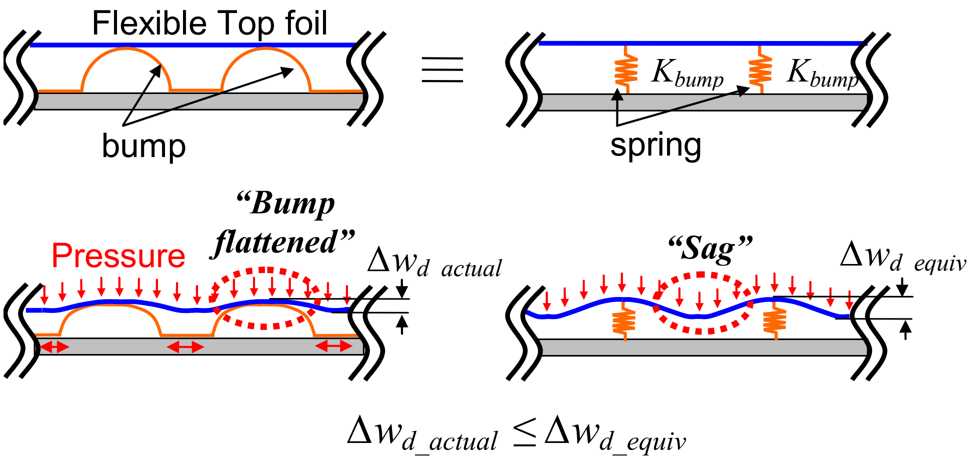

(a) Foil deflections in actual GFBs (b) Foil deflections for equivalent model

Figure 8 Schematic representations of deformations in actual and idealized top foil and bump strips (1D and 2D models).

Thus, the present analysis uses the anisotropic, shear deformable plate model based on first-order shear deformation theory [70]. The governing equations are detailed in Appendix A.

A bump is modeled as an axially distributed linear spring, and the FE bump stiffness matrix [$\boldsymbol{K}^s$] is derived from the bump stiffness per unit area, K_f [72]. K_f is estimated using Iordanoff's [23] analytical expressions for a bump with both sides free, or one end free and the other fixed. Although the formulas in [23] include provisions for a dry friction coefficient, at present none is being used. Note that when considering the dynamic behavior of a bump support, a complex stiffness, $K'_f = K_f\,(1+i\gamma)$, is easily defined to account for a material loss factor (γ) arising from hysteresis and dry-friction.

The global FE stiffness matrix [$\boldsymbol{K}^G$] $=\cup$ {[$\boldsymbol{K}^e$]+ [$\boldsymbol{K}^s$]} adds the bump stiffness matrix [$\boldsymbol{K}^s$] to the flat shell element stiffness matrices [$\boldsymbol{K}^e$]. The global stiffness matrix [$\boldsymbol{K}^G$] is reduced by considering the geometric constraints along the top foil fixed end, i.e., $v = \phi_x = \phi_z = 0$ where v depicts top foil transverse deflection (w_d). ϕ_x and ϕ_z are rotation angles about the z and x axes, respectively.

Without journal misalignment, the pressure field is symmetric about the bearing mid plane. In this case, the FE procedure models only one half side of the top foil and support bumps. The global system of equations for deflections of the top foil and bump supports is given by

$$\left[\boldsymbol{K}^{\boldsymbol{G}}\right]\left\{\boldsymbol{U}^{\boldsymbol{G}}\right\}=\left\{\boldsymbol{F}^{\boldsymbol{G}}\right\} \tag{5}$$

where $[\boldsymbol{K}^{\boldsymbol{G}}]$ is a symmetric, positive definite matrix, $\{\boldsymbol{U}^{\boldsymbol{G}}\}$ is the vector of generalized deflections (transverse displacement and rotations), and $\{\boldsymbol{F}^{\boldsymbol{G}}\}$ is the vector of generalized forces, namely pressures acting on the top foil.

Prior to computations coupling the structure deflections to the thin film gas flow governed by Reynolds Eq. (1), the global stiffness matrix, derived from the 1D and 2D FE models, is decomposed using Cholesky's procedure [73]. Note that the FE structural model analysis is performed off-line. In this manner, the computational efficiency of the numerical scheme is greatly enhanced. The transverse deflection field (w_d) is extracted from $\{\boldsymbol{U}^{\boldsymbol{G}}\}$ and used to update the film thickness for solution of Reynolds equation within the framework of an iterative scheme.

Results and Discussion

Comparisons of predictions to published test data

***Configuration of test GFB*:** The validity of the analysis and computational program is assessed by comparison of predictions to experimental data available in the open literature. Table 1 provides parameters for the test "first generation" foil bearing given in [32]. The top foil and single bump strip layer are spot welded at one end to the bearing sleeve. The other end of the top foil is free as well as the end of the bump strip layer. The journal rotational direction is from the free end of the top foil towards its fixed end. The structural stiffness per unit area (K_f) is estimated from Iordanoff's formulae [23]; K_{ff} = 4.7 GN/m^3 for a free-free ends bump and K_{fw} = 10.4 GN/m^3 for a fixed-free end bump.

Table 1 Design details of foil bearing, reference [32].

Bearing radius, $R=D/2$	19.05 mm (0.75 inch)
Bearing length, L	38.1 mm (1.5 inch)
Foil arc circumferential length, l_x	120 mm (4.7 inch)
Radial journal travel, c	31.8 μm (1.25 mil)
Top foil thickness, t_t	101.6 μm (4 mil)
Bump foil thickness, t_b	101.6 μm (4 mil)
Bump pitch, s_0	4.572 mm (0.18 inch)
Half bump length, l_0	1.778 mm (0.07 inch)
Bump height, h_b	0.508 mm (0.02 inch)
Number of bumps, N_b	26
Bump foil Young's modulus, E_b	214 Gpa (31 Mpsi)
Bump foil Poisson's ratio, ν_b	0.29

All tests were performed with air at ambient temperature conditions. Although the measured bearing temperature changes from 29 ºC to 57 ºC during a series of static load tests, the present analysis assumes a constant gas temperature of 27 ºC. In [32], the authors report a nominal diametrical clearance, $2c$=63.6 μm, based on an ad-hoc procedure displacing the journal with small static loads. The actual bearing clearance is not reported.

***Minimum film thickness and journal attitude angle*: **The GFB computational tools integrating the 1D and 2D finite element top foil structural models, as well as the earlier simple elastic foundation model [31], predict the static and dynamic force performance of the test GFB.

The 2D FE model uses a mesh of 78 and 10 elements in the circumferential and axial directions, respectively. The same mesh size is used for the finite difference numerical scheme solving Reynolds Eq. and calculating the hydrodynamic gas film pressure. On the other hand, the 1D FE model uses a mesh of 78 elements in the circumferential direction. A mesh of 78 and 10 elements, in the circumferential and axial directions, respectively, is used to analyze the gas film pressure. Predictions using the simple elastic foundation model, for a mesh of 90 and 10 elements in the circumferential and axial directions, respectively, are directly taken from [20].

A top foil stiffening factor S_{fc}= 4 in the circumferential direction was obtained through parametric studies based on the recorded test data in [32], and is used in both 1D and 2D FE models. In the 2D FE model, foil deflections along its edges are calculated using the axial upstream pressures modified by the local Peclet number [74], a procedure based on physical reasoning which improves the accuracy in the prediction in the gas film thickness. Note that 2D FE predictions overestimate the top foil deflections when compared to the test data in [32]. This behavior may be due to the omission of membrane stresses in the current model.

Figure 9 presents the minimum film thickness versus applied static load for operation at shaft speeds equal to (a) 45,000 rpm and (b) 30,000 rpm. The graphs includes the test data [32], and predictions for three increasingly complex structural models; namely, the simple elastic foundation, 1D top foil acted upon an axially averaged gas pressure, and the 2D top foil. In the tests, film thicknesses were recorded at both the bearing mid-plane and near the bearing exit-planes, i.e. 1.6 mm from the bearing axial ends. The 2D model predictions show minimum film thicknesses along the bearing mid-plane and near the bearing edges, i.e. 1.9 mm away. Both the simple elastic model and the 1D FE model predictions show a film thickness not varying across the bearing width since the models rely on an axially averaged pressure field.

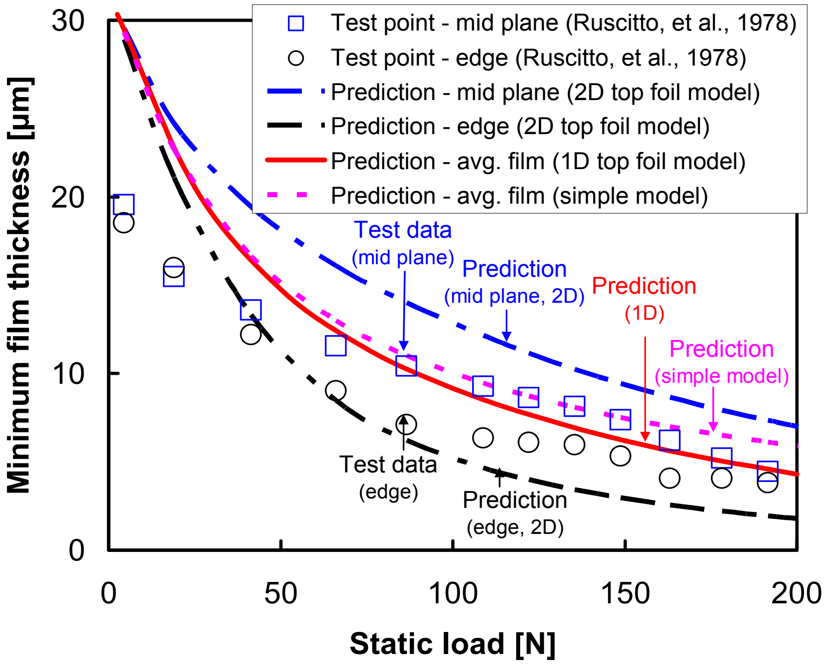

(a) 45,000 rpm

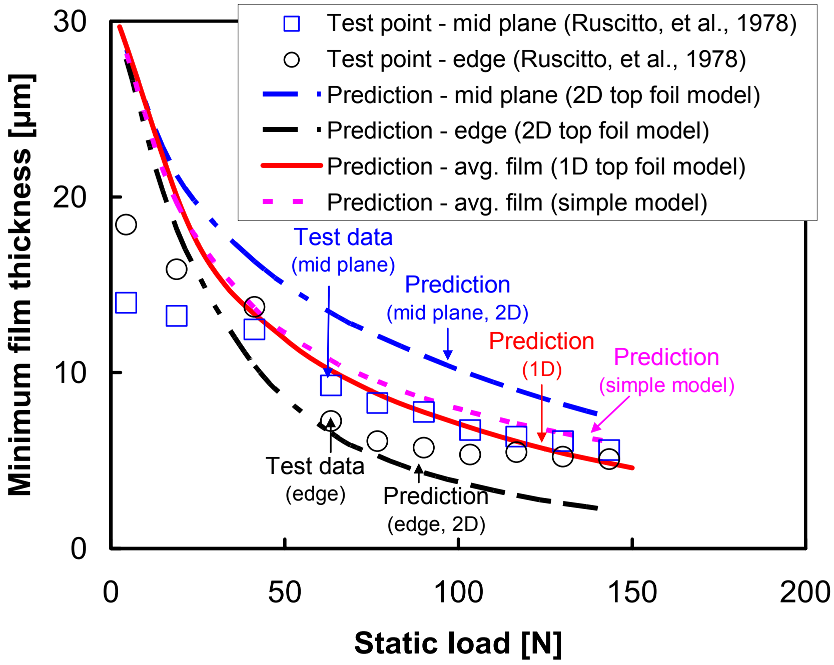

(b) 30,000 rpm

Figure 9 Minimum film thickness versus static load. Predictions from three foil structural models and test data [32].

In general, all model predictions agree fairly with the test data [32]. Incidentally, the measurement errors reported in [32] render a precision uncertainty of ~15 % for film thickness.

Over the whole range of static loads, 2D top foil model predictions overestimate the minimum film thickness at the bearing mid-plane, and slightly underestimate this parameter at the top foil edge. The discrepancies are due to membrane forces preventing the extension of the top foil. Membrane forces produce a uniform deflection along the bearing width, in particular for heavy static loads. This effect is most notable for a uniform pressure field along the bearing width. The assumption of an axially uniform minimum film thickness in the 1D top foil model results in a significant reduction of computational costs. More importantly, the 1D top foil model predictions show the best correlation to the collected experimental results. The simpler model predictions slightly overestimate the minimum film thickness, especially for heavy static loads. From the comparisons, it is inferred that a too large bump pitch or a too thin top foil may cause a significant decrease in load capacity, as also demonstrated experimentally in [75].

Figure 10 depicts the journal attitude angle versus applied static load for speeds equal to (a) 45,000 rpm and (b) 30,000 rpm, respectively. The graph includes predictions from the three structural models and test data [32]. All model predictions slightly underestimate the test data above 60 N. The notable discrepancy between predictions and test results for static loads below 60 N can be attributed to foil bearing fabrication inaccuracy [32]. In general, all model predictions agree well with the test data, although the 1D top foil model predictions are best.

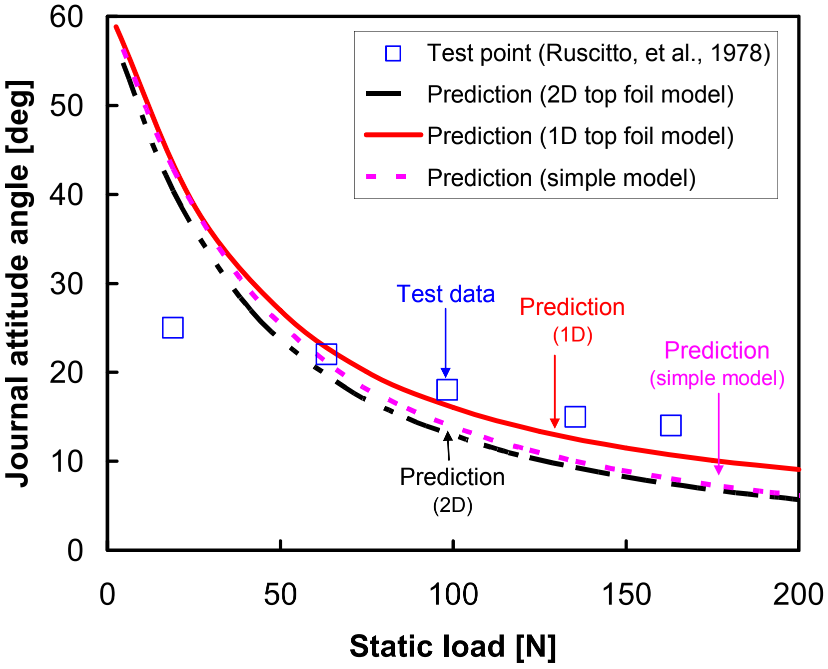

(a) 45,000 rpm

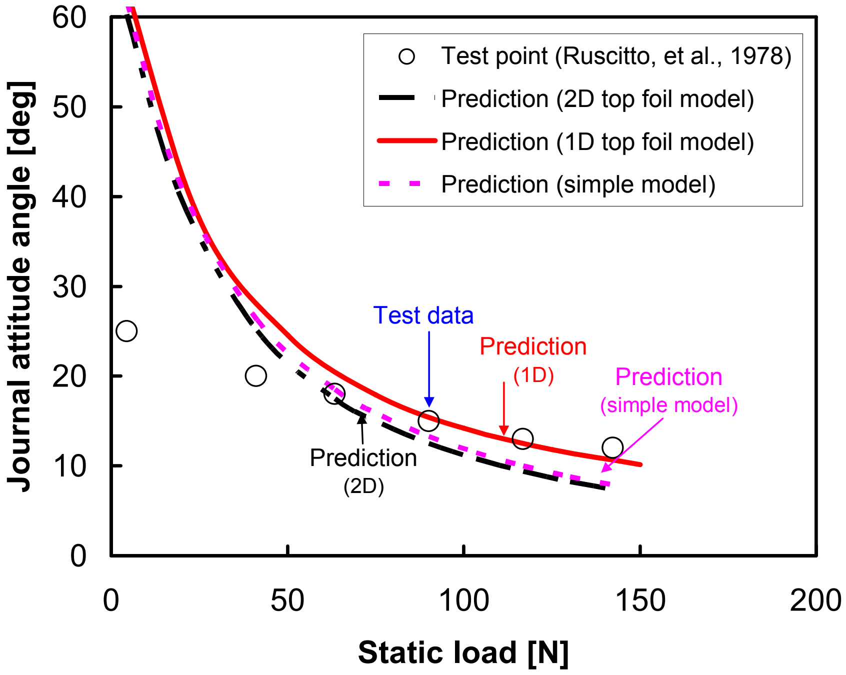

(b) 30,000 rpm

Figure 10 Journal attitude angle versus static load. Predictions from three foil structural models and test data [32].

Figure 11 displays the predicted pressure field (p/p_a) and the corresponding foil deflection (w_d) derived from the 2D top foil structural model. The results are presented for one half side of the bearing, i.e., from z=0 to z=L/2. A static load of 200 N, specific pressure = 138 kPa (20 psi), acts on the rotor operating at 45,000 rpm. During operation, the top foil could detach, not allowing for sub-ambient pressures, i.e. $p \geq p_a$ [31]. The pressure is nearly constant along the bearing axial length except at the axial edges. Due to the bearing inherent compliance, the model prediction shows a large top foil deflection, in particular, around the peak pressure zone. The softness of the top foil in between individual bumps causes the local pressure field to sag between consecutive bumps, i.e. the appearance of a "*ripple*" like effect.

Figure 12 presents the predicted film thickness versus circumferential location for the 1D top foil model and the measured film thickness [32] for a static load of 134.1 N and rotor speed of 30 krpm. For the heavily loaded condition, the model prediction shows a large circumferential region of uniform minimum film. Along the zone of smallest film thickness, the predictions match very well with the test data. Recall that the model does not account for the interaction between adjacent bumps, thus showing a slight difference in the pitch of the *ripple* shapes. Note that the test GFB has a nearly constant film thickness along the bearing axial length (Δh < 1μm) for both load and speed conditions, as shown in Fig 9 (b).

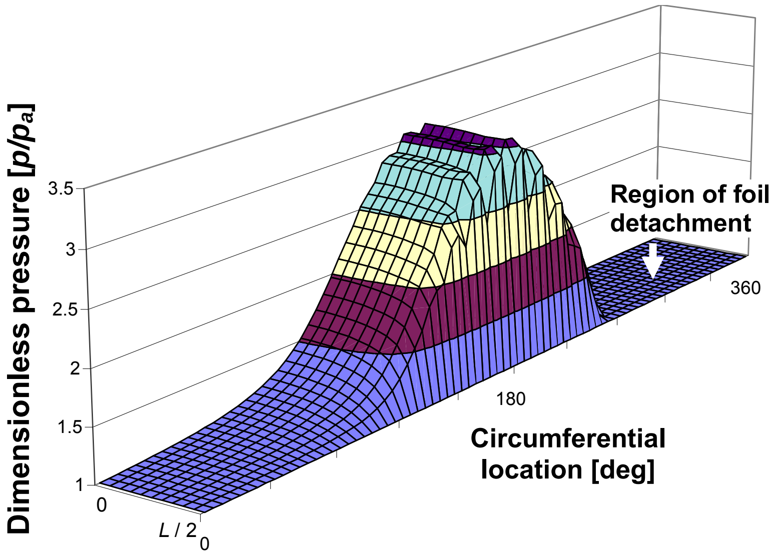

(a) Pressure field

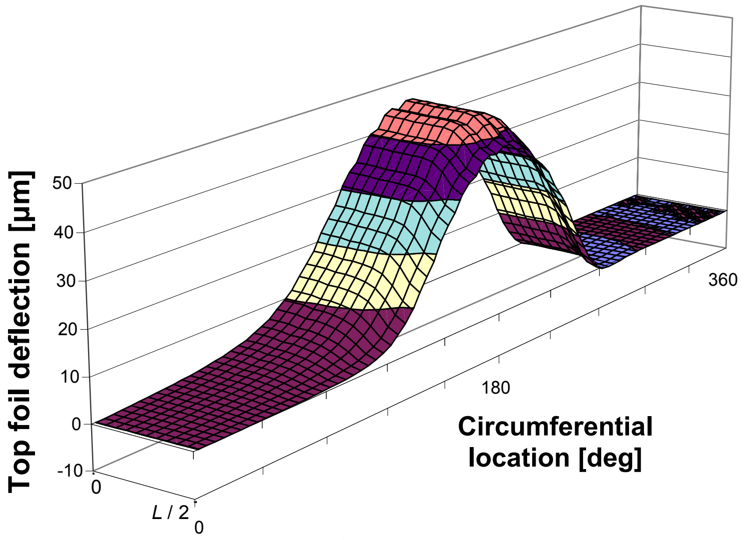

(b) Top foil deflection field

Figure 11 Predicted (a) dimensionless pressure field and (b) top foil deflection field from 2D top foil structural model. Static load: 200 N, rotor speed: 45 krpm. Bearing configuration given in [32].

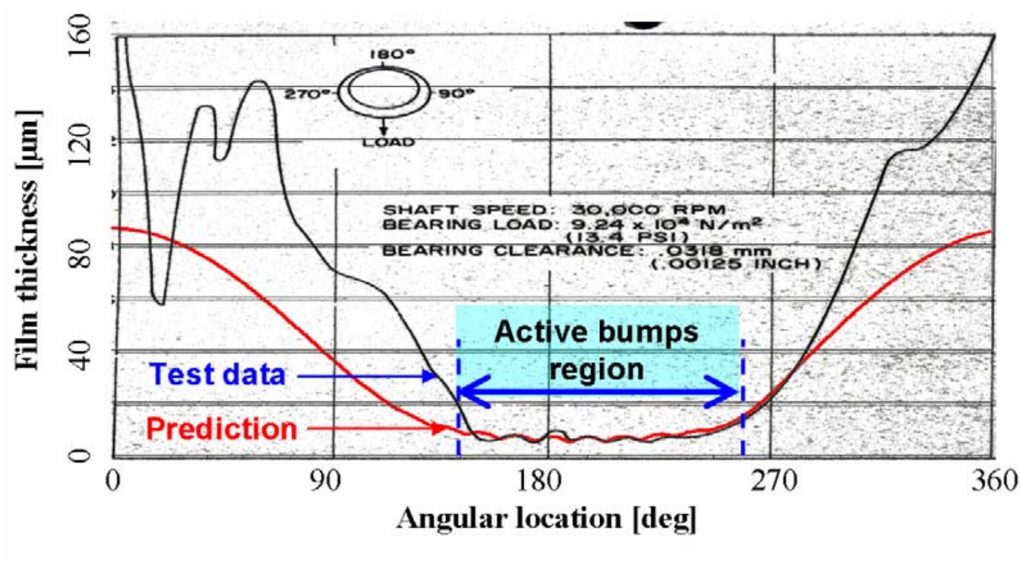

Figure 12 Film thickness versus angular location at bearing mid-plane. Prediction from 1D top foil model and test data [32]. Static load: 134.1 N. Rotor speed: 30 krpm.

Although the test GFB in [32] has unknown radial clearance, the comparisons demonstrate a remarkable correlation between predictions and measurements in the region of minute, nearly uniform, film thickness. These comparisons validate the 1D top foil model for accurate prediction of GFB static load performance.

Predicted stiffness and damping force coefficients

To date there are no published comprehensive test data on GFB force coefficients, stiffness and damping. Recent work by Lee et al [35] advances an identification method and presents frequency-independent force coefficients. Unfortunately, the named reference does not give details on the test bearing geometry and experimental identification conditions.

Figure 13 displays predicted GFB stiffness coefficients versus excitation frequency as determined by the three structural support models. A static load of 150 N, i.e. specific load of 1 bar (15 psi), is applied at 45,000 rpm. Synchronous excitation corresponds to a frequency of 750 Hz. Note the difference in vertical axis scales in Fig. 13(a-c). The direct stiffness coefficients (K_{XX}, K_{YY}) increase with excitation frequency due to the "hardening" effect of the gas film.

All models predict very similar direct stiffness coefficients. The simple elastic foundation model offers the largest direct stiffness, K_{XX}, while the 2D top foil model renders the smallest. The elastic *"sagging"* effect of the top foil in between adjacent bumps in the 1D and 2D FE models is thought to reduce slightly the direct stiffness K_{XX}. All predictions of cross-coupled stiffness coefficients show positive values. Note that $(K_{XY} - K_{YX}) > 0$ may induce dynamic destabilizing effects. The 1D top foil model predicts the largest K_{XY} and the smallest K_{YX}. The 2D model predicts the smallest K_{XY}, while the simple model predicts the largest K_{YX}. All model predictions demonstrate much greater direct stiffnesses, K_{XX} and K_{YY}, than cross-coupled stiffnesses, K_{XY} and K_{YX}.

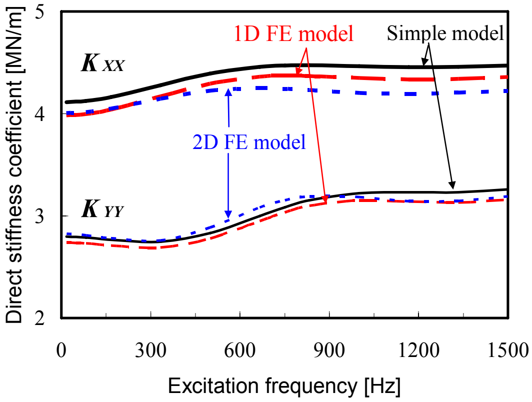

(a) K_{XX}, K_{YY}

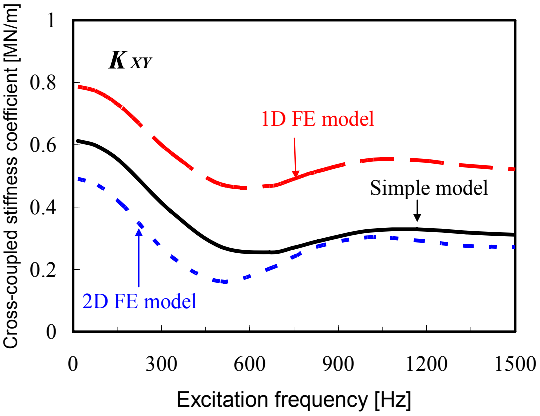

(b) K_{XY}

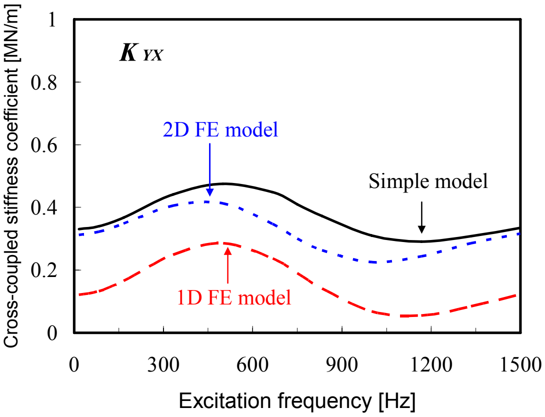

(c) K_{YX}

Figure 13 Predicted GFB stiffness coefficients versus excitation frequency for three structural models. Rotor speed: 45 krpm, Static load: 150 N. Structural loss factor $\gamma = 0.0$.

Figure 14 displays predicted damping coefficients versus excitation frequency as determined from the three structural models. Static load and rotor speed are as in the prior figure. The structural loss factor $\gamma = 0.4$ represents a typical hysteresis damping effect in the bump strip layer [76,77]. Note that the vertical axes of Figs. 14 (a) and 14 (b) show a log scale, while Figs. 14 (c) and 14 (d) show a linear scale along the vertical axes. All model predictions demonstrate much greater direct damping coefficients, C_{XX} and C_{YY}, than cross-coupled damping coefficients, C_{XY} and C_{YX}. With a structural loss factor ($\gamma = 0.4$), direct damping C_{XX}, C_{YY} increase significantly when compared to those for $\gamma = 0.0$, i.e. without material damping. Regardless of the structural loss factor, the 2D top foil model predicts the smallest direct damping coefficients (C_{XX}, C_{YY}). The simple elastic foundation model prediction shows the largest coefficients, except for excitation frequencies lower than 500 Hz, where the 1D FE model predicts the largest C_{XX} and C_{YY} for $\gamma = 0$. Predictions of cross-coupled damping coefficients, C_{XY} and C_{YX}, do not show a discernible difference among the three models. Generally, cross-coupled damping coefficients (C_{XY}, C_{YX}) decrease in magnitude as the excitation frequency increases.

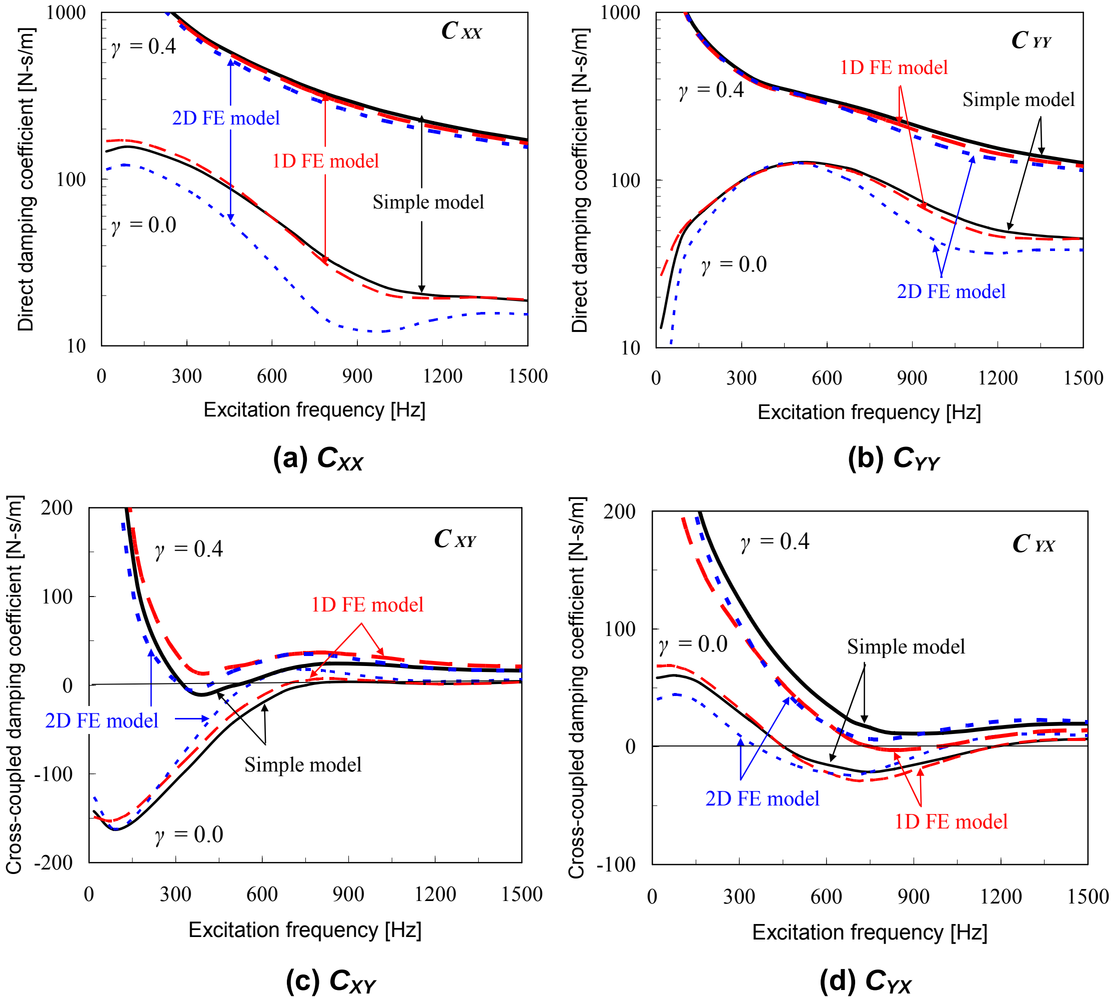

(a) C_{XX}

(b) C_{YY}

(c) C_{XY}

(d) C_{YX}

Figure 14 Predicted GFB damping coefficients versus excitation frequency for three structural models. Rotor speed: 45 krpm, Static load: 150 N. Structural loss factors, γ = 0.0 and 0.4.

Conclusions

Simplified analyses of GFBs neglect the elasticity of the top foil and consider the bump-strip-layers support structure as an elastic foundation with uniform stiffness. This simple model has been most useful for decades; however, stringent applications of gas bearings into commercial oil-free turbomachinery demands the development of more realistic models to better engineer them as reliable supports.

Presently, the chapter introduces two accurate finite element models for the top foil elastic structure. The simplest FE model assumes the top foil as a 1D thin beam-like structure with negligible deflections along the axial coordinate, i.e. very stiff and acted upon by a uniformly distributed pressure field. The second FE model, 2D, takes the top foil as a flat shell with anisotropic material properties with a stiffening factor along the circumferential direction. The underlying bumps modeled as a uniform elastic foundation along the edge of a typical finite element representing a top foil, are directly integrated into a global stiffness matrix that relates the top foil (and bump strips) deflections to applied gas film pressure or contact pressure, depending on the operating condition. The decomposition of the symmetric stiffness matrix is performed off-line and prior to computations coupling it to the gas bearing analysis. The procedure greatly enhances the computational efficiency of the numerical scheme.

Predictions of GFB attitude angle and minimum film thickness for increasing static loads and two shaft speeds are compared to published test data. The predictions presented correspond to three models: (a) simplest elastic foundation with no accounting for top foil structure, (b) 1D FE model with top foil as a thin beam, and (c) 2D FE model with top foil as a shell. 2D FE model predictions overestimate the minimum film thickness at the bearing centerline, but underestimate it at the bearing edges. Predictions from the 1D FE model compare best to the limited tests data; reproducing closely the experimental circumferential profile of minimum film thickness. The 1D top foil model is preferred due to its low computational cost. The FE models predictions show local *ripples* in the top foil supported in between bumps. The *ripples* are a pathway for gas to escape the bearing, thus decreasing the hydrodynamic pressure and diminishing the bearing load carrying capacity. Predicted stiffness and damping coefficients versus excitation frequency show that the two FE top foil structural models results in slightly lower direct stiffness and damping coefficients than those from the simple elastic foundation model. Note that staggered bump strip layers may improve the ultimate load capacity as well as dynamic forced performance of GFBs by reducing the sagging of the top foil between adjacent bumps.

The present FE model first presents accurate predictions of the “sagging” of the top foil between adjacent bumps. The sagging effect is more apparent at a heavily loaded condition. A parametric study anchored to test data proposes an appropriate stiffening factor to increase the top foil stiffness due to increasing contact area between the top foil and bump supports. Results of this study provide a design guidance for advanced GFBs.

CHAPTER IV

EXPERIMENTAL VERIFICATION OF THE EFFECT OF SIDE END PRESSURIZATION ON THE PERFORMANCE OF GFBS

Introduction

This chapter describes experimental results of the rotordynamic performance of a rotor supported on two GFBs with side end pressurization. Rotor speed run-up tests first demonstrate the beneficial effects of side end pressurization into GFBs on the onset rotor speed of subsynchronous motions. A sufficiently high side end pressure[2] effectively delays the onset rotor speed of subsynchronous motions.

The experimental test results are unique in that normalized synchronous amplitudes recorded during rotor speed coastdown tests reveal a linear rotor response behavior. Rotor run-out is excluded by subtraction of the baseline imbalance response (amplitude and phase). Rotordynamic parameter identification[3] delivers similar effective GFB stiffness and damping coefficients from tests conducted with small and moderately large imbalance masses. A large rotor imbalance mass added on the rotor causes an increase in normalized synchronous amplitudes for shaft speeds enclosing the rotor-bearing system critical speed, apparently due to a reduction in viscous damping. More importantly, a large imbalance mass leads to a decrease in the onset rotor speed of subsynchronous whirl motions which appear at 1/3 whirl frequency ratio. Note that these test results imply a forced nonlinearity due to the foil bearing nonlinear (hardening) stiffness characteristics as determined from static load – deflection measurements [80].

---

[2] Pressurized feed air is often needed to cool GFBs as well as the integral drive motor (or generator) mounted between GFBs in oil-free micro turbomachinery.

[3] To date, there is little experimental evidence on GFB rotordynamic force coefficients. The present study uses a one degree of freedom rigid rotor model to estimate the effective stiffness and damping coefficients of test GFBs.

Experimental Procedure

Rotordynamic response measurements for increasing imbalance masses are conducted on a rotor supported on GFBs. The bearings are air pressurized at one end only; the other end is exposed to ambient pressure. Ref. [78] details the geometry and materials of the test rotor and second generation GFBs. Briefly, the rotor weighs 1 kg, and the GFB length L and shaft diameter ($2R_J$) are 38.1 mm, with estimated sway radial clearances of c = 40 and 70 um for the drive and free end GFBs, respectively. Figure 15 shows the GFB test rig for the rotordynamic experiments. The test rig housing holds two test GFBs and contains an internal duct to supply air pressure up to 7 bars (100 psig) for cooling the bearings, if needed. Uncertainty in the controlled pressures is ± 0.14 bar (±2 psig). The air pressurization at rotor midspan forces a cooling flow through the test GFBs. A 0.75 kW (1 HP) AC electric motor with maximum speed of 50 krpm drives the test rotor through a flexible coupling. A router AC motor, 1.49 kW (2.0 HP) with maximum speed of 25 krpm, aids the driving motor to start up the test rotor through a centrifugal clutch before the rotor lifts off from its bearings. Two pairs of orthogonally positioned eddy current sensors located at both rotor ends record the lateral rotor motions along the horizontal and vertical planes. The eddy current sensors, Bently 7200 8 mm [79], have a 2 mm linear range and an incremental scale factor of 7.87 mV/μm ±5% error, i.e. ±0.25 μm/0.1 mV error, between 0 ºC and 45 ºC. Test data are collected using Bently Neveda ADRE® data acquisition system. See Ref. [78] for a more detailed description of the test rig and bearings.

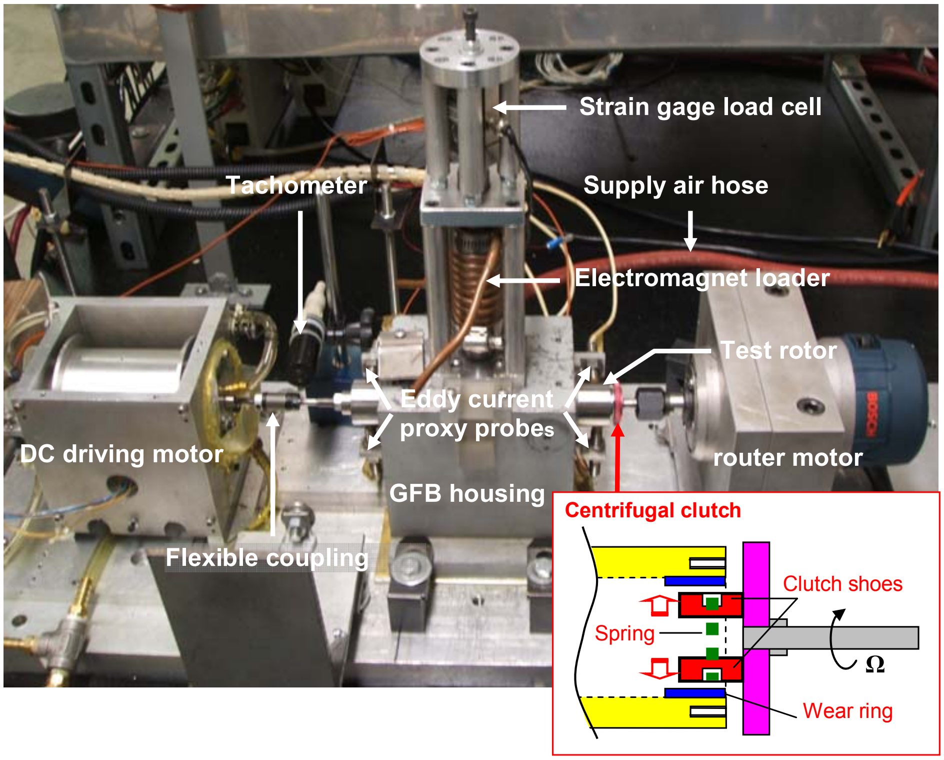

Figure 15 Test rig for rotordynamic tests of a rotor supported on GFBs [78].

Tests are conducted at ambient temperature, T = 293° K. Ref. [78] shows severe subsynchronous rotor motions above 26 krpm at a side end pressure of 0.35 bar (5 psig). The large amplitude whirl motions reach limit cycles with frequencies coinciding with the low natural frequency rigid body modes of the rotor bearing system. At rotor speeds lower than 26 krpm, no subsynchronous motions are observed. Normalized synchronous amplitudes show a linear rotor response behavior when using moderately small imbalance masses of 55 mg, 110 mg, and 165 mg. These results are in opposition to those in [17]; increasing normalized synchronous amplitudes with increasing imbalance masses. Note that only a well balanced rotor in [78] ensures a linear rotor behavior.

Presently, further imbalance response measurements are conducted at a side end pressure of 0.35 bar (5 psi) for in-phase and out-of-phase large imbalance mass of 330 mg, i.e. six times the lowest imbalance mass of 55 mg. Normalized rotor amplitudes and phase angles of the measured synchronous responses with the large imbalance mass are compared to those with small to moderate imbalance masses in [78]. A one degree of freedom mechanical system model aids to identify the natural frequency, effective stiffness, and damping ratio of the test GFBs.

Table 2 shows the imbalance masses added into the rotor end planes at radius (r) equal to 15.11 mm. The table includes the masses angular disposition (in-phase and out-of-phase) as well as the equivalent imbalance displacements (u).

Table 2 Imbalance masses, equivalent imbalance displacements, and their location at rotor end planes.

Imbalance test type		Imbalance mass (m_e)		Imbalance displacement (u)	
		Drive end	Free end	Drive end	Free end
In-phase	Test 1	55 mg (-45º)	55 mg (-45º)	1.26 µm	2.34 µm
	Test 2	110 mg (-45º)	110 mg (-45º)	2.52 µm	4.67 µm
	Test 3	165 mg (-45º)	165 mg (-45º)	3.78 µm	14.0 µm
	Test 4	330 mg (-45º)	330 mg (-45º)	7.56 µm	7.56 µm
Out-of-phase	Test 1	55 mg (-45º)	55 mg (135º)	1.26 µm	2.34 µm
	Test 2	110 mg (-45º)	110 mg (135º)	2.52 µm	4.67 µm
	Test 3	165 mg (-45º)	165 mg (135º)	3.78 µm	7.00 µm
	Test 4	330 mg (-45º)	330 mg (-45º)	7.56 µm	14.0 µm

Imbalance displacement, $u_i = m_e \times r / M_i$, $_{i=DE,\, FE}$.

Uncertainty in imbalance masses (m_e) is ±1mg with correspondent uncertainty in imbalance displacement (u) equal to ±0.042 µm.

The masses (M_{DE} , M_{FE}) represent a fraction of the rotor weight (divided by gravity) acting on each bearing: 0.66 kg and 0.36 kg for drive end and free end bearings, respectively. The coupling force is not considered for the static load distribution.

Rotor speed-up tests are also conducted on the same rotor supported on side end pressurized GFBs for small to moderate imbalance masses of 55 mg, 110 mg, and 165 mg. The bearings are air pressurized at one end only; the other end is exposed to ambient pressure. The air supply pressure level is controlled manually.

Processing of the test data reveals the onset rotor speeds of subsynchronous whirl motions for increasing side end pressures of 0.35 bar (5 psig), 1.4 bar (20 psig), and 2.8 bar (40 psig). Rotor speed coastdown tests from 25 krpm[4] are conducted for increasing side end pressures.

Three metal shims of 25.4 μm thickness, 8.6 mm width, and 38.1 mm length are installed under the bump strip and in contact with the bearing housing at three angular locations. Figure 16 shows the schematic views of the original test GFB and the modified GFB with three shims. The original test GFB consists of five bow like bump strips, each with five bumps. The end of a bump strip is welded to the bearing sleeve while the other end is free. The top foil, coated with a spray-on Teflon® type coating of thickness 25.4 μm, consists of a thin metal sheet welded at the bearing sleeve at one end (spot weld) and free at the other end. Figure 16 notes the orientation of the top foil spot-weld with respect to the vertical (gravity) plane is noted. Table 3 lists the geometry and material properties of the test GFB with shims. Each shim has an angular extension of 26 °, and the arc distance between adjacent shims is 120 °.

A rotor speed-up (acceleration) test determines the threshold speed of instability where subsynchronous motions suddenly begin to increase. The side end pressure is manually increased from 0.35 bar (5 psig) to 4.1 bar (60 psig) during the rotor speed-up tests to 50 krpm. Imbalance rotor responses are measured during coastdown tests from 35 krpm[5] for in-phase and out-of-phase imbalance masses of 55 mg and 110 mg. Normalization of the synchronous rotor amplitudes aids to verify the linearity of the system response within the speed range of 0 to 35 krpm. The measured synchronous and subsynchronous rotor motions for increasing side end pressures are analyzed. In

---

[4] Onset speed of subsynchronous rotor motions for a side end pressure of 0.35 bar supplied to the original GFBs.

[5] Onset speed of large subsynchronous rotor motions for air pressure of 0.35 bar supplied to the test GFBs with shims.

addition, the estimated loci of static rotor centerline are compared for tests with increasing end gas pressure into the bearings.

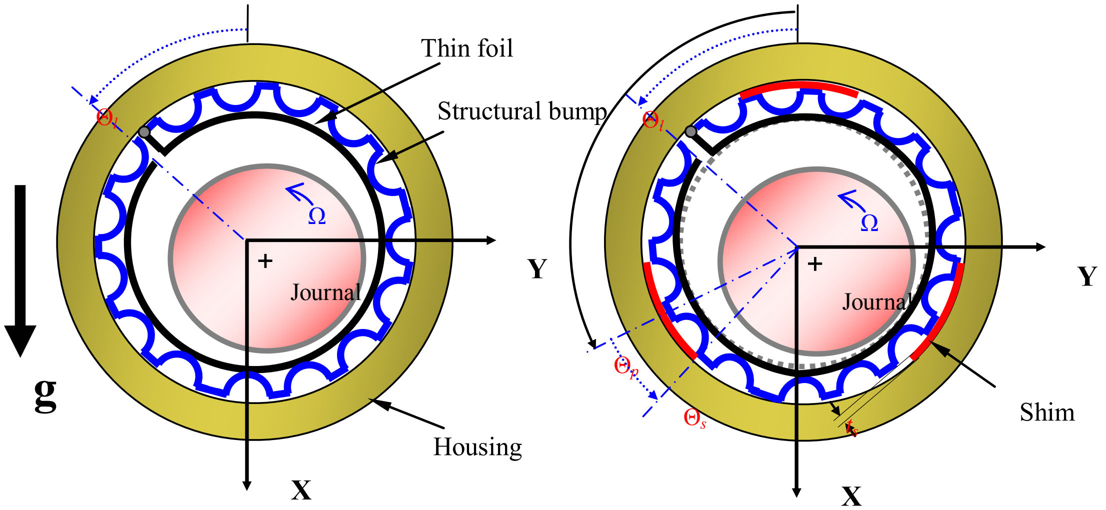

(a) Gas foil bearing **(b) Gas foil bearing with three shims**

Figure 16 Schematic views of original test GFB and modified GFB with three metal shims. Locations of top foil leading edge and shims relative to vertical plane as in tests.

Table 3 Geometry of modified GFB with shims.

Bearing	Radius, *R=D/2*	19.05 mm	(0.75 inch)
	Length, *L*	38.1 mm	(1.5 inch)
	Top foil arc circumferential length, l_x	120 mm	(4.7 inch)
	Angular distance between top foil leading edge and vertical plane, Θ_l	45 °	
Shims	Angular distance between adjacent shims, Θ_p	120 °	
	Axial length, L_s	38.1 mm	(1.5 inch)
	Thickness, t_s	25.4 µm	(1.0 mil)
	Width, w_s	8.6 mm	(0.34 inch)
	Angular extent, Θ_s	26 °	
	Number, N_s	3	
	Material	Steel	
Bump	Pitch, *p*	4.572 mm	(0.18 inch)
	Length, l_o	4.064 mm	(0.16 inch)
	Foil thickness, *t*	0.102 mm	(4.0 mil)
	Height, *h*	0.381 mm	(15 mil)
	Poisson's ratio, *v*	0.29	
	Bump modulus of elasticity, *E*	213 GPa	(30.9 Mpsi)
	Dry friction coefficient, *μ* (estimated)	0 - 0.25 [49]	

Measurements of Rotor Motion in Test Rotor-GFB System: Original GFBs Configuration

Onset speed of subsynchronous motions (rotor speed-up tests)

A rotor speed-up (acceleration) test identifies the onset speeds of subsynchronous rotor motion for increasing side end pressures. The rotor speed is manually controlled to accelerate the rotor from the minimum motor control speed (10 krpm) to rotor speeds well above the onset speeds. Figures 17 (a) and (b) display waterfall plots of vertical motion recorded at the rotor free end for side end gauge pressures of 0.35 bar (5 psig) and 2.8 bar (40 psig), respectively. Subsynchronous motion of large amplitude is evident as the rotor speed increases. Figure 18 depicts the amplitudes of rotor synchronous and subsynchronous motions recorded at the rotor free end for side end pressures of 0.35 bar (5 psig), 1.4 bar (20 psig), and 2.8 bar (40 psig). With a low feed pressure of 0.35 bar, the onset speed of subsynchronous motion (N_{os}) is 25 krpm. This rotor onset speed increases to 30.5 krpm as the side end gauge pressure is raised to 2.8 bar.

As vividly shown in Figure 19, FFT spectra of shaft motions at a shaft speed of 30 krpm (500 Hz), the severity of subsynchronous amplitudes is directly related to the amount of side end pressurization. The frequency of subsynchronous whirl corresponds with a rigid body natural frequency the rotor-GFBs system. This natural frequency changes little with the magnitude of side end pressurization. Figure 20 shows the dramatic effect of end gas pressurization on reducing the total amplitude of motion, mainly composed of the subsynchronous whirl motions. For $P_s \geq 2.8$ bar the rotor subsynchronous whirl motions disappear; i.e. the test system is rotordynamically stable at 30 krpm.

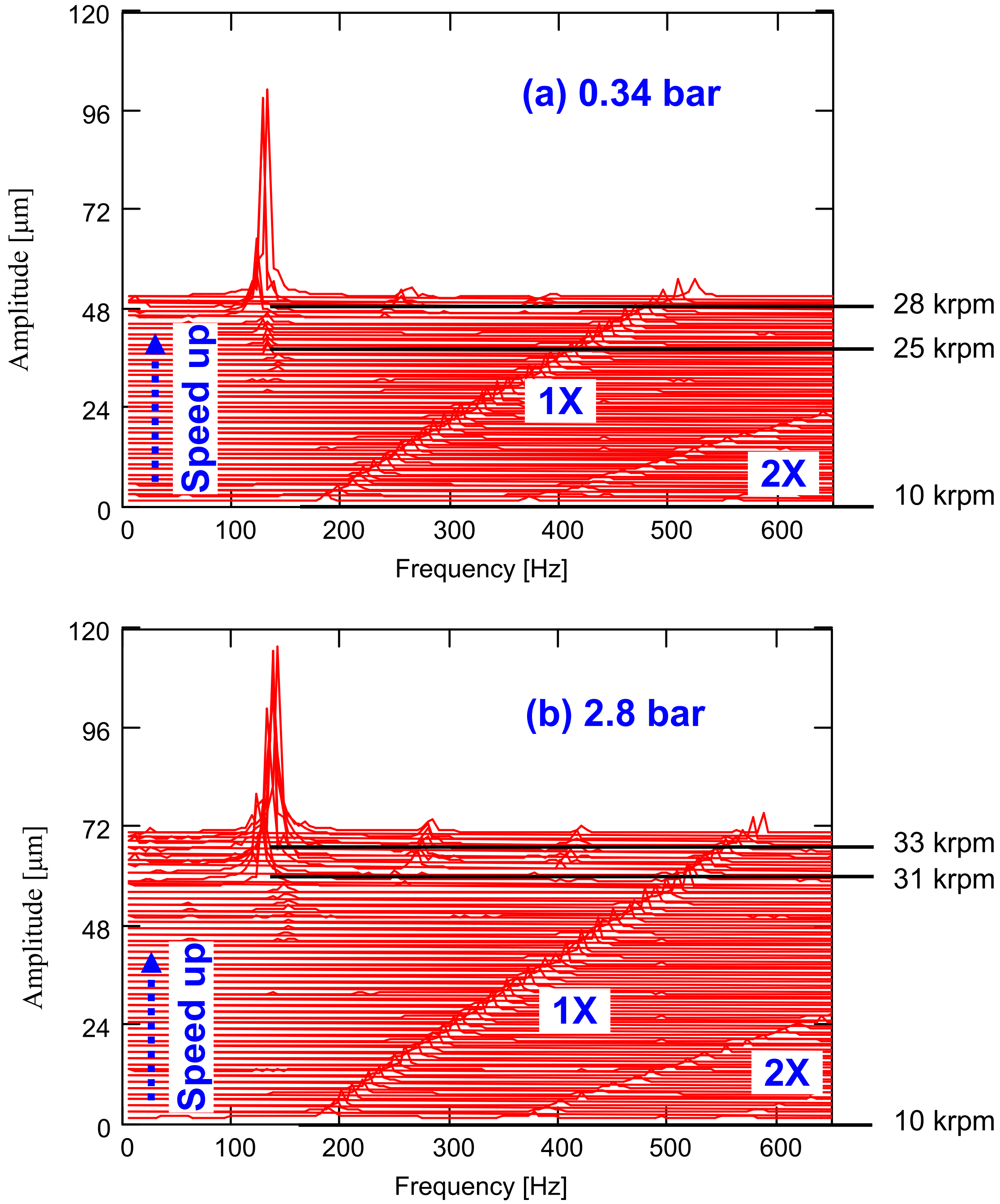

Figure 17 Waterfall of rotor speed-up response from 10 krpm. Baseline imbalance condition, feed air gauge pressures (a) 0.34 bar (5 psig) and (b) 2.8 bar (40 psig). Vertical displacements recorded at rotor free end. Original GFBs.

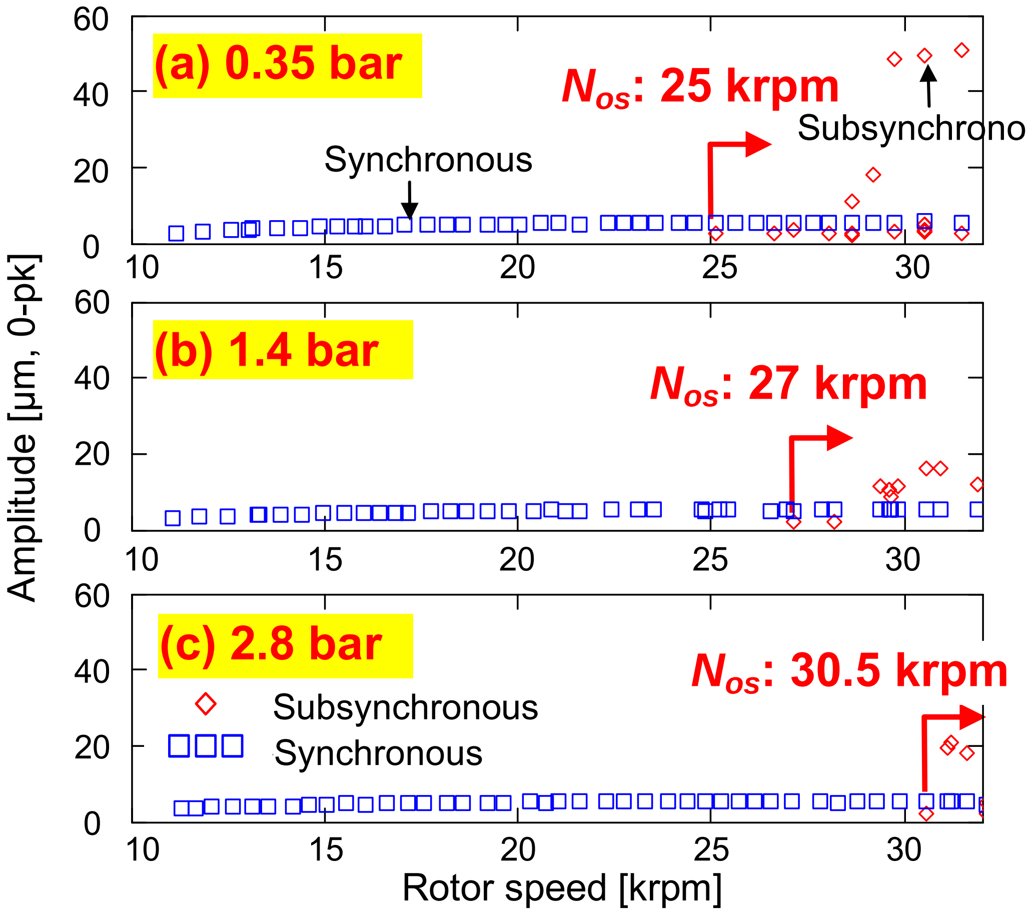

Figure 18 Amplitudes of synchronous and subsynchronous rotor motions for increasing side end feed gauge pressures versus shaft speed. Vertical displacements (*X*-direction) at rotor free end. Rotor half mass: 0.5 kg. N_{os}: onset speed of subsynchronous motions. Original GFBs.

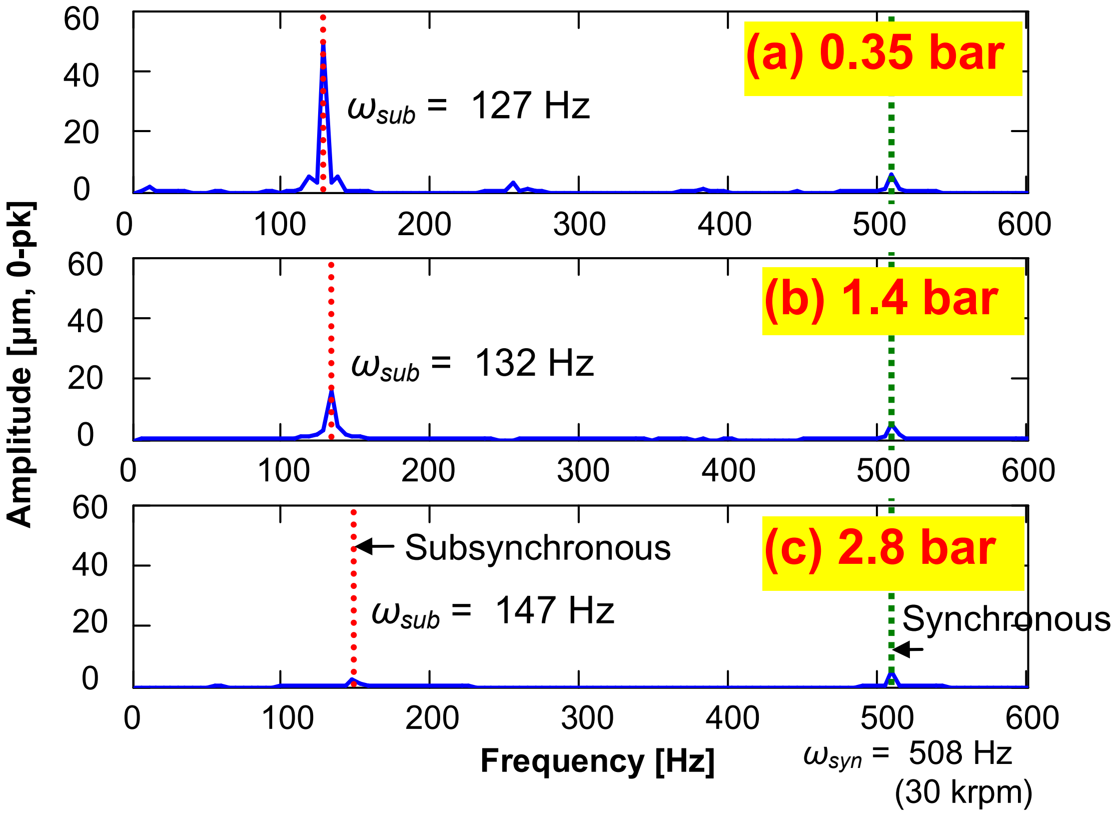

Figure 19 Spectra of rotor motions for increasing side end feed (gauge) pressures and operation at 30 krpm (500 Hz). Original GFBs.

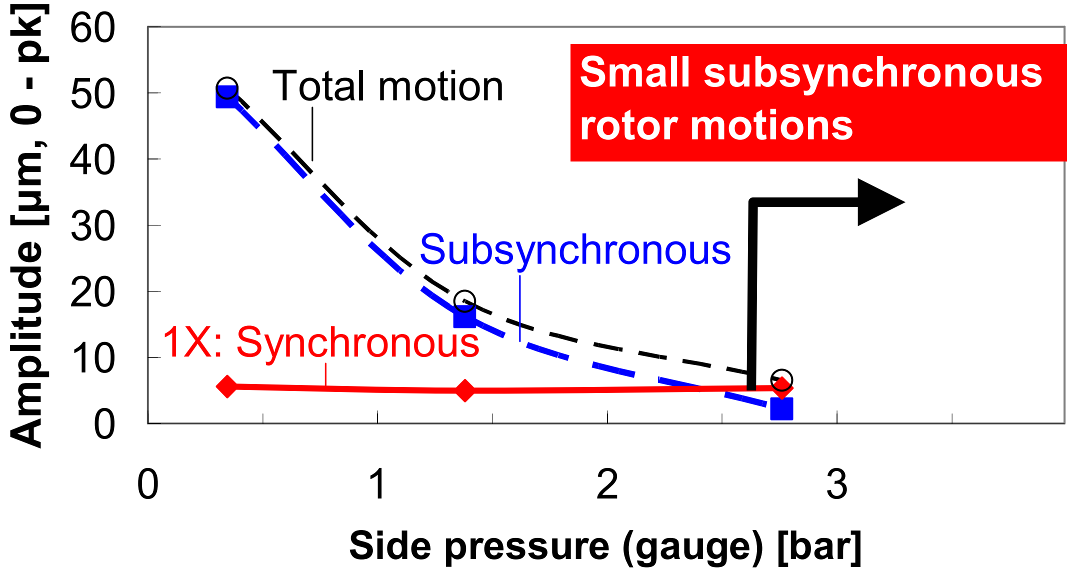

Figure 20 Amplitudes of total shaft motion, and synchronous and subsynchronous components versus side end gas pressurization at 30 krpm (500 Hz). Original GFBs.

Synchronous response amplitude and phase angle (rotor coastdown tests)

Imbalance response measurements are conducted during rotor coastdown test from 25 krpm at a side end (gauge) pressure of 0.35 bar (5 psig) for in-phase and out-of-phase large imbalance mass of 330 mg, i.e. six times the minimum imbalance mass of 55 mg (imbalance distances, *u*=1.3 μm and 2.3 μm, for the rotor drive and free ends). Figures 21a and 22b show the normalized rotor amplitudes and phase angles of the measured synchronous responses with the large imbalance mass, and compare them to those with small to moderate imbalance masses reported in [78]. The recorded imbalance responses are subtracted using a baseline response (amplitude and phase) and normalized by multiplying the ratio of the smallest imbalance to the actual imbalance [78]. The figures display the vertical motions at the rotor drive end. Each phase angle is shifted an offset to discard the influence of an imbalance mass angular disposition on the recorded data (e.g., a shifted offset of -45 º at the drive end, vertical plane for both in-phase and out-of-phase imbalance conditions).

For the smallest to moderate imbalance masses, the test data evidence nearly uniform normalized amplitudes and phase angles, i.e., characteristic of a linear system. On the other hand, with a large imbalance mass of 330 mg, the peak amplitude around the critical speed (ω_{cr}) increases significantly, in particular, for the out-of-phase imbalance test. The critical speed of the rotor-bearing system decreases by ~3 krpm when compared to those estimated with the smallest to moderate imbalance masses. The phase angle of ~ 90 º determines similar natural frequency for all imbalance conditions. With the large imbalance mass, the phase angle increases more rapidly around the natural frequency, showing a reduction in equivalent viscous damping. Thus, a large imbalance mass causes a nonlinear response of the rotor – GFB system as discussed in [17]. Note, however, that the added imbalance mass appears not to change the system natural frequency, i.e. the system effective stiffness appears indifferent to the magnitude of added imbalance mass.

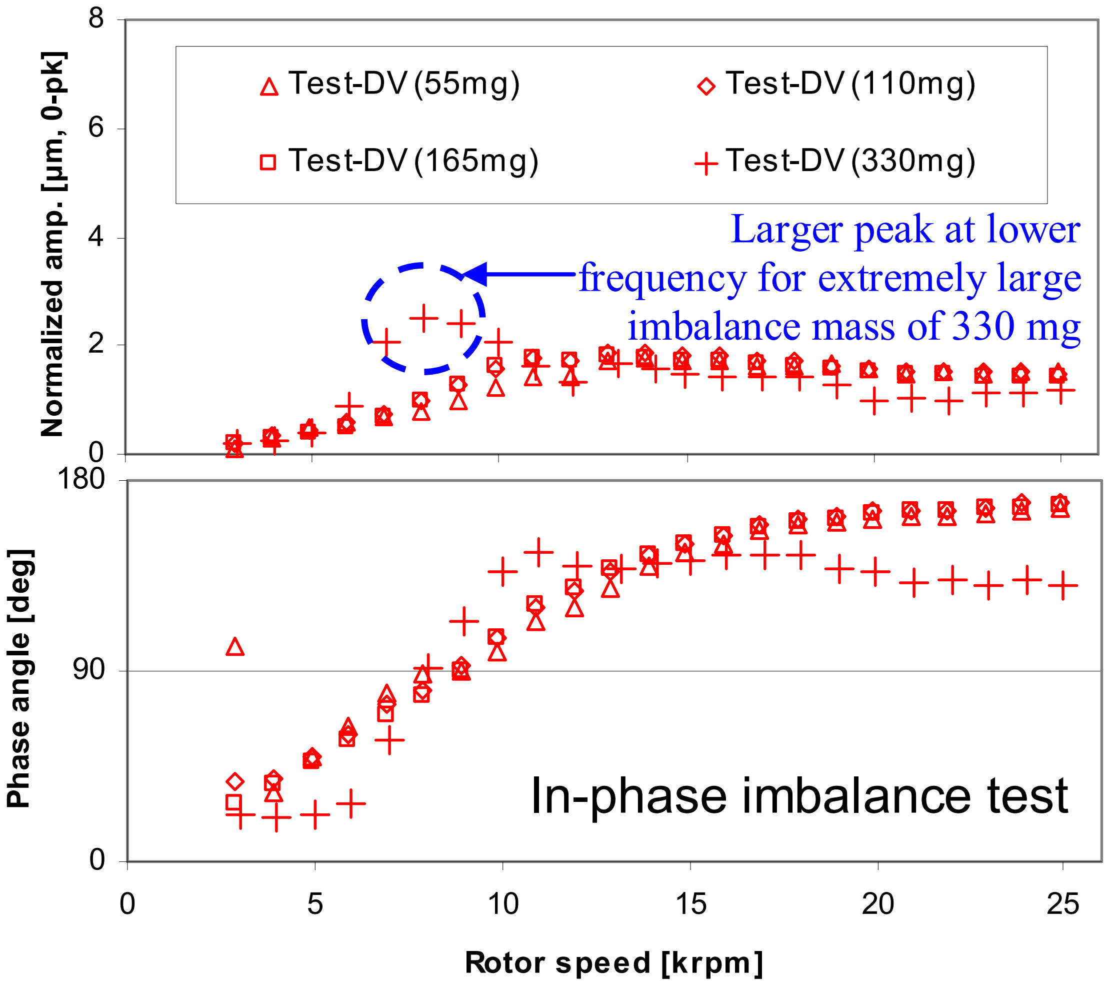

Figure 21a Influence of large imbalance mass on normalized amplitude and phase angle of synchronous response. In-phase imbalance masses of 55mg, 110mg, 165mg, and 330mg. Measurement at drive end bearing, vertical plane with baseline subtraction. Side end gauge pressure at 0.34 bar (5 psig). Original GFBs.

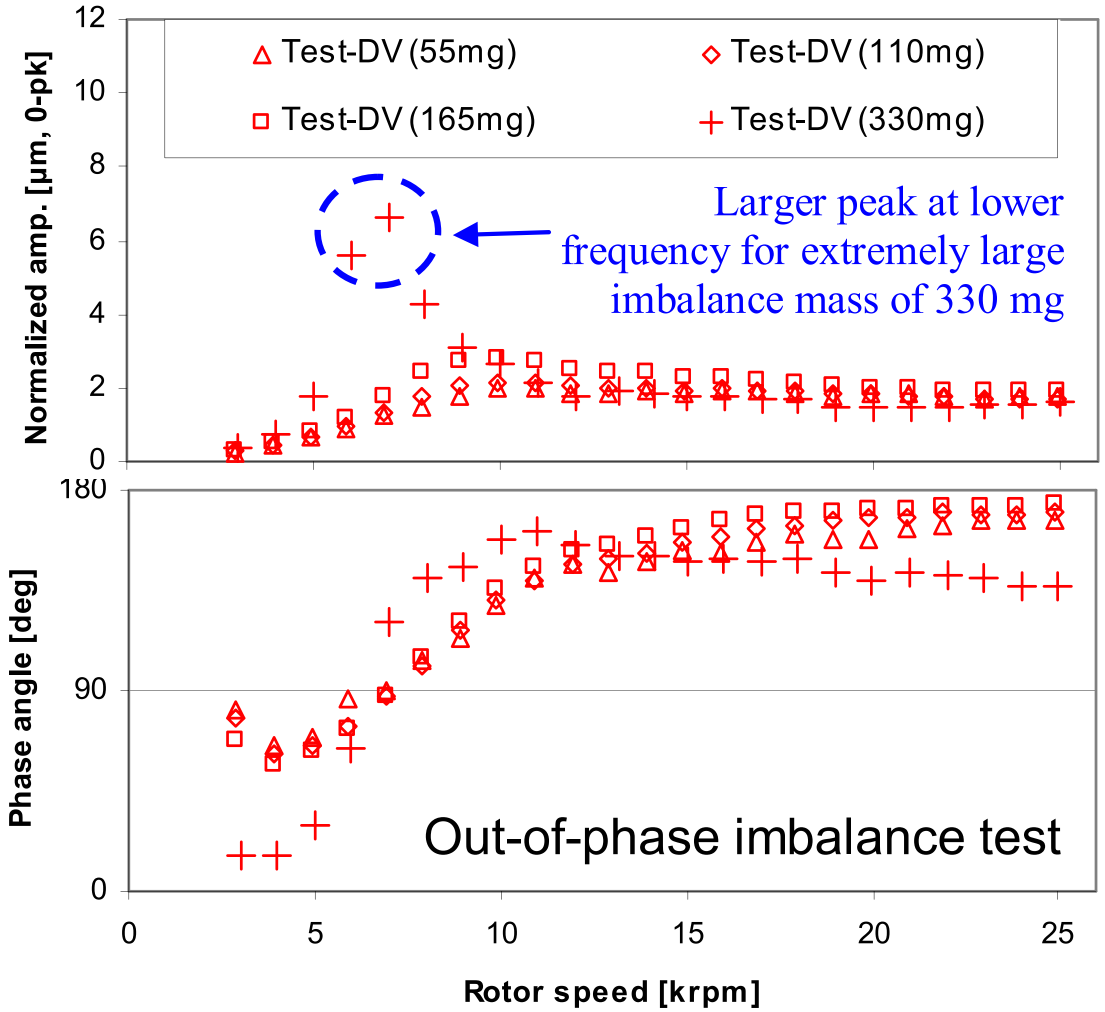

Figure 21b Influence of large imbalance mass on normalized amplitude and phase angle of synchronous response. Out-of-phase imbalance test responses with imbalance masses of 55mg, 110mg, 165mg, and 330mg. Measurement at drive end bearing, vertical plane with baseline subtraction. Side end gauge pressure at 0.34 bar (5 psig). Original GFBs.

Note that, in Figs. 21a and 21b, a large imbalance mass of 330 mg results in different trends of phase angles from those with small to moderate imbalance masses; the phase angle is not toward 180 º as the rotor speed increases. This may be caused due to a lack of viscous damping with the large imbalance mass; for example, in a dry-friction damping model, the phase angle is independent of the frequency of a response[6] [80].

Appendix B shows the normalized amplitude and phase angle of the rotor synchronous response for the free end bearing, vertical plane. Next section details the determination of the effective stiffness (K_{eff}), damping ratio (ξ), and effective damping (C_{eff}) derived from the rotor responses to moderate and large imbalance masses.

Figures 22a and 22b show coastdown rotor responses for large and small imbalance masses of 330 mg and 55 mg, respectively. Note that the large imbalance mass of 330 mg causes subsynchronous rotor motions of large amplitude at rotor speeds as low as 18krpm. For the large added imbalance (330 mg), the rotor shows whirl frequency ratios (*WFR*=subsynchronous whirl frequency / rotor speed) equal to 0.33 (1/3 *X*) and 0.66 (2/3*X*) from 28 krpm to 18 krpm; while for the small imbalance mass (55 mg) the rotor shows *WFR*s equal to 0.25 (1/4*X*) and 0.5 (1/2*X*) from 35 krpm to 27 krpm. Note, however, that for the small imbalance mass (55 mg), the recorded relatively small amplitudes of subsynchronous rotor motions appearing between 23 krpm and 30 krpm show a *WFR* equal to 0.33 (1/3*X*).

---

[6] Ginsberg [80] also notices that a large amplitude dynamic force (F), a small dry-friction coefficient (μ), and a small normal load (N) lead to null energy dissipation (a typical result from the dry-friction effect for operation of the system) at the natural frequency, thus causing significantly large amplitude peaks at this frequency, i.e. $E_{diss}=0$ if $\mu N/F<\pi/4$. Therefore, it is readily inferred that a small imbalance mass, a heavy rotor mass, and a large dry-friction coefficient aid to reduce rotor amplitude peak at the natural frequency of the rotor-GFB system.

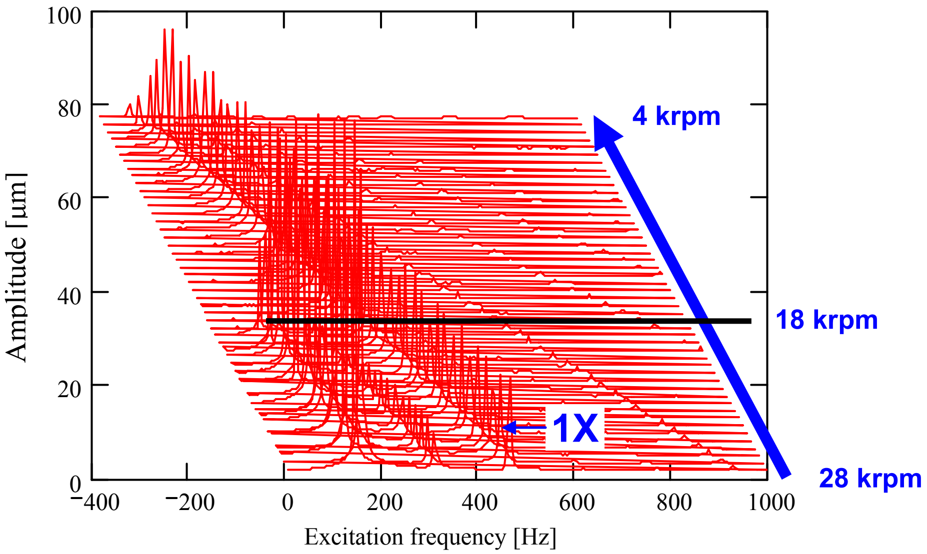

(a) Waterfall

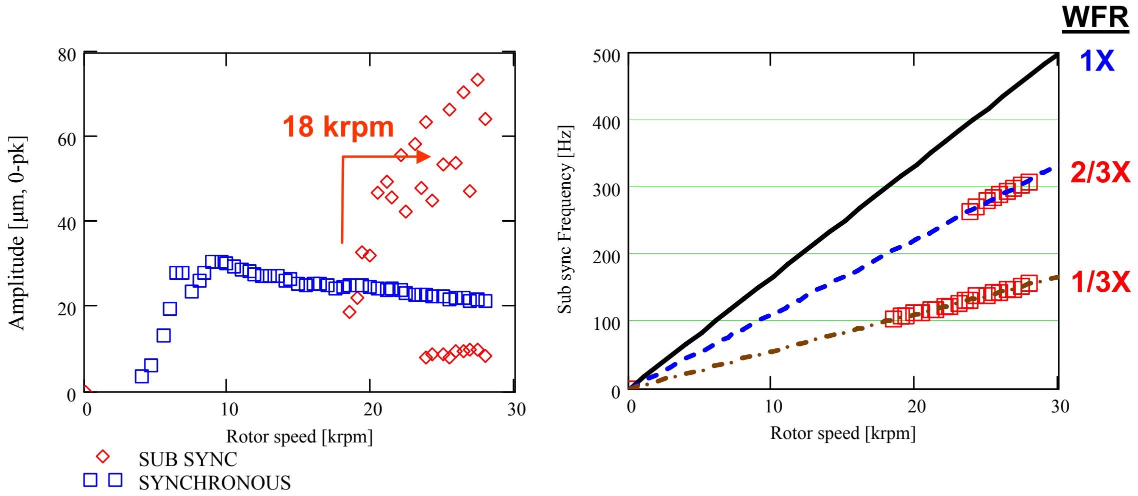

(b) Synchronous and subsynchronous components

(c) Subsynchronous whirl frequency

Figure 22a Coastdown rotor response from 28 krpm. Out-of-phase imbalance mass of 330 mg, side end air gauge pressure of 0.34 bar (5 psig). Measurement at rotor free end, vertical plane. Original GFBs.

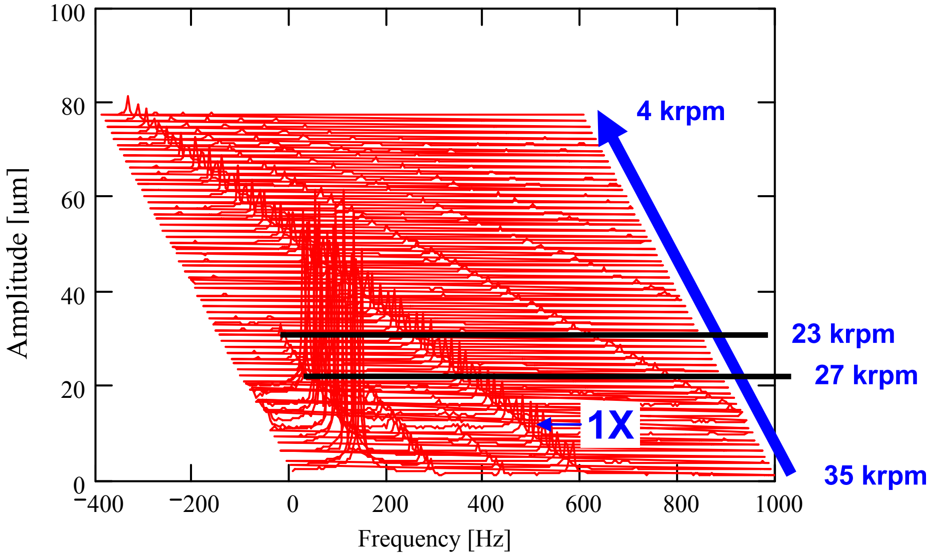

(a) Waterfall

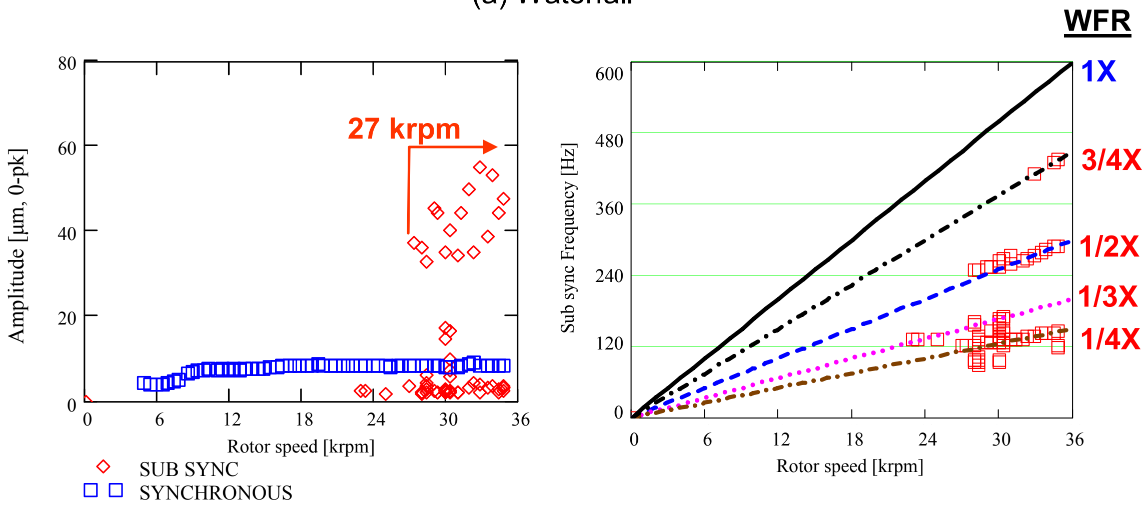

(b) Synchronous and subsynchronous components

(c) Subsynchronous whirl frequency

Figure 22b Coastdown rotor response from 35 krpm. Out-of-phase imbalance mass of 55 mg, side end air gauge pressure of 0.34 bar (5 psig). Measurement at rotor free end, vertical plane. Original GFBs.

Further imbalance response measurements are conducted on GFBs with side end pressurization for small to moderate imbalance masses of 55 mg, 110 mg, and 165 mg. At increasing side end pressures of 1.4 bar (20 psig) and 2.8 bar (40 psig), test results present nearly uniform normalized amplitudes and phase angles, i.e., characteristic of a linear system and similar to those for 0.34 bar (5 psig) feed pressure as shown in Fig. 23 (See also Appendix C).

The normalized rotor amplitudes and phase angles for the increasing imbalance masses at each side end pressure are arithmetically averaged, for a comparison to the averaged results at 0.34 bar (5 psig). Figures 23a and 23b present the averaged normalized amplitudes and phase angles at increasing side end pressures of 0.34 bar (5 psig), 1.4 bar (20 psig) and 2.8 bar (40 psig). The peak amplitude around the critical speed (ω_{cr}) increases for operation with side end pressures of 1.4 bar (20 psig) and 2.8 bar (40 psig), thus implying a decrease in system damping ratio. Side end pressurization does not change the system natural frequency, although the critical speed decreases slightly. Note that Ref. [17] shows somewhat opposite results, i.e. a reduction in the amplitudes of synchronous motion while crossing a critical speed. The discrepancy may be due to poor baseline imbalance subtraction in Ref. [17].

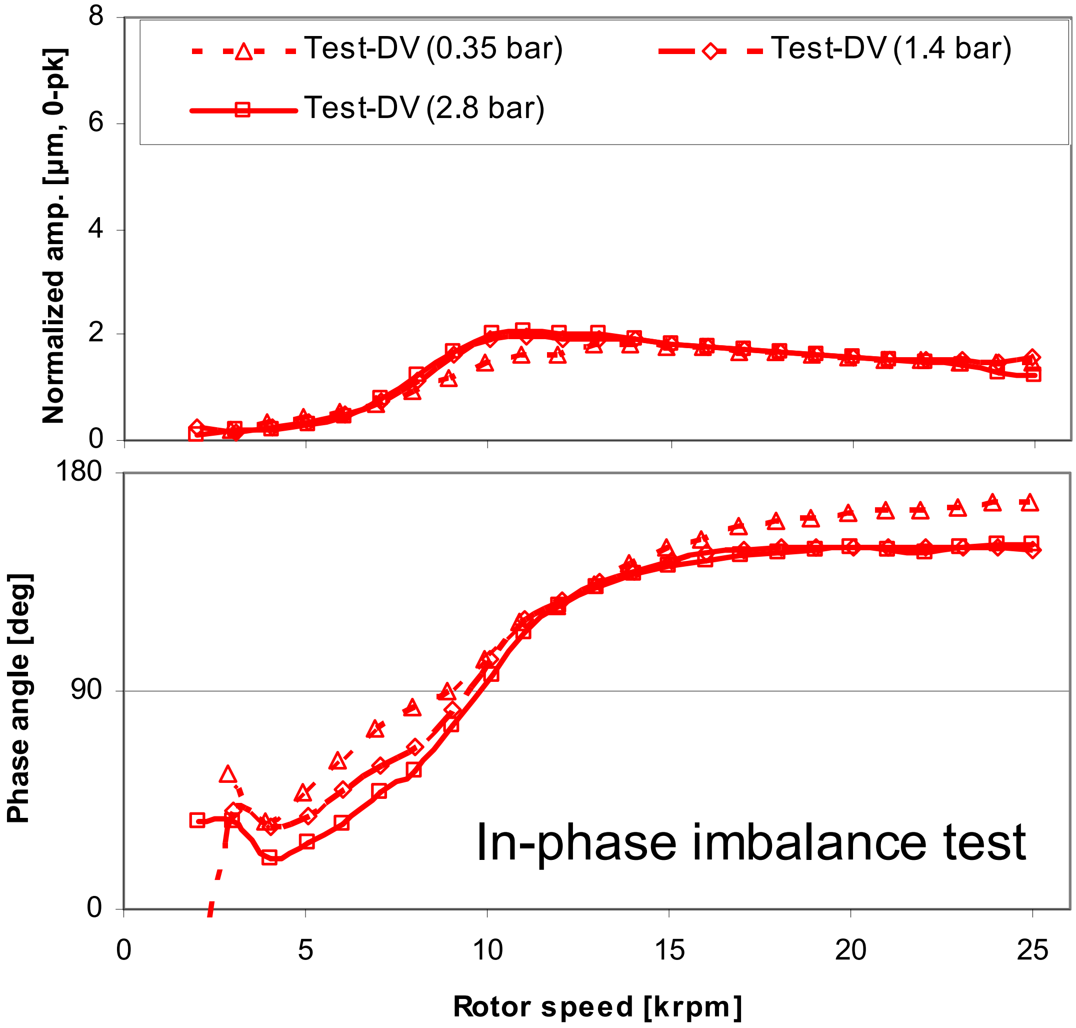

Figure 23a Normalized rotor amplitude and phase angle of synchronous response (averaged over the increasing in-phase imbalance masses of 55 mg, 110 mg, and 165 mg) at increasing side end gauge pressures of 0.34 bar (5 psig), 1.4 bar (20 psig), and 2.8 bar (40 psig). Measurement at drive end bearing, vertical plane with baseline subtraction. Original GFBs.

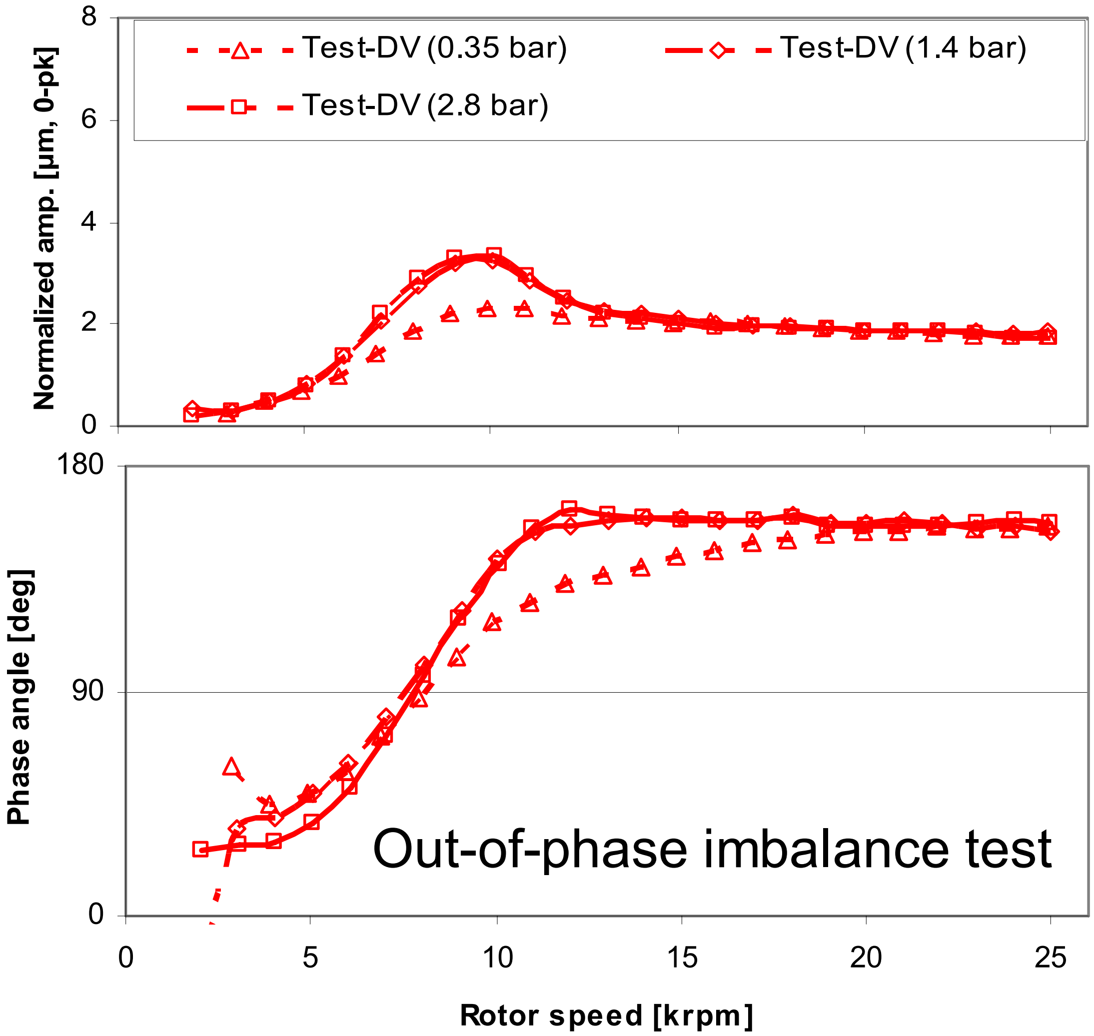

Figure 23b Normalized rotor amplitude and phase angle of synchronous response (averaged over the increasing out-of-phase imbalance masses of 55 mg, 110 mg, and 165 mg) at increasing side end gauge pressures of 0.34 bar (5 psig), 1.4 bar (20 psig), and 2.8 bar (40 psig). Measurement at drive end bearing, vertical plane with baseline subtraction. Original GFBs.

Rotordynamic parameters of rotor and GFBs

Rotordynamic parameters of the rotor-GFB system are identified using a one degree of freedom model and the measured rotor responses with small to large imbalance masses at the side end gauge pressure of 0.34 bar (5 psig). Phase angles equal to 90 º identify the undamped natural frequencies, ω_n, for in-phase and out-of-phase imbalance conditions. The effective stiffness coefficient, K_{eff} is estimated as $K_{eff} = \omega_n^2 M$ at the drive and free end bearing locations. Note that M is a fraction of the rotor mass that each bearing supports. The damping ratio (ξ) and the damping coefficient (C_{eff}) are estimated as [80];

$$\xi = \sqrt{\frac{1}{2}\left\{1-\left(\frac{\omega_n}{\omega_{cr}}\right)^2\right\}}; \qquad C_{eff} = 2\xi\sqrt{K_{eff}M} \tag{6}$$

Note that, in the first equation above, the damping ratio (ξ) approaches zero as the critical speed, ω_{cr} moves toward the natural frequency, ω_n. Hence, Table 4 lists the dynamic parameters of the rotor-GFB system identified, using the synchronous response. Note that small to moderate imbalance masses of 55 mg, 110 mg, and 165 mg result in nearly uniform normalized amplitude and phase angle of synchronous response, thus implying no discernable difference in dynamic parameters of the rotor-GFB system. For the small to moderate imbalance masses, the damping ratios are ~ 0.5 for the in-phase and out-of-phase imbalance conditions, thus implying a well-damped system. On the other hand, with the large imbalance mass of 330 mg, the damping ratio is smaller than 0.3 for most estimations. Fro the same imbalance mass, the effective stiffness coefficients increase slightly for the free end GFB, albeit decreasing slightly for the drive end GFB, thus showing insignificant changes. Note that, in this simple analysis, K_{eff} and C_{eff} may not accurately represent the bearing stiffness and damping coefficients due to the influence of the coupling stiffness.

Table 4 Estimated rotordynamic parameters of the rotor-GFB system obtained from synchronous coastdown responses. Side end air gauge pressure at 0.34 bar (5 psig). Original GFBs.

Location		Imbalance Condition	Natural frequency, $\omega_n \times (30/\pi)$ [rpm]	Critical Speed, $\omega_{cr} \times (30/\pi)$ [rpm]	Effective stiffness, K_{eff} [MN/m]	Damping ratio, ξ	Effective damping, C_{eff} [N-s/m]
Imbalance mass (55 mg), u_{DE} = 1.26 μm and u_{FE} = 2.34 μm							
Drive end	X_{DE}	in phase	9,000	13,000	0.59	0.51	635
		out of phase	7,000	11,000	0.35	0.55	528
	Y_{DE}	in phase	10,000	18,000	0.72	0.59	813
		out of phase	8,000	11,000	0.46	0.49	537
Free End	X_{FE}	in phase	9,000	15,000	0.32	0.57	384
		out of phase	6,000	10,000	0.14	0.57	256
	Y_{FE}	in phase	10,500	16,000	0.44	0.53	422
		out of phase	9,000	15,000	0.32	0.57	384
Imbalance mass (110 mg), u_{DE} = 2.52 μm and u_{FE} = 4.67 μm							
Drive end	X_{DE}	in phase	9,000	13,000	0.59	0.51	635
		out of phase	7,000	11,000	0.35	0.55	528
	Y_{DE}	in phase	8,500	18,000	0.52	0.62	732
		out of phase	8,000	11,000	0.46	0.49	537
Free End	X_{FE}	in phase	8,000	16,000	0.25	0.61	369
		out of phase	7,000	10,000	0.19	0.51	267
	Y_{FE}	in phase	8,000	16,000	0.25	0.61	369
		out of phase	8,500	12,000	0.29	0.50	320
Imbalance mass (165 mg), u_{DE} = 3.78 μm and u_{FE} = 7.00 μm							
Drive end	X_{DE}	in phase	9,000	13,000	0.59	0.51	635
		out of phase	7,000	10,000	0.35	0.51	489
	Y_{DE}	in phase	8,500	18,000	0.52	0.62	732
		out of phase	6,500	10,000	0.31	0.54	483

Table 4 continued

Location		Imbalance Condition	Natural frequency, $\omega_n \times (30/\pi)$ [rpm]	Critical Speed, $\omega_{cr} \times (30/\pi)$ [rpm]	Effective stiffness, K_{eff} [MN/m]	Damping ratio, ξ	Effective damping, C_{eff} [N-s/m]
Imbalance mass (165 mg), u_{DE} = 3.78 µm and u_{FE} = 7.00 µm							
Free End	X_{FE}	in phase	8,000	18,000	0.25	0.63	382
		out of phase	7,000	9,000	0.19	0.44	235
	Y_{FE}	in phase	7,000	16,000	0.19	0.64	336
		out of phase	8,000	12,000	0.25	0.53	318
Imbalance mass (330 mg), u_{DE} = 7.56 µm and u_{FE} = 14.0 µm							
Drive end	X_{DE}	in phase	7,900	8,000	0.45	0.11	122
		out of phase	6,500	7,000	0.31	0.26	236
	Y_{DE}	in phase	7,500	10,000	0.41	0.47	485
		out of phase	5,500	6,000	0.22	0.28	215
Free End	X_{FE}	in phase	8,500	9,000	0.29	0.23	149
		out of phase	7,500	9,000	0.22	0.39	221
	Y_{FE}	in phase	7,500	8,000	0.22	0.25	139
		out of phase	6,000	6,100	0.14	0.13	58

X: vertical, Y: horizontal. ω_n and ω_{cr} are determined from synchronous rotor responses with uncertainty of ±500 rpm.

Rotor masses supported on the drive end and free end bearings are 0.66 kg and 0.36 kg, respectively.

Effect of Mechanical Preloads (Shims) on Dynamic Performance of GFB

Reference [78] shows that the test rotor supported on the original GFBs could have operated to 50 krpm (motor maximum speed) for extended periods of time. The rotor showed significant subsynchronous motions from 27 krpm to 50 krpm for operation with a side end air pressure at 0.34 bar (5 psig), see Fig. 24. As the rotor speed decreased from 50 krpm, the amplitudes of subsynchronous motions became smaller. In spite of the large rotor motions recorded for speeds larger than 27 krpm, the test GFBs survived without damage, except for some coating wear.

Three metal shims of 25 μm thickness are installed into the test GFB to enhance the bearing stiffness (See Table 3), thus increasing the system critical speed. An increase in the critical speed is expected to increase the threshold speed of instability if the whirl frequency ratio (WFR) is unchanged. Coastdown tests from 50 krpm are conducted at a side end pressure of 0.34 bar (5psig). Figure 25 displays the waterfall plot, synchronous and subsynchronous amplitudes, and subsynchronous whirl frequency of the vertical rotor motion recorded at the rotor free end for an out-of-phase imbalance mass of 110 mg. The amplitude of synchronous motion is smaller than 11 μm over the whole speed range. Significant subsynchronous motion appears from 50 krpm to ~ 40 krpm. The amplitude of the subsynchronous motion decreases with mechanical preload when compared to those without the mechanical preload. Below 40 krpm, the amplitude of the subsynchronous motions is smaller than 7 μm. Thus, introducing a preload in the GFBs delays by ~13 krpm the onset of subsynchronous motions with persistent increasing amplitudes of rotor motion. As rotor speed decreases from 50 krpm to 26 krpm, the subsynchronous whirl frequency decreases from 151 Hz to 137 Hz.

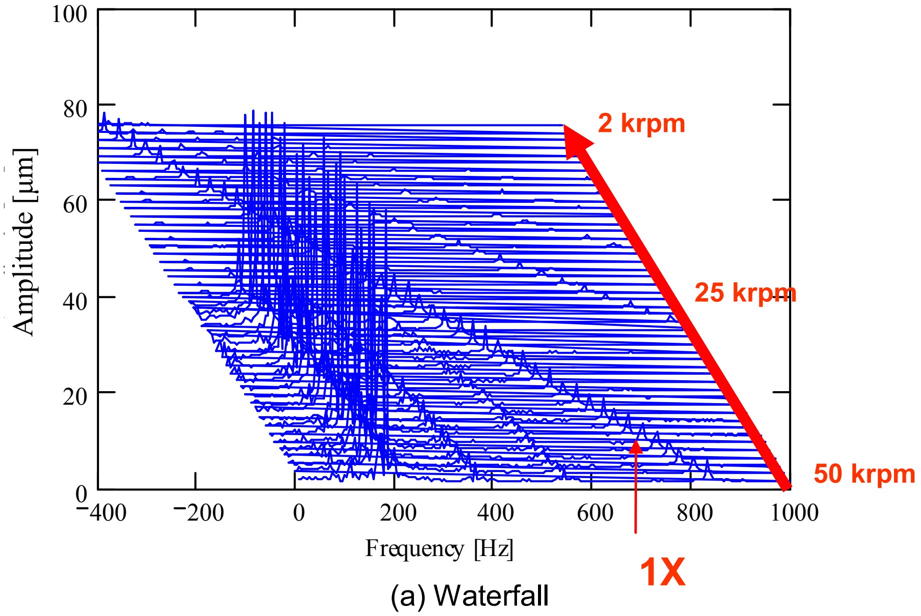

(a) Waterfall

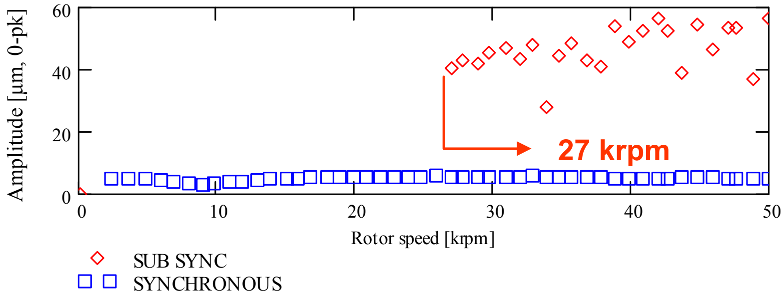

(b) Synchronous and subsynchronous components

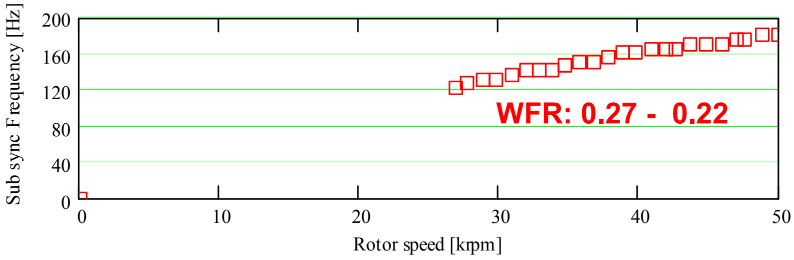

(c) Subsynchronous whirl frequency

Figure 24 Coastdown rotor response from 50 krpm. Baseline imbalance condition, side end air gauge pressure of 0.34 bar (5 psig). Measurement at rotor free end, vertical plane. Original GFBs [16].

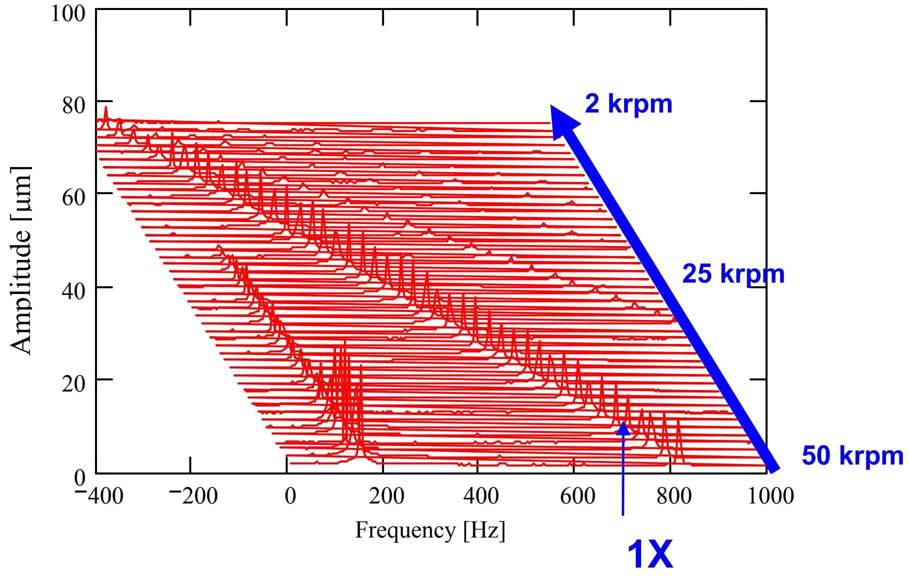

(a) Waterfall

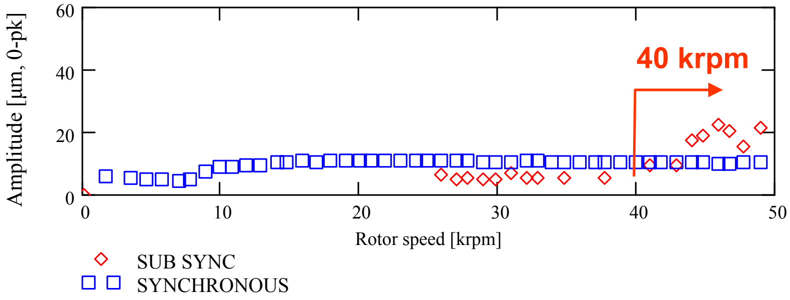

(b) Synchronous and subsynchronous components

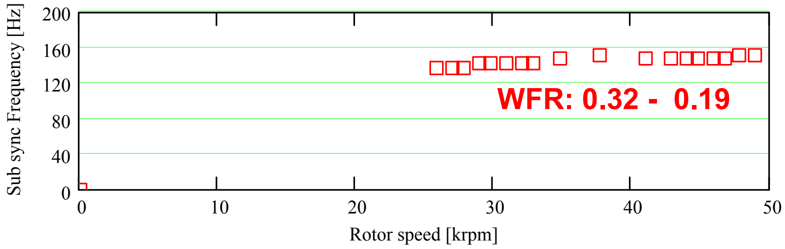

(c) Subsynchronous whirl frequency

Figure 25 Coast down rotor response from 50 krpm. Out of phase imbalance mass of 110 mg, side end air gauge pressure of 0.34 bar (5 psig). Measurement at rotor free end, vertical plane. GFBs with shims.

Figure 26 displays the rotor coastdown responses from 50 krpm for GFBs supplied with an increased side end pressure of 4.1 bar (60 psig), i.e., waterfall plot, synchronous and subsynchronous amplitudes, and subsynchronous whirl frequency of vertical motions recorded at the rotor free end. The amplitude of synchronous motion is smaller than 11 μm, and the subsynchronous motion appearing from 50 krpm to 27 krpm is smaller than 5 μm over the whole speed range. The subsynchronous whirl frequency decreases from 166 Hz to 142 Hz as the rotor speed decreases from 50 krpm to 30 krpm.

Figure 27 presents the amplitude of subsynchronous motion and associated whirl frequency measured during rotor speed-up tests for increasing side end pressures. The rotor speed is manually controlled to accelerate the rotor from the minimum motor control speed (10 krpm) to the maximum motor speed (~50 krpm). The side end pressure increases from 0.34 bar (5 psig) to 4.1 bar (60 psig) with a step increment of ~ 1.4 bar (20 psig) for each speed-up test. The measurements are taken at the rotor free end, vertical plane for out-of-phase imbalance of 110 mg. External pressurization reduces dramatically the amplitude of subsynchronous rotor motions. The subsynchronous whirl frequency does not change with air side end pressurization, but increases from 142 Hz to 152 Hz as rotor speed increases.

Note that a moderate change in rotor imbalance condition does not have a discernable effect on the rotor response. See Appendix D for speed-up rotor responses from 10 krpm to 50 krpm for the baseline imbalance condition at side end gauge pressures of 0.34 bar (5 psig) and 4.1 bar (60 psig).

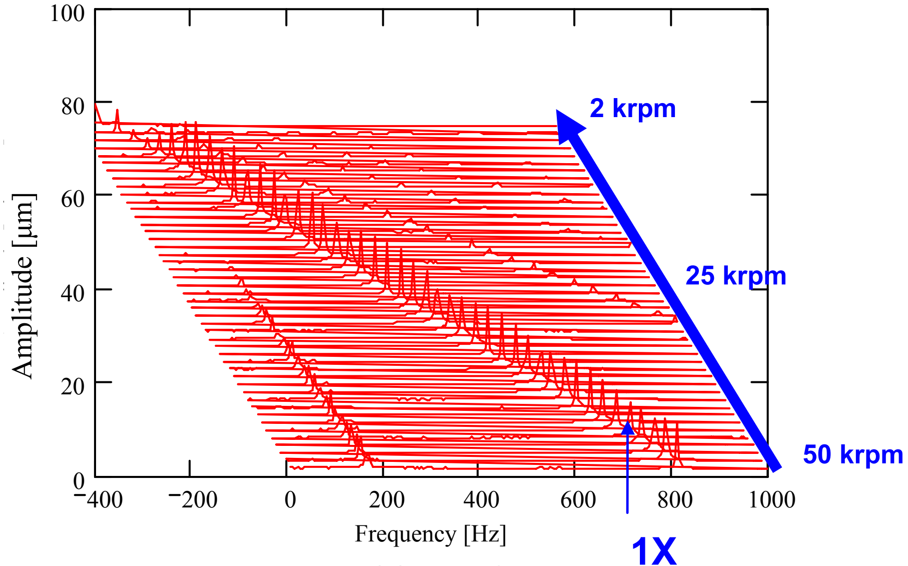

(a) Waterfall

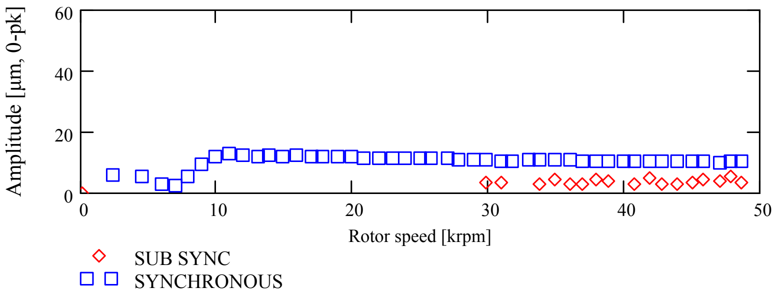

(b) Synchronous and subsynchronous components

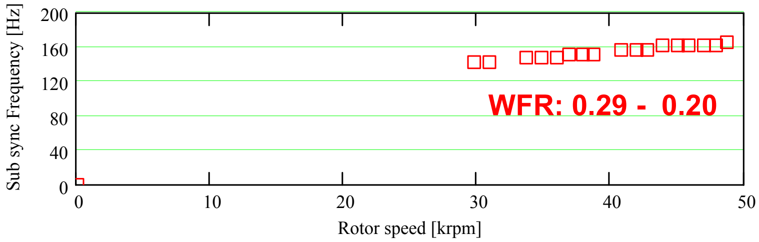

(c) Subsynchronous whirl frequency

Figure 26 Coast down rotor response from 50 krpm. Out of phase imbalance mass of 110 mg, side end air gauge pressure of 4.1 bar (60 psig). Measurement at rotor free end, vertical plane. GFBs with shims.

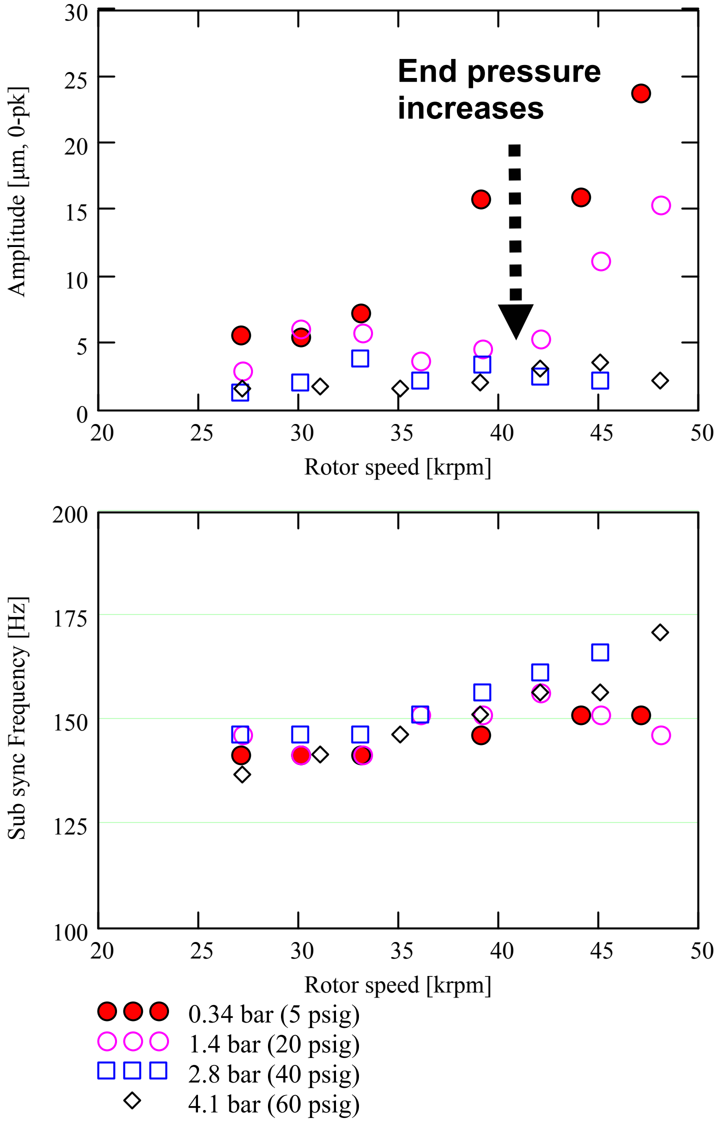

Figure 27 Amplitude of subsynchronous rotor motions, and subsynchronous whirl frequency during rotor speed-up test for increasing side end pressurization. Out-of-phase imbalance mass of 110 mg. Measurement at rotor free end, vertical plane. GFBs with shims.

Rotor speed coastdown tests from 35 krpm are conducted with a side end pressure of 0.34 bar (5psig) and the rotor at its baseline imbalance; and for in-phase and out-of-phase imbalance location conditions. Note that within this speed region (35 -0 krpm), subsynchronous rotor motions are insignificant. Figures 28a and 28b show normalized amplitudes of rotor synchronous response and phase angles for in-phase and out-of-phase imbalance masses equal to 55 mg and 110 mg.

The measurements at the rotor drive end, vertical plane are subtracted using the baseline synchronous response (amplitude and phase). The test data show nearly uniform normalized amplitudes, i.e., characteristics of a linear system as reported for GFBs. The natural frequency (ω_n) increases by ~ 5 krpm at the drive end bearing (vertical plane) for an in-phase imbalance mass of 55 mg; when compared to that for the GFB without shims. The increase in natural frequency (9 krpm → 14 krpm) implies an increase in bearing direct stiffness due to the mechanical preload.

Appendix E displays the normalized amplitude and phase angle of the rotor synchronous response for the free end bearing, vertical plane. Appendix F lists the dynamic parameters of the rotor-GFB system identified using the synchronous response for GFBs with shims. In general, installation of shims significantly increases the effective stiffness (K_{eff}) and decreases the damping ratio (ξ) and effective damping (C_{eff}). However, K_{eff} decreases notably for the imbalance mass of 110 mg when compared to that with the small imbalance mass of 55 mg. A reduction in K_{eff} is rather significant for the drive end GFB which has a smaller nominal radial clearance than the free end GFB[7]. Recall that K_{eff} is not sensitive to the smallest to moderate imbalance masses for the original configuration of GFBs without shims, as discussed for Table 4.

---

[7] See Appendix G for the estimated nominal radial clearances of the drive and free end GFBs, original configuration (without shims).

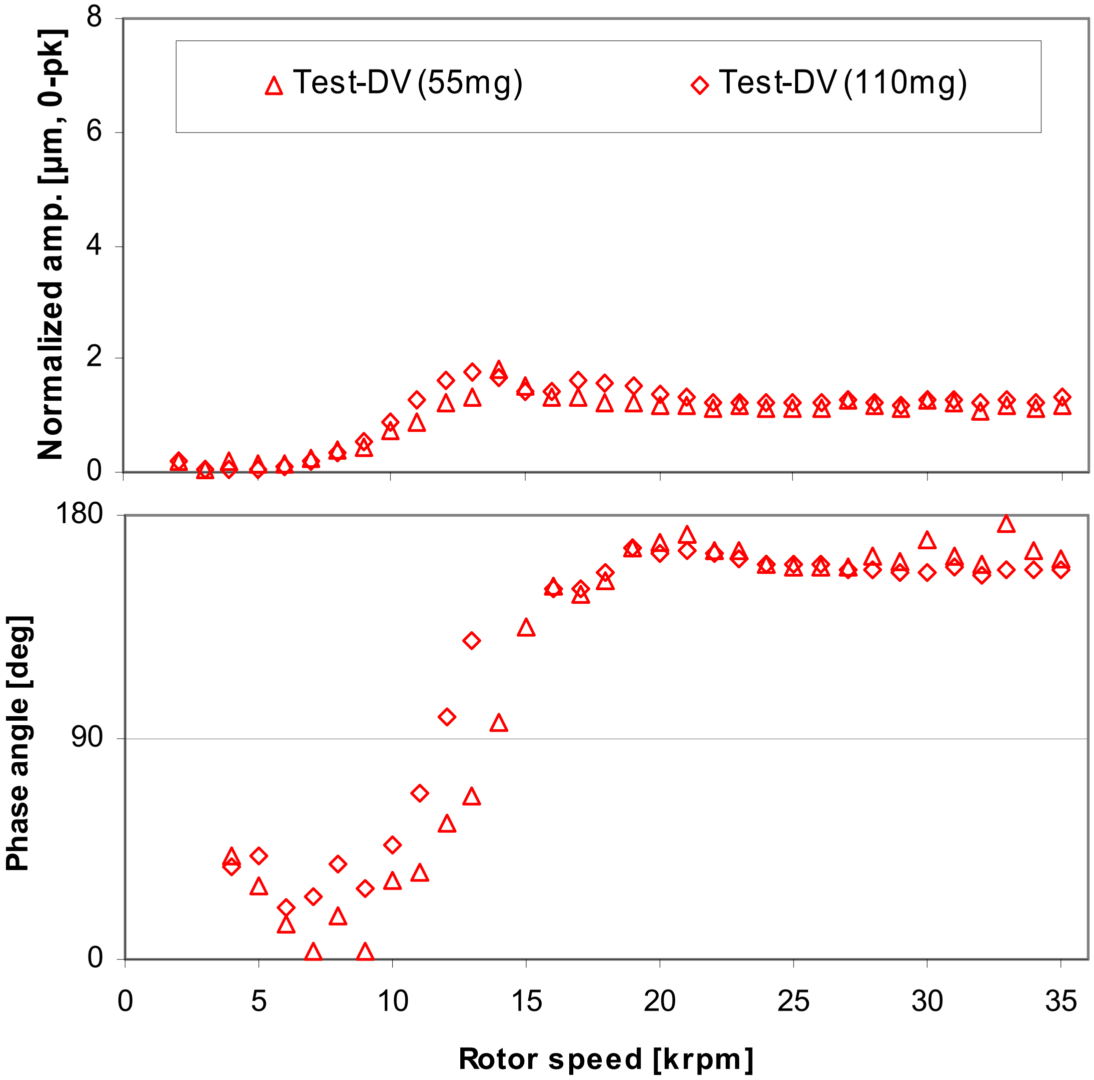

Figure 28a Normalized amplitude of synchronous response and phase angle for in-phase imbalance masses of 55mg and 110mg. Measurements at drive end bearing, vertical plane with baseline subtraction. Side end air gauge pressure at 0.34 bar (5 psig). GFBs with shims.

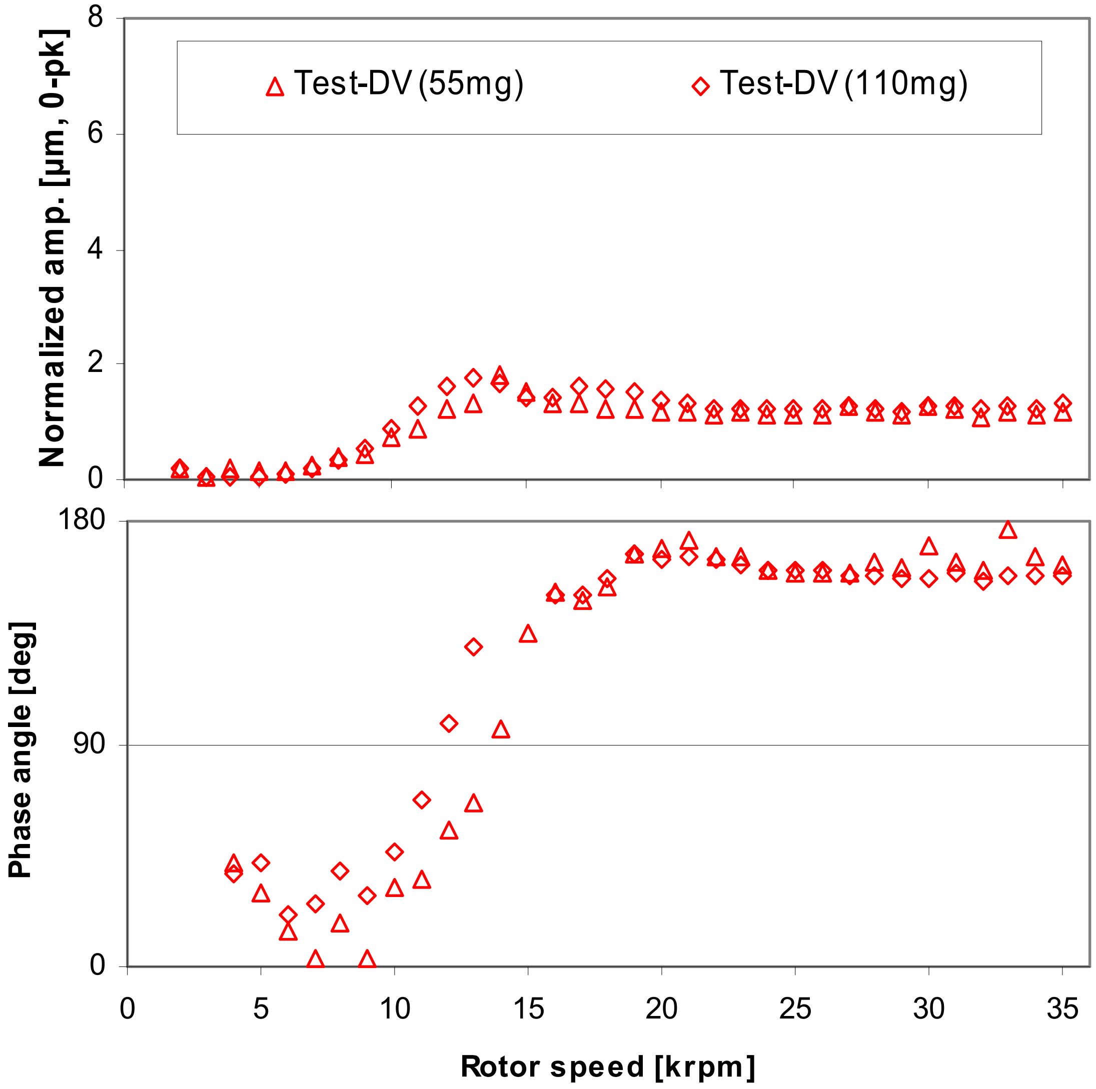

Figure 28b Normalized amplitude of synchronous response and phase angle for out-of-phase imbalance masses of 55mg and 110mg. Measurements at drive end bearing, vertical plane with baseline subtraction. Side end air gauge pressure at 0.34 bar (5 psig). GFBs with shims.

Figures 29a and 29b compare the amplitudes and phase angle of rotor synchronous motions at feed gauge pressures of 0.34 bar (5 psig) and 4.1 bar (60 psig) for the out-of-phase imbalance condition. The measurements recorded during coastdown tests show the subtraction of the baseline synchronous response (amplitude and phase). The speed coastdown test at 4.1 bar (60 psig) is conducted from 50 krpm; while the coastdown test at 0.34 bar (5 psig) is conducted from 38 krpm to reduce the influence of subsynchronous motions on the amplitude of the synchronous motion. A comparison of the synchronous amplitudes does not show significant changes for increasing side end pressures, i.e. critical speed and natural frequency are similar for the measurements at the drive and free end GFBs. However, for the measurement at the free end GFB, vertical plane, the amplitude increases from 3.5 μm to 5.8 μm, implying a reduction in damping. In general, side end pressurization may reduce damping while crossing a critical speed. This observation is valid for both the original and shimmed GFBs.

The static locus of the rotor centerline for increasing rotor speeds is estimated for the test GFBs. For GFBs with side end pressurization, the measurements may guide advancements in predictive models by providing an insight into the static performance of GFBs operating at increasing rotor speeds. Because a bearing geometric center, as well as the bearing clearance, is generally unknown, the initial rotor center position is set to zero. The DC bottom line refers to the locations where the rotor is in contact with the test bearings and without rotor spinning. Note that this bottom line may be relatively accurate for the free end bearing, while it may not be for the drive end bearing due to the flexible coupling connected to the rotor drive end. Appendix G provides the estimation of the flexible coupling stiffness.

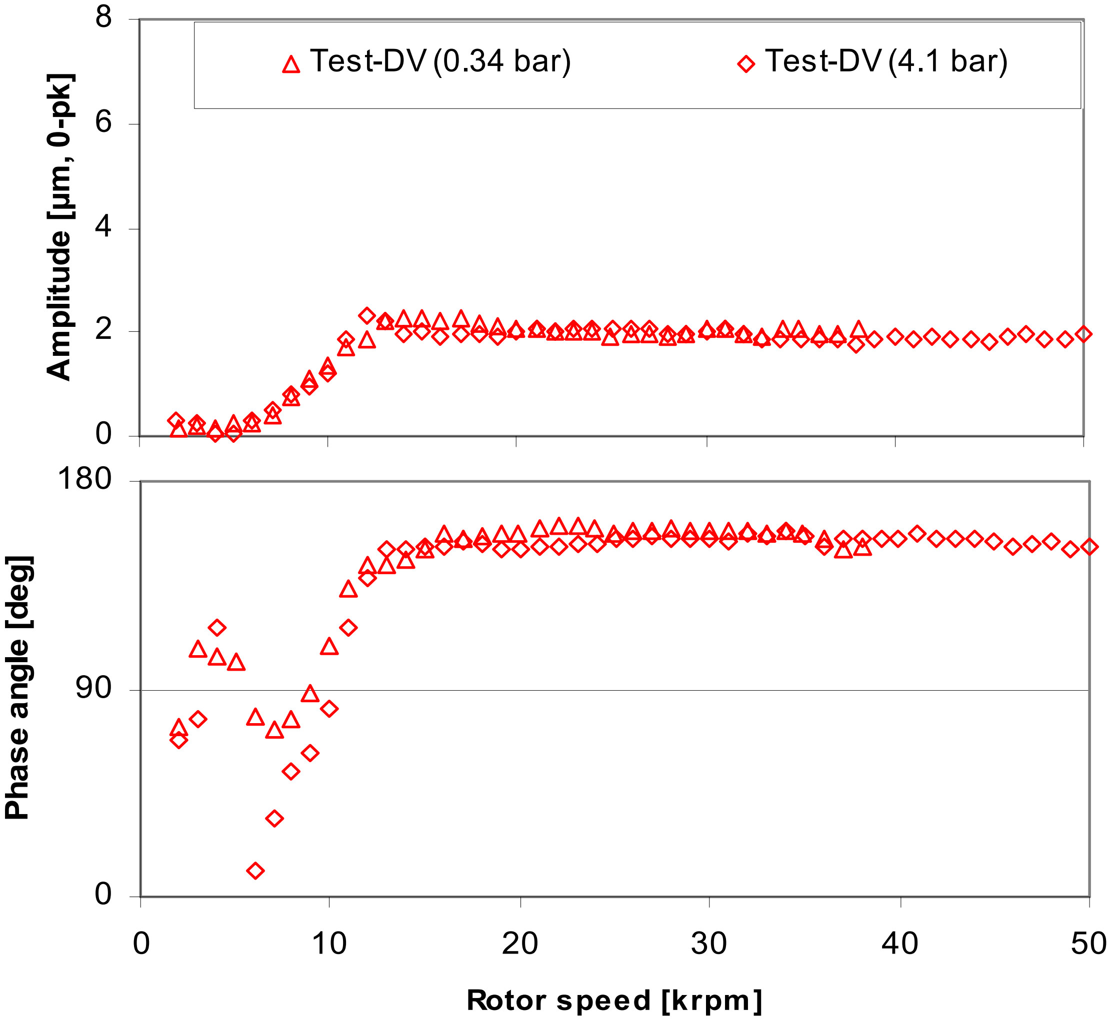

Figure 29a Amplitude and phase angle of synchronous rotor motion versus rotor speed for side end gauge pressures of 0.34 bar (5 psig) and 4.1 bar (60 psig). Measurements at drive end, vertical plane. Out-of-phase imbalance mass of 110 mg with baseline subtraction. GFBs with shims.

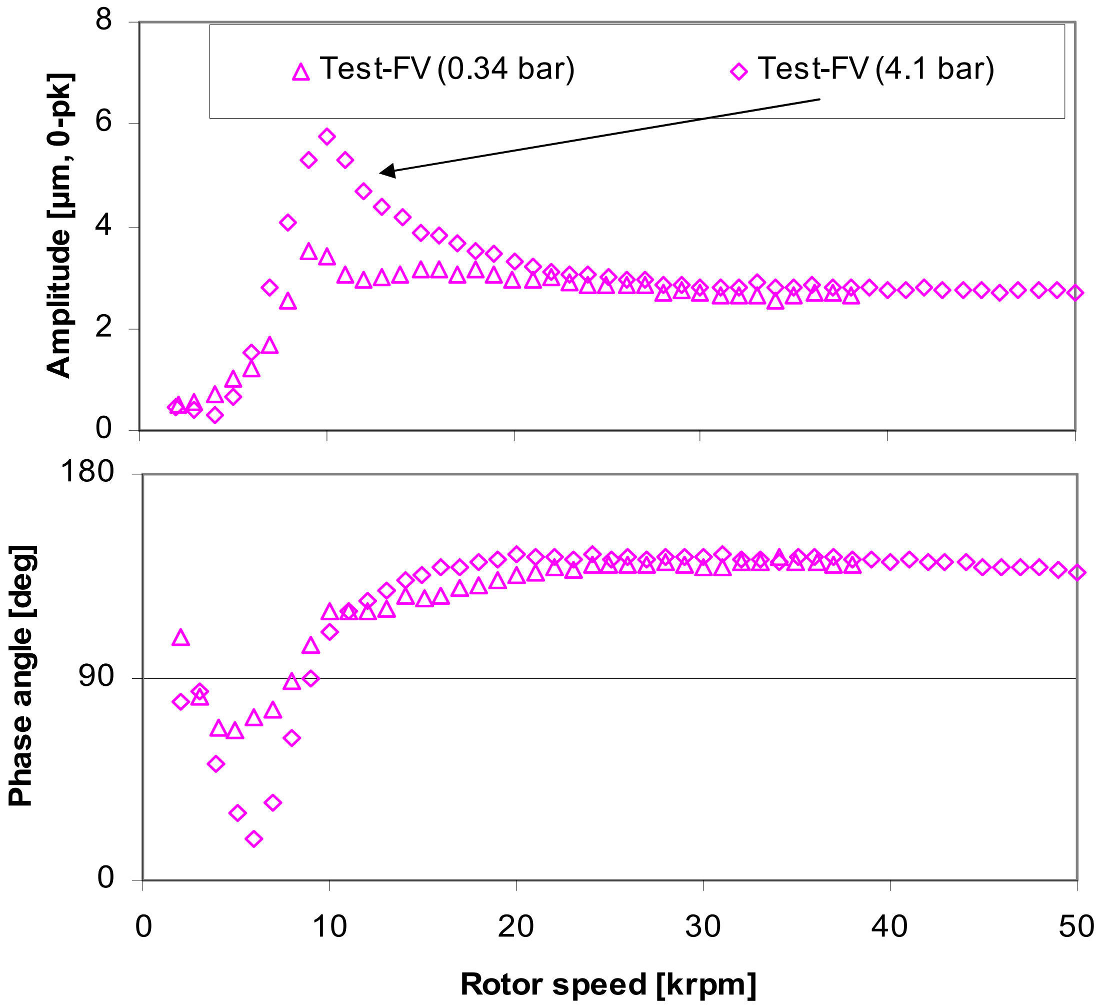

Figure 29b Amplitude and phase angle of synchronous rotor motion versus rotor speed for side end gauge pressures of 0.34 bar (5 psig) and 4.1 bar (60 psig). Measurements at free end, vertical plane. Out-of-phase imbalance mass of 110 mg with baseline subtraction. GFBs with shims.

Figure 30 displays the trajectory of the rotor static center during speed-up tests for an out of phase imbalance mass of 110 mg. Square and diamond symbols indicate measurements at the rotor drive and free ends, respectively. As the rotor speed increases from 11 krpm to 50 krpm, the static centerline measured at the rotor free end moves up and to the left, in a path with the same orientation as rotor spinning. At the rotor drive end, the orbit center moves up and to the right, in a path opposite to the orientation of rotor spinning. Hence, both the rotor static centers at the rotor drive and free ends moves up, in paths with different orientations as the rotor speed increases. As the side end pressure increases, the trajectory measured at the rotor free end tends to move up and the movement in the horizontal direction becomes narrower. The trajectory measured at the rotor drive end moves down slightly, and the movement in the horizontal direction becomes narrower. Note that the rotor has a small static displacement at the rotor drive end due to the coupling force. Relatively larger stiffness and smaller nominal clearance for the drive end GFB to those for the free end GFB (see Appendix G) also restrain the static displacement at the rotor drive end.

Figure 31 compares the static trajectories of the rotor center during rotor speed coastdown tests from 50 krpm for side end gauge pressures of 0.34 bar and 4.1 bar and an out of phase imbalance mass of 110 mg. As the rotor speed decreases, the static rotor center measured at the rotor free end moves down and to the right, in a path opposite to the orientation of rotor spinning. On the other hand, the rotor center measured at the rotor drive end moves down and to the left, in a path with the same orientation as rotor spinning. With increased pressure, the trajectory measured at the rotor free end moves up, and the movement in the horizontal direction becomes narrower. Thus, it is inferred that an increase in side end pressure may reduce the cross-coupled effects destabilizing the rotor at high speeds.

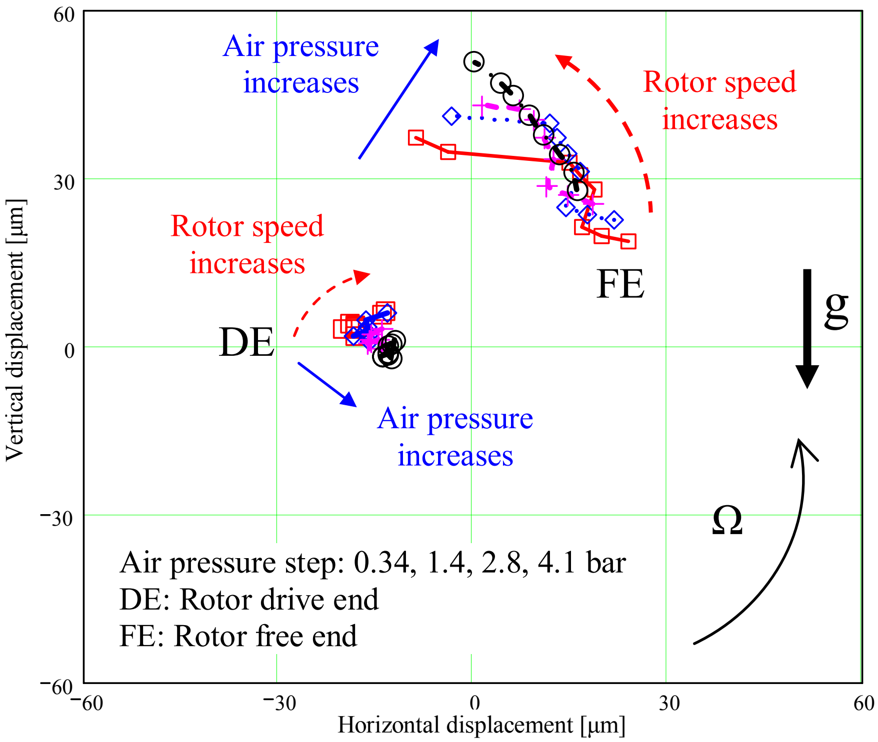

Figure 30 Trajectory of rotor center during speed-up tests with increasing side end pressures. Speed-up responses from 11 krpm to 50 krpm. DC-offset subtraction. Out-of-phase imbalance mass of 110 mg. Measurement at rotor drive and free ends. GFBs with shims.

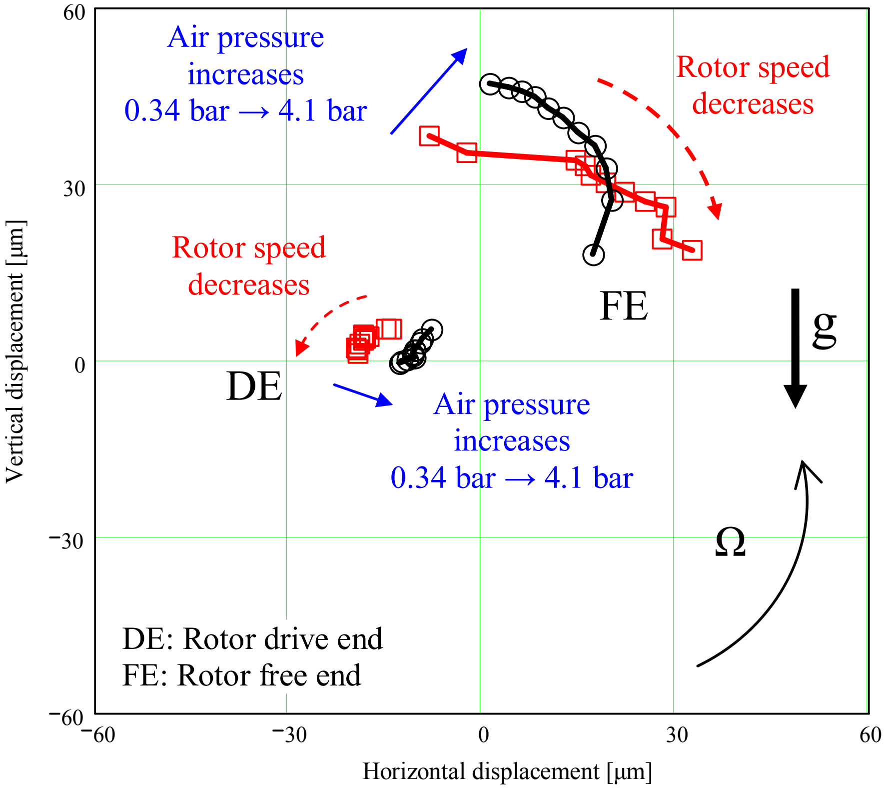

Figure 31 Trajectory of rotor center during rotor coastdown tests from 50 krpm with side end gauge pressures of 0.34 bar and 4.1 bar. DC-offset subtraction. Out-of-phase imbalance mass of 110 mg. Measurement at rotor drive and free ends. GFBs with shims.

Figure 32 displays the rotor speed versus time for the modified GFB with mechanical preload (shims) operating with side end gauge pressures of 0.34 bar and 4.1 bar (baseline imbalance). The results are compared to those for the original GFBs (without shims) at a side end gauge pressure of 0.34 bar [78]. In general, all results display an exponential decay of rotor speed with time from 50 krpm to 10 krpm, thus implying an operation with "viscous" drag. From 5 krpm until rest, rotor operation shows dry friction effects (rotor rubs) with a fast deceleration to rest. Note that the rotor may touch down earlier in shimmed GFBs, at 0.34 bar gauge, because of the bearings' smaller clearances.

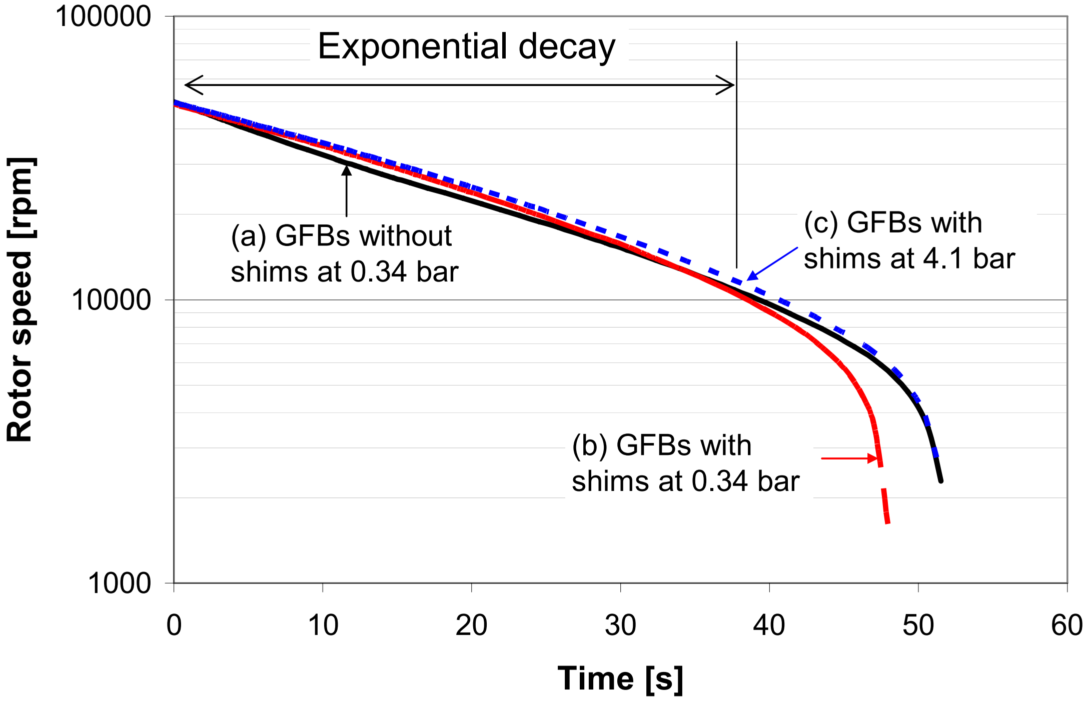

Figure 32 Rotor speed versus time during coastdown tests from 50 krpm for the original GFBs and the GFBs with shims. Baseline imbalance condition for (a) and (c). Out of phase imbalance mass of 110 mg for (b).

Conclusions

The exhaustive rotordynamic measurement of a rotor supported on GFBs demonstrates the performance of the original and shimmed bump type GFBs operating with side end pressurization. The present work is unique, with results and verifications first reported.

Rotordynamic response measurements of a test rotor supported on GFBs are conducted during rotor speed-up and coastdown tests. The GFBs are fed with side end air gauge pressures to 4.1 bar (60 psig). Side end pressurization demonstrates the dramatic effect of end gas pressurization on reducing the total amplitude of motions, mainly composed of subsynchronous whirl frequencies. For sufficiently high side end pressures into the bearings, the shaft subsynchronous whirl motions disappear; i.e. the test system becomes rotordynamically stable.

Normalized synchronous amplitudes recorded during coastdown rotor responses from 25 krpm show a linear rotor response behavior when using moderately small imbalance masses of 55 mg, 110 mg, and 165 mg. A large imbalance mass of 330 mg causes an increase in normalized peak amplitudes of synchronous response and at a lower critical speed, due to a reduction in equivalent viscous damping, when compared to those for small to moderate imbalance conditions. A reduction in equivalent viscous damping may be attributed to a decrease in dry-friction type energy dissipation at the natural frequency of the rotor-GFB system with a large imbalance (dynamic) force [80].

Installation of metal shims under the foil bearing bump strip layers and in contact with the bearing cartridge introduces mechanical preload into the test GFBs. The preload increases the threshold speed of instability where subsynchronous motions suddenly appear with large amplitudes. Bearing side end pressurization to 4.1 bar (60 psig) significantly delays this threshold speed. Estimated loci of static rotor centerline show that side end pressurization aids to reduce cross-coupled effects that destabilize the rotor-bearing system at high rotational speeds. Rotor speed versus time measurements obtained during speed coastdown tests, for the original GFBs and shimmed GFBs, display an exponential decay from 50 krpm to 10 krpm, thus evidencing an operation with “viscous” drag. However, the shimmed GFBs lead to higher (earlier) rotor touch-down speeds. This effect is undesirable for it accelerates the wear of the top foil and shaft coatings. Obviously, shimmed GFBs require more torque for rotor lift-off at start-up.

CHAPTER V

A MODEL OF GFBS WITH SIDE END PRESSURIZATION AND PREDICTIONS COMPARED TO ROTORDYNAMIC MEASUREMENTS

Introduction

This chapter presents a new physical model of GFBs supplied with end gas pressurization. The gas film model is governed by the modified Reynolds equation including the evolution of the gas circumferential flow velocity along the axial plane due to the imposed side end pressure. The 2D FE model of the top foil supported on bump strip layers described in chapter IV is coupled to the gas film model to predict the performance of GFBs with side end pressurization. A simple stability analysis [18] gives the rotordynamic characteristics of the test GFB with side end pressurization. The predicted threshold speed of instability is in close agreement with test measurements.

A model for GFBs with machined mechanical preload predicts the performance of shimmed GFBs. An ad-hoc function describes the radial clearance modified after installation of the shims. The shimmed GFB generates significant hydrodynamic pressures with peaks at the three shim locations, while the original GFB shows much lower film pressures. Installation of shims into the GFBs leads to an increase in direct stiffness and damping coefficients. Changes in cross-coupled force coefficients are relatively small.

A linear finite element rotordynamic analysis (XLTRC2®) models the test rotor supported on GFBs and predicts the system rotordynamic stability and synchronous rotor responses (amplitude and phase angle), both in good agreement with test measurements. Note that an extensive comparison of both rotor amplitude and phase angle is the only way to ensure the quality of the model predictions. Such extensive measurements have not been reported in the open literature, until now.

Gas Foil Bearing with End Pressurization

Computational model

Figure 33 shows a schematic depiction of a GFB and a journal rotating with angular speed *Ω*. An imposed pressure differential (p_s-p_a) forces a cooling flow through the foil bearing. The graph depicts the evolution of gas velocities through the inner and outer flow regions. The inner flow, between the rotating journal and top foil, is characterized by a minute film thickness (*h*). The outer flow passing through the back end of the top foil has a much larger gap, typically same as a bump height.

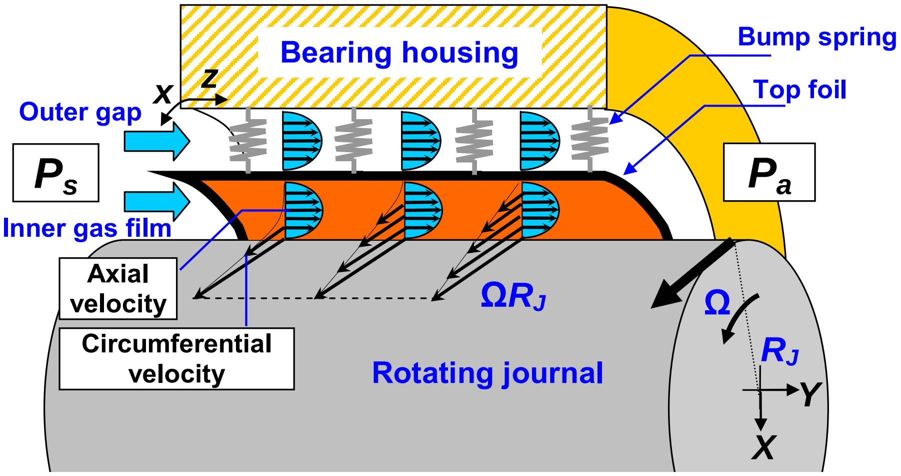

Figure 33 Flow induced by side end pressure in a foil bearing. Schematic view of evolution of gas velocities between journal and top foil (inner film flow) and between top foil and bearing housing (outer flow).

San Andrés at al. [17] observes that the axial flow rate induced by side end pressurization retards the development of the mean circumferential flow velocity (u_c) within the GFB, as is commonly asserted in annular pressure seals [68,69]. For centered journal operation, the gas mean flow circumferential velocity varies along the axial coordinate z [68] as

$$u_c = \frac{\Omega R_J}{2}\left(1-e^{-\delta z}\right)+\alpha\,\Omega R\,e^{-\delta z} \tag{7}$$

where $\delta = 12\mu/(\dot{m}_z c^2)$; $\dot{m}_z = \dfrac{c^2}{24\mu\Re T}\dfrac{\left(p_s{}^2 - p_a{}^2\right)}{L}$ (8)

$\Re$ =287 J/kg-K and viscosity μ = 1.87 ×10^{-5} Pa-s for air. $\dot{m}_z$ is the axial flow rate through the film, and α is an inlet flow pre-swirl factor. Note that as $z \rightarrow \infty$, $u_c \rightarrow 0.5\ \Omega R$, i.e. 50 % of rotor surface speed.

Figure 34 shows the effect of (a) side end pressurization and (b) inlet flow pre-swirl factor on the axial evolution of the circumferential flow velocity. Without inlet flow pre-swirl (α = 0), i.e., the gas has null circumferential flow velocity at the inlet plane (z/L = 0). The circumferential flow velocity increases along the axial coordinate, approaching half rotor speed ($u_c/\Omega R$ = 0.5) at the exit (discharge) plane. As side end pressure increases, the axial location where $u_c/\Omega R$ = 0.5 moves toward the bearing exit plane, thus implying a decrease in the overall circumferential flow velocity.

In Fig. 34 (b), for a fixed side end pressure (P_s = 4.1 bar), the circumferential flow velocity grows more rapidly toward $u_c/\Omega R$ = 0.5 as the inlet flow pre-swirl factor increases. The present analysis takes a null inlet flow pre-swirl factor, i.e., α = 0, since in the tests the side end pressurized air flow is impinged directly into one bearing end, see Fig. 33. That is, a negligible rotation of the fluid at the bearing inlet plane is assumed.

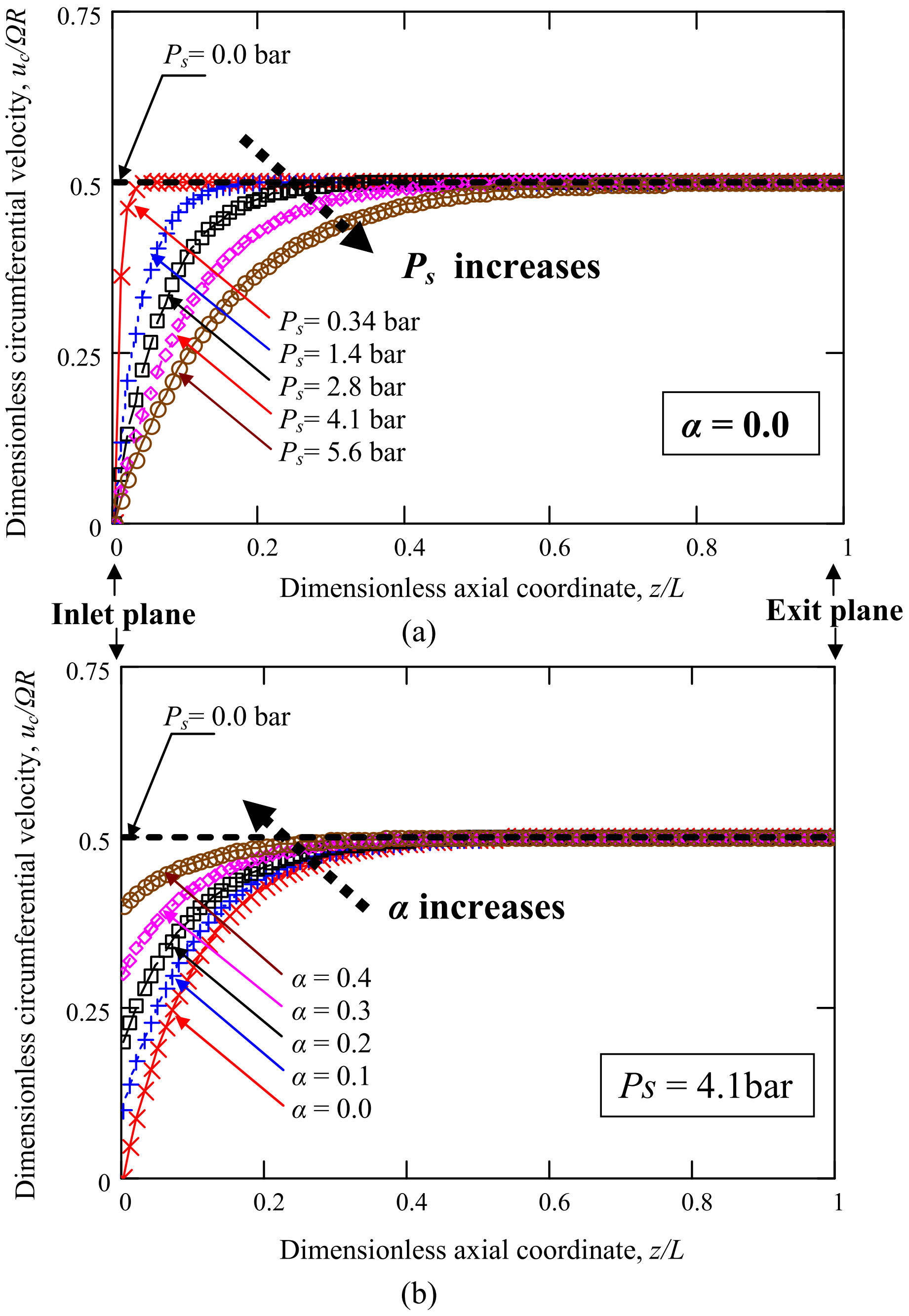

Figure 34 Dimensionless circumferentially averaged flow velocity versus dimensionless bearing length for (a) increasing side end (gauge) pressures, P_s, and a null inlet flow pre-swirl factor, α= 0.0, and (b) increasing inlet flow pre-swirl factor, α, and a constant side end (gauge) pressure, P_s = 4.1 bar.

The ideal isothermal and isoviscous gas film pressure *(p)* within the foil bearing is governed by an appropriately modified Reynolds equation incorporating the evolution of circumferential flow velocity,

$$\frac{\partial}{\partial x}\left(ph^3\frac{\partial p}{\partial x}\right)+\frac{\partial}{\partial z}\left(ph^3\frac{\partial p}{\partial z}\right)=12\mu\left[\left(1-e^{-\delta z}\right)\frac{\Omega R}{2}\frac{\partial(ph)}{\partial x}+\frac{\partial(ph)}{\partial t}\right] \tag{9}$$

in the film region $\{0<x=\Theta R<2\pi R,\ 0<z<L\}$. The film thickness ($h$) for an aligned journal is $h=c+e_X cos(\Theta)+e_Y sin(\Theta)+w_d$, where ($e_X$, e_Y) are journal center displacements and w_d is the deflection field of the underlying support structure. w_d is proportional to the pressure differential (p-p_{sub}) and a function of the material, thickness and geometry of the top foil modeled with shell FEs and the underlying elastic support structure. The flow of gas through the outer region behind the top foil is only axial, not greatly restricted by the bearing underspring structure.

The boundary conditions for the gas film pressure field are $p(\Theta,0)=p_s$, $p(\Theta,L)=p_a$, and $p(\Theta_\eta,z)_{\eta=l,t}=p_{sub}(z)$ at the leading (Θ_l) and trailing (Θ_t) edges of a top foil. The gas pressure behind the top foil (P_{sub}) equals:

$$p_{sub}(z)=\left[p_s^{\,2}\left(1-\frac{z}{L}\right)+p_a^2\left(\frac{z}{L}\right)\right]^{0.5} \tag{10}$$

As in Ref. [31], small amplitude journal motions about an equilibrium position render PDEs for the zeroth- and first- order pressure fields; from which, prediction of the GFB reaction forces and force coefficients, stiffness and damping, $[K_{\alpha\beta},\ C_{\alpha\beta}]_{\alpha\beta=X,Y}$, follow. The model does not include thermal energy transport considerations since these were unimportant for the laboratory test conditions.

During the rotordynamic tests, insignificant changes (<5 ºC) in temperature of the test GFBs were recorded. Therefore, the present study considers that thermal effects are of no importance on the performance of the tested GFBs.

Predicted bearing performance

Figure 35 introduces a layout of the TAMU rotor-GFBs test rig and instrumentation, fully described in chapter IV. The test rotor weighing 1 kg is supported on two GFBs, each of length and diameter equal to 38.1 mm. The test rig housing holds two test GFBs and contains an internal duct to supply air pressure up to 7 bars (100 psig). The side end pressurization at rotor midspan forces a cooling flow through the test GFBs.

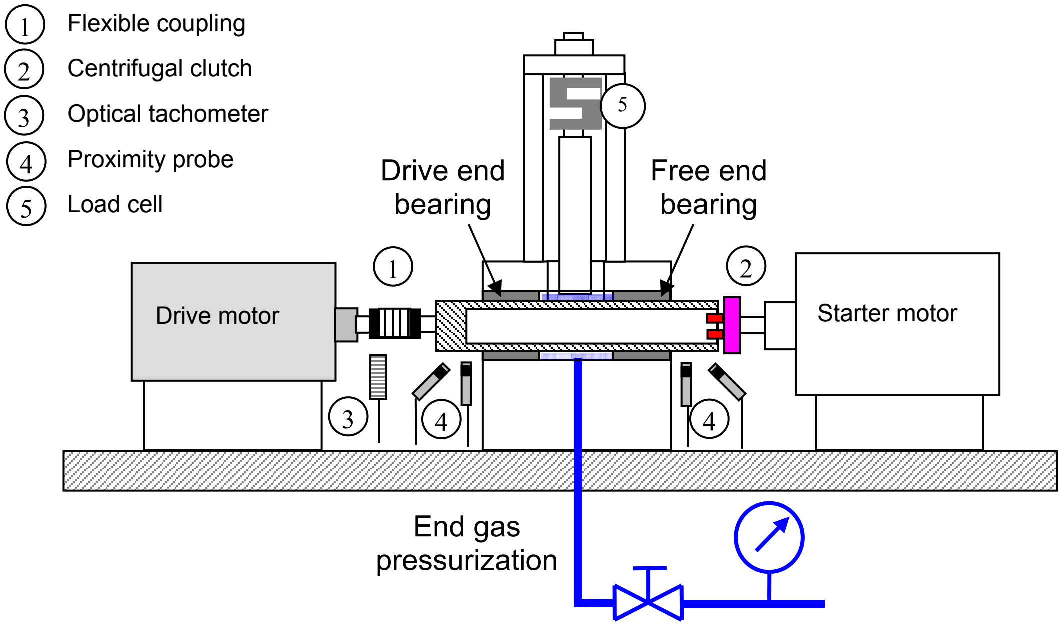

Figure 35 Layout of rotor-GFBs test rig and instrumentation.

Model predictions follow for the free end GFB tested in chapter IV. For rotor operation at 30 krpm (500 Hz), Fig. 36 shows the pressure differential, top foil deflection, and film thickness versus bearing axial length for (a) null side end (gauge) pressure, P_s = 0.0 bar and (b) increased side end (gauge) pressure, P_s = 3.0 bar. Note that the pressure differential (p-p_{sub}) directly affects the top foil deflection and film thickness. With side end pressurization, P_s = 3.0 bar, the peak pressure differential value increases and its axial location shifts from the bearing mid-plane toward the bearing end. The film thickness decreases with side end pressurization, albeit the film thickness change along the axial length is relatively small (<5 μm), both for P_s = 0.0 bar and P_s = 3.0 bar, to the film thicknesses (>30 μm), thus implying the taper shape film thickness may not affect significantly the bearing stiffness and damping coefficients. With side end pressurization, the axial location within the bearing where the maximum film thickness and top foil deflection occur shifts from the bearing mid-plane toward the bearing end discharge.

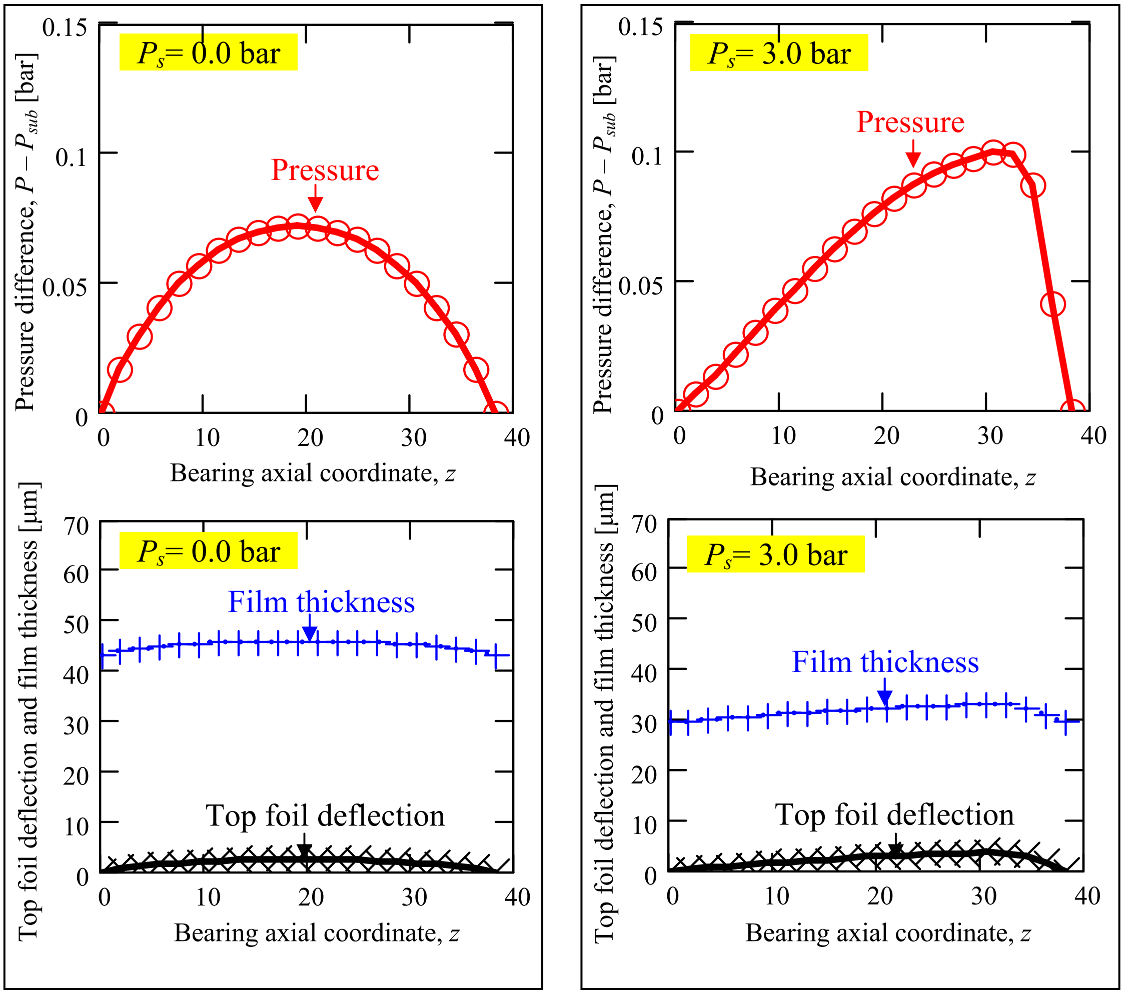

(a) (b)

Figure 36 Gas peak pressure differential, top foil deflection, and minimum film thickness versus axial coordinate for (a) null side end (gauge) pressure, P_s = 0.0 bar and (b) with side end (gauge) pressure, P_s = 3.0 bar. Static load 4.9 N. Rotor speed: 30 krpm (500 Hz). α = 0.0.

Figure 37 shows the predicted journal eccentricity and attitude angle versus end (gauge) pressure. As the side end pressure increases, the predicted journal eccentricity increases and journal attitude angle decreases. Note that test measurements with side end pressurization show small static rotor motions along the horizontal direction as the rotor speed increases, thus implying a reduction in cross-coupled effects.

In Fig. 38, as the side end pressure increases, the minimum film thickness and drag torque decrease. The axially fed gas flow due to side end pressurization retards the evolution of gas velocities in the circumferential direction, thus decreasing the bearing drag torque and minimum film thickness, and increasing the operating journal eccentricity.

Figure 39 shows predicted (a) direct (K_{XX}, K_{YY}) and cross-coupled (K_{XY}-K_{YX}) stiffnesses and (b) direct (C_{XX}, C_{YY}) damping coefficients versus excitation frequency at shaft speed of 30 krpm (500 Hz). Direct stiffnesses and damping coefficients grow as side end pressurization increases. Most importantly the difference (K_{XY} -K_{YX}) decreases at low frequencies denoting a net gain in bearing stability. Note also that all force coefficients are strongly frequency-dependent functions.

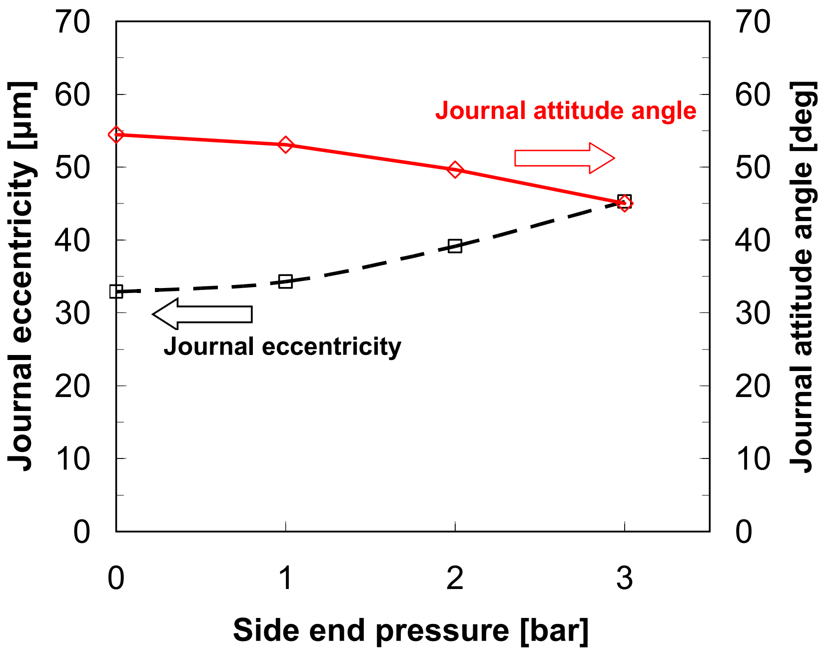

Figure 37 Predicted journal eccentricity and attitude angle versus side end (gauge) pressure. Static load 4.9 N. Rotor speed: 30 krpm (500 Hz).

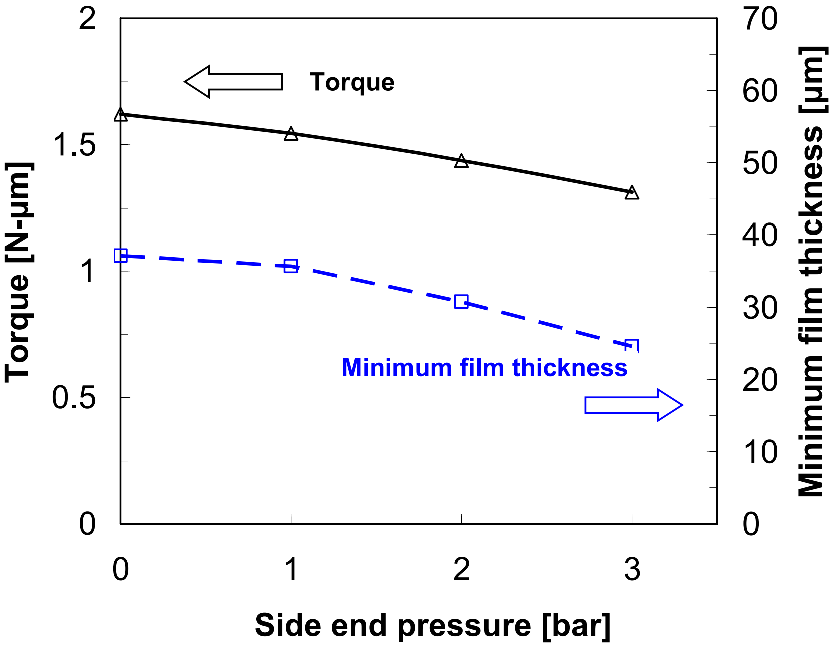

Figure 38 Predicted bearing drag torque and minimum film thickness versus side end (gauge) pressure. Static load 4.9 N. Rotor speed: 30 krpm (500 Hz).

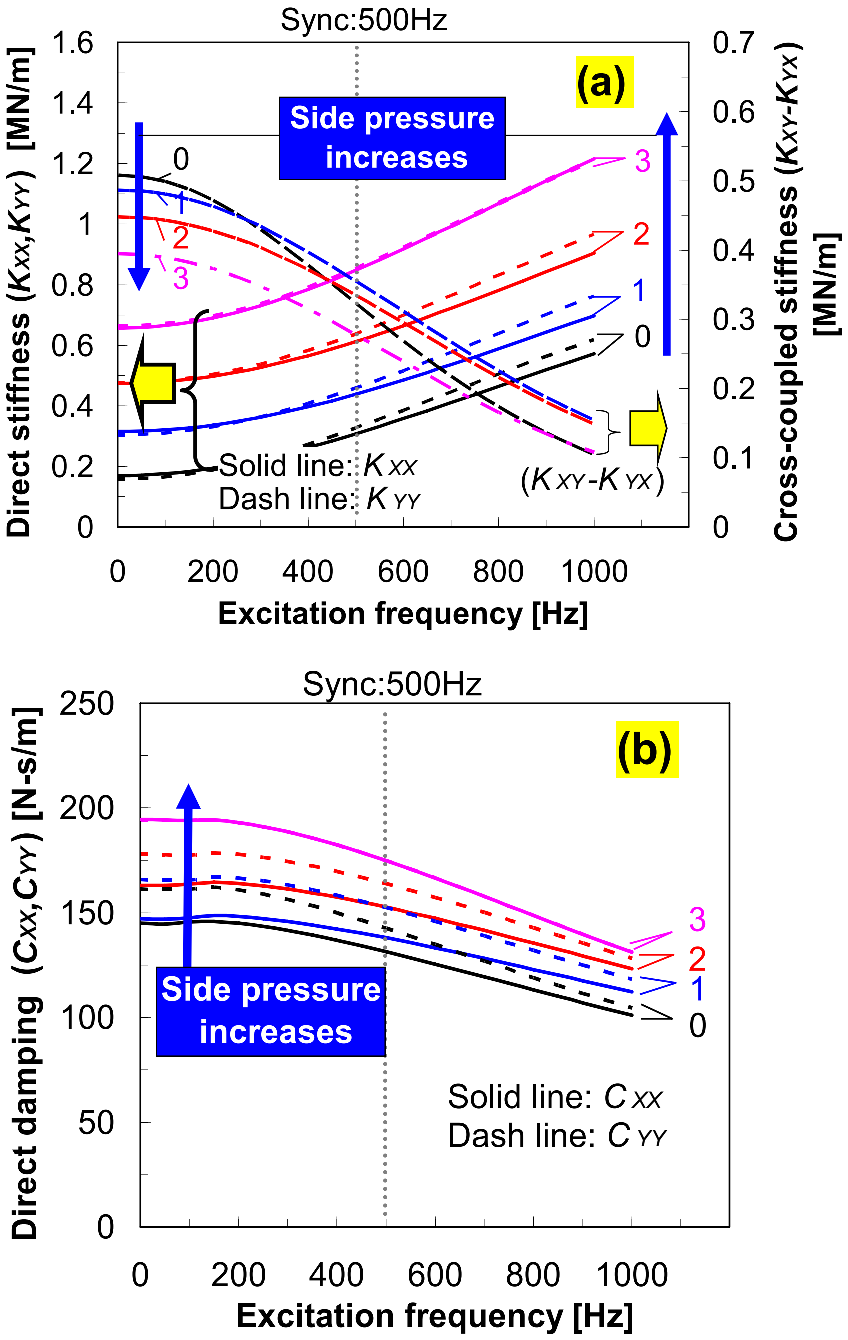

Figure 39 Effect of side end pressurization on test GFB force coefficients. (a) Direct and cross-coupled stiffnesses (b) direct damping coefficients. Numbers denote magnitude of side end (gauge) pressure, P_s [bar]. Static load 4.9 N. Rotor speed: 30 krpm (500 Hz).

Predictions and comparisons to test data

A simple eigenvalue analysis of the test rotor-GFBs follows Lund's approach [18] to determine stability parameters: critical mass and whirl frequency ratio (*WFR*), defined as the ratio between whirl frequency and angular shaft speed. For a shaft speed of 30 krpm and rotor ½ mass of 0.5 kg, Figure 40 shows a magnitude of side end pressure, ≥ 2.9 bar, needed to ensure stable rotor operation, i.e. free of subsynchronous whirl. Note that, in Fig. 41 (duplicated from chapter V), the measured rotor subsynchronous whirl motions disappear for side end pressures ≥ 2.8 bar, i.e. the test system becomes rotordynamically stable.

Figure 42 compares the predicted natural frequency to measured subsynchronous frequency as the end (gauge) feed pressure increases. At P_S=3 bar, the predicted whirl frequency is 165 Hz, i.e. whirl frequency ratio (*WFR*) is 0.33=165Hz/500Hz*,* while that determined from the measurements is 147 Hz, i.e. WFR is 0.29=147Hz/508Hz (see also Fig. 19).

The agreement between the predicted threshold speed of instability and the measured onset speed of subsynchronous motion in Fig. 41 is remarkable.

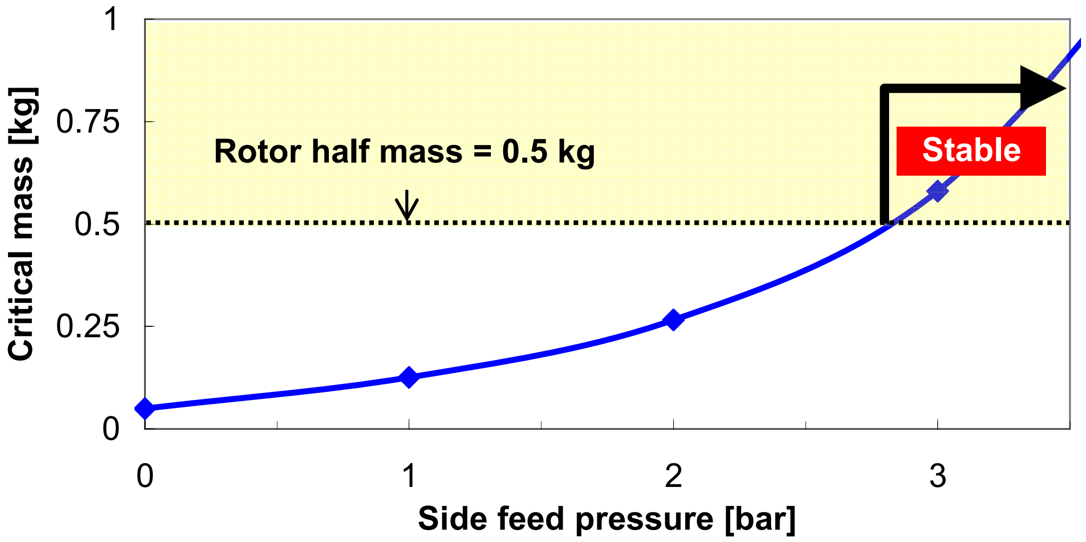

Figure 40 Predicted critical mass versus side end (gauge) feed pressure for operation of GFB. Static load 4.9 N. Rotor speed: 30 krpm (500 Hz).

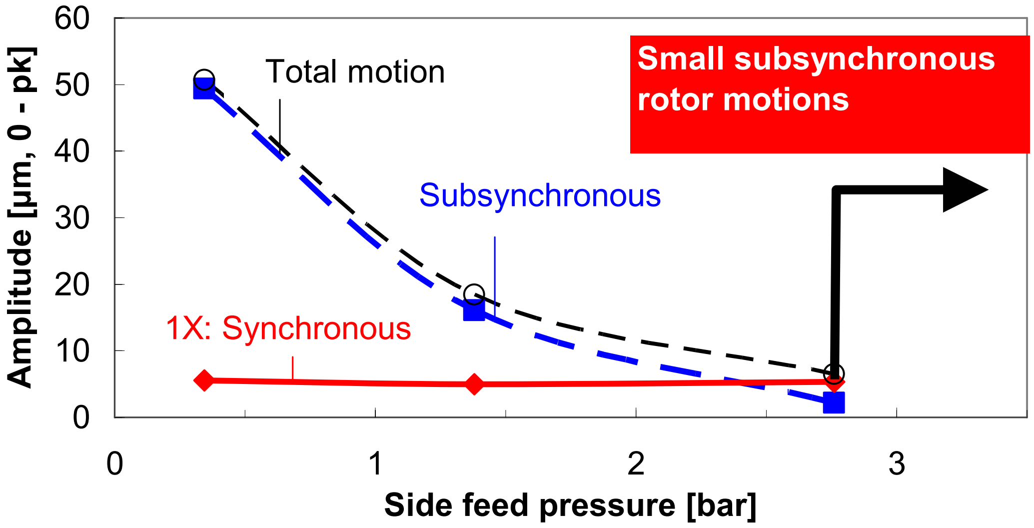

Figure 41 Amplitudes of total shaft motion, and synchronous and subsynchronous components versus side end gas pressurization. Rotor speed : 30 krpm (500 Hz).

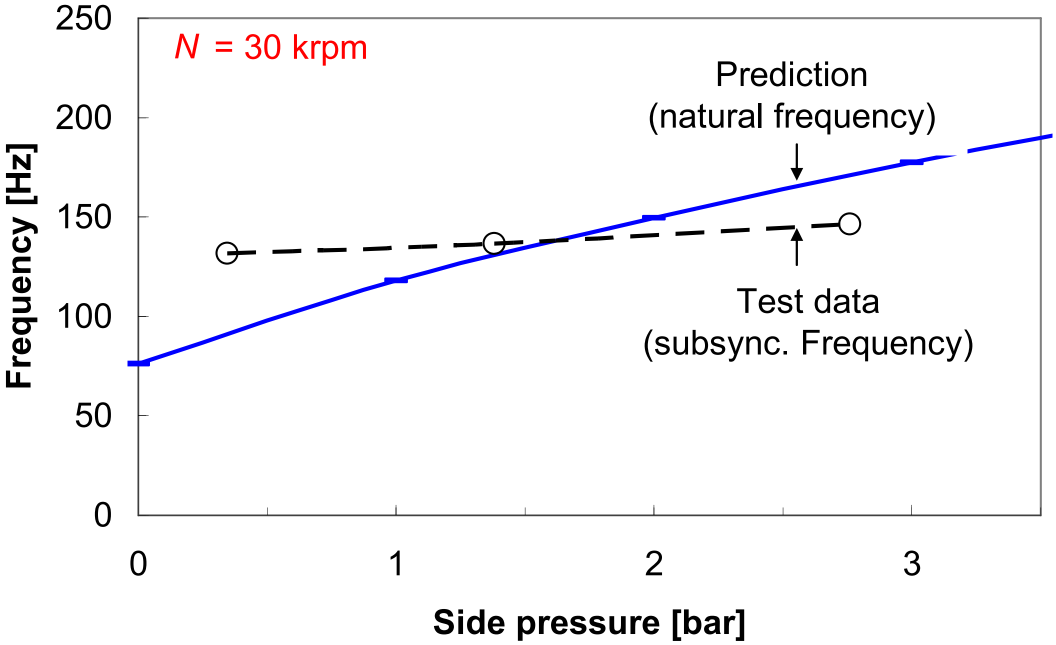

Figure 42 Predicted system natural frequency and measured subsynchronous whirl frequency versus side end (gauge) pressure. Static load 4.9 N. Speed: 30 krpm (500 Hz).

Performance of Shimmed Gas Foil Bearings

Chapter IV demonstrates that shimmed gas foil bearings delay the onset speed of large subsynchronous rotor motions during rotor speed-up (acceleration) tests. The test GFBs have three metal shims installed under a bump strip layer and in contact with the bearing cartridge at three angular locations, as shown in Fig. 43. Chapter IV provides the geometry and material properties of the test shimmed GFBs (see Table 3 for the geometry of test GFBs).

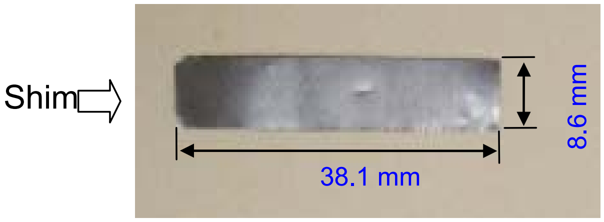

25.4 μm thickness shim

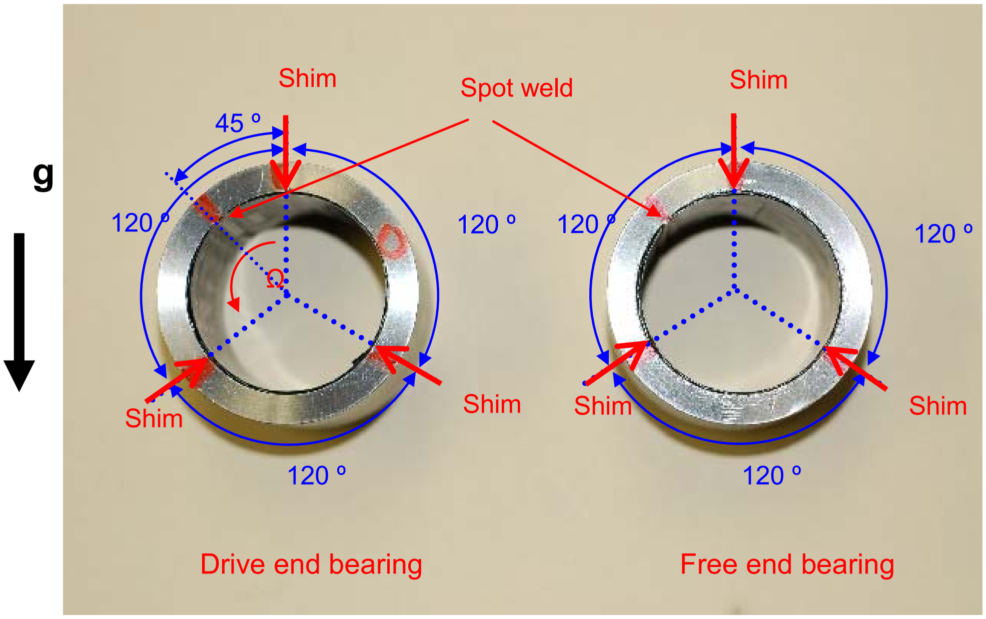

Figure 43 Locations of three shims relative to top foil spot-weld in test bearings.

Figure 44 illustrates schematic views of (a) structural top foil and bump strip layer with shims, and (b) an approximation to the assembly radial clearance of the shimmed GFB for a nominal clearance of 35 μm as provided by the manufacturer[8]. Three metal shims of 25.4 μm thickness, 26 ° angular extent, and 38.1 mm length installed under the bump strip and with an angular distance, 120 ° reduce by the shim thickness the radial assembly clearance of test GFBs at three angular locations. A sinusoidal function approximately depicts the modified assembly radial clearance[9] as shown in Fig. 44.

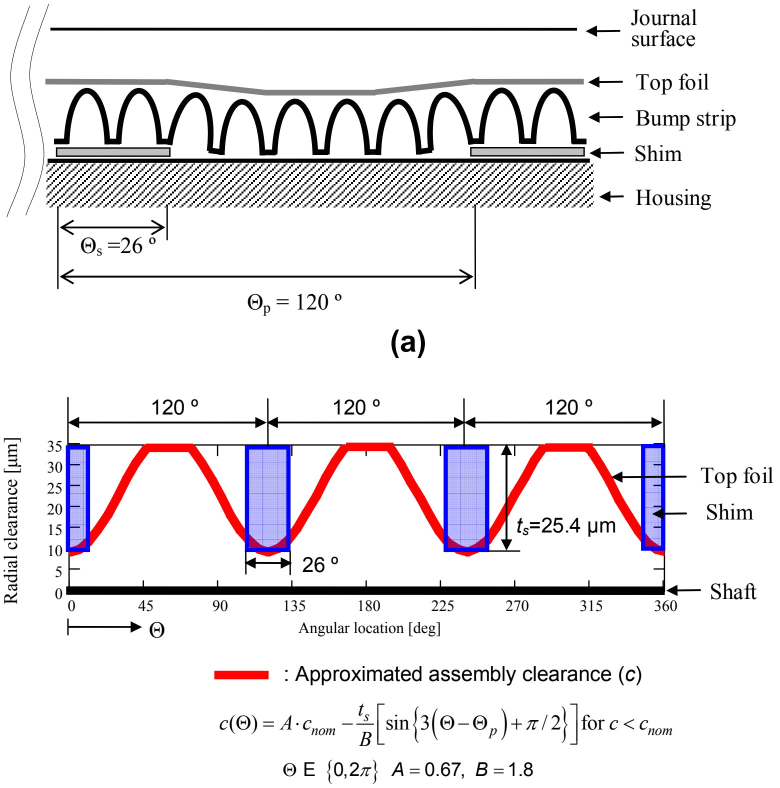

$$c(\Theta) = A \cdot c_{nom} - \frac{t_s}{B}\left[\sin\left\{3\left(\Theta - \Theta_p\right) + \pi/2\right\}\right] \text{for } c < c_{nom}$$

$$\Theta \text{ E } \{0, 2\pi\} \quad A = 0.67, \; B = 1.8$$

(b)

Figure 44 (a) Schematic view of a structural foil layer with shims and (b) approximation of radial assembly clearance of GFB with three shims.

---

[8] Radial clearances in the test GFBs are generally unknown. A load-deflection test (see Appendix G) reveals the structural stiffness coefficients < 1×10^5 N/m within nominal radial clearances, c = 40 μm and 70 μm estimated for the drive and free end GFBs, respectively. Thus, the GFBs have an interference contact with the rotor at rest. A small gap between the rotor and the top foil, i.e. bearing clearance, is created as the rotor speed increases while pushing away the top foil.

[9] The top foil and bump strip layer around the shim locations make a smooth contour for a radial assembly clearance.

Figures 45a – 45c illustrate the predicted mid-plane pressure, top foil deflection, and film thickness versus angular location for the original and shimmed GFBs operating at increasing rotor speeds. Note that the top foil extends from 45 º to 395 º. For a small static load of 6.6 N, i.e. a fraction of the rotor mass for the drive end bearing, the GFB with shims generates significant hydrodynamic pressures with peaks at three shim locations, while the original GFB shows much lower hydrodynamic pressures, irrespective of the rotor speeds. As the rotor speed increases, the hydrodynamic pressures, structural deflections and minimum film thickness also increase for the GFB with shims. In Fig. 45b, the model prediction shows a sagging effect in the top foil deflection and also produces "negative" values at locations between two shims. Note that although the GFB with shims enhances the hydrodynamic pressure generation thus implying an increase in bearing stiffness, a reduction in the minimum film thickness, in particular at low rotor speeds, may lead to earlier rotor touch-down, which is undesirable from the viewpoint of top foil and shaft coatings endurance.

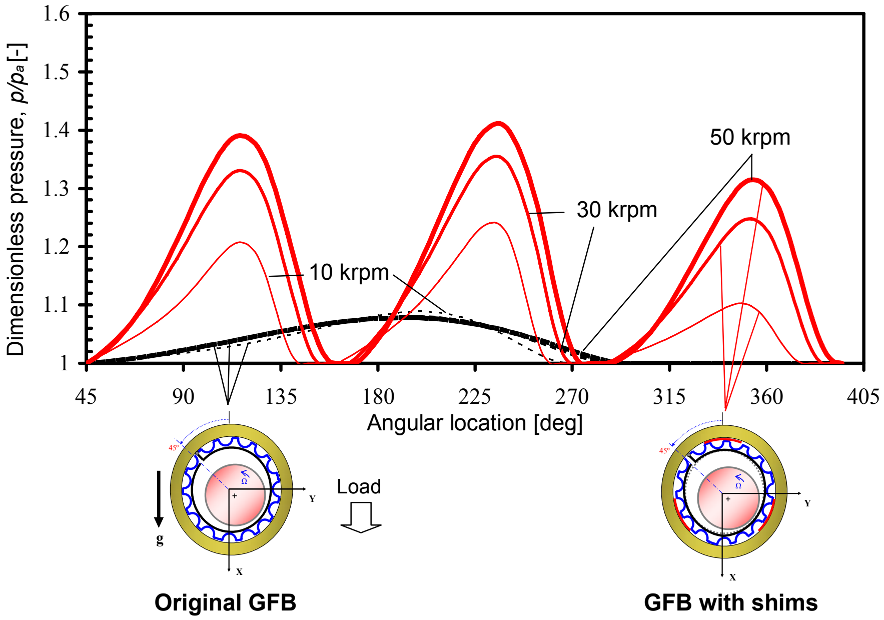

Figure 45a Dimensionless mid-plane pressure versus angular location for original and shimmed GFBs at increasing rotor speeds. Static load of 6.6 N.

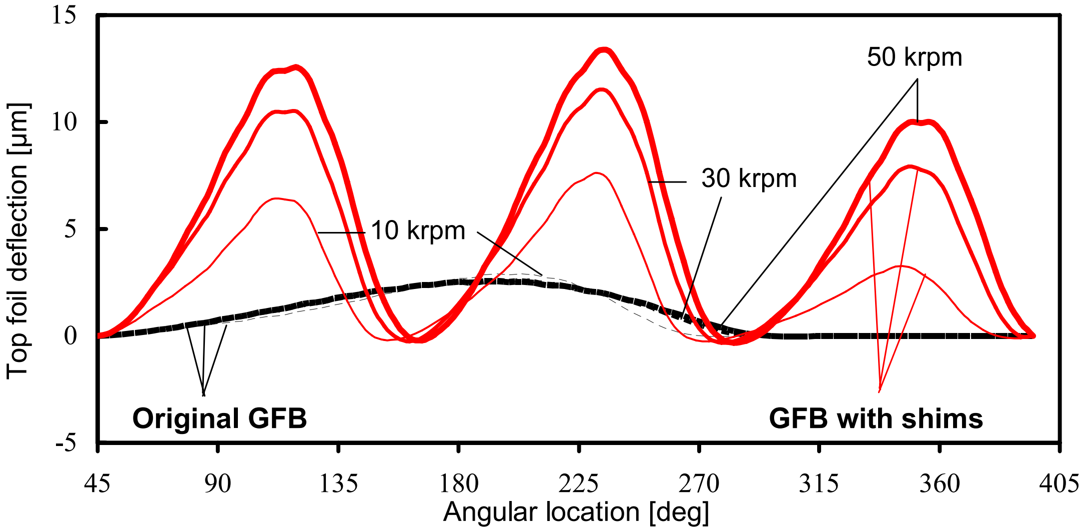

Figure 45b Mid-plane top foil deflection versus angular location for original and shimmed GFBs at increasing rotor speeds. Static load of 6.6 N.

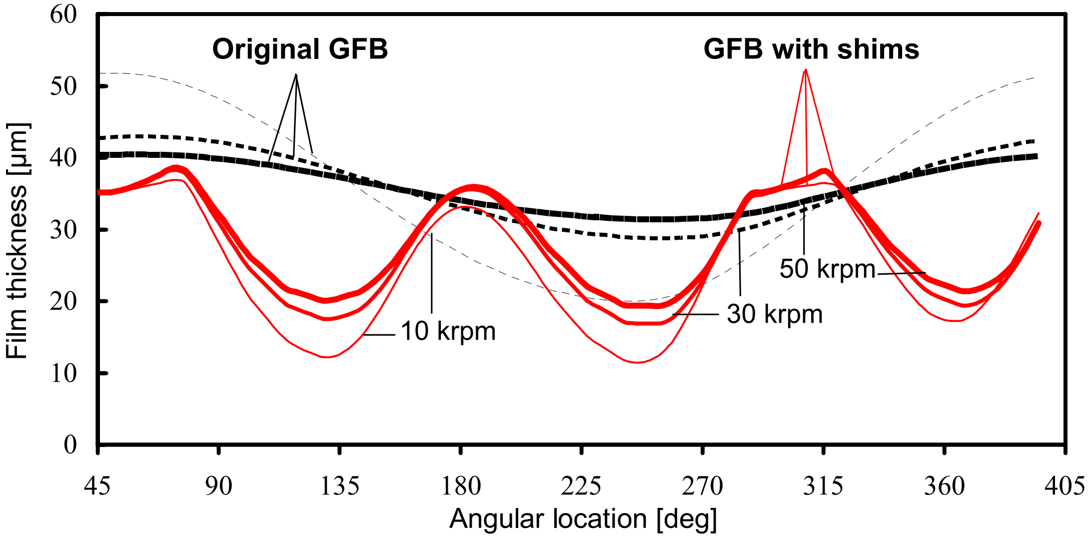

Figure 45c Mid-plane film thickness versus angular location for original and shimmed GFBs at increasing rotor speeds. Static load of 6.6 N.

Figures 46 and 47 display the predicted journal eccentricity versus rotor speed and journal attitude angle versus rotor speed, respectively, for the original GFB and shimmed GFB. A nominal radial clearance of 35 μm is used for both GFBs. The shimmed GFB has smaller journal eccentricity and attitude angle when compared to the original GFB. Note that the smaller journal attitude angle for the shimmed GFB implies reduced cross-coupled effects. See Appendix H for journal eccentricity versus rotor speed and journal attitude angle versus rotor speed for the (original and shimmed) free end GFBs. Recall Fig. 35 for the configuration of test rotor and the designation of the two GFBs.

Figures 48 and 49 present the predicted synchronous force (stiffness and damping) coefficients versus rotor speed for the original and shimmed GFBs, respectively. A structural loss factor $\gamma = 0.2$ for the original and the shimmed GFBs represents energy dissipation from dry-friction effects [49]. Installation of shims into the GFBs leads to an increase in direct stiffness (K_{XX}, K_{YY}) and direct damping (C_{YY}) coefficients. Changes in other coefficients are relatively small. Stiffness ($K_{XX} \sim K_{YY}$ and $K_{XY} \sim -K_{YX}$) damping ($C_{XX} \sim C_{YY}$ and $-C_{XY} \sim C_{YX}$) coefficients for the shimmed GFBs indicate an almost centered rotor operation over the entire rotor speed range. For both the original and shimmed GFBs, the magnitudes of direct stiffness (K_{XX}, K_{YY}) are larger than those of cross-coupled stiffness (K_{XY}, K_{YX}), in particular at high rotor speeds, thus favoring stable rotor performance. Appendix I provides the predicted stiffness and damping coefficients for the original and shimmed free end GFBs.

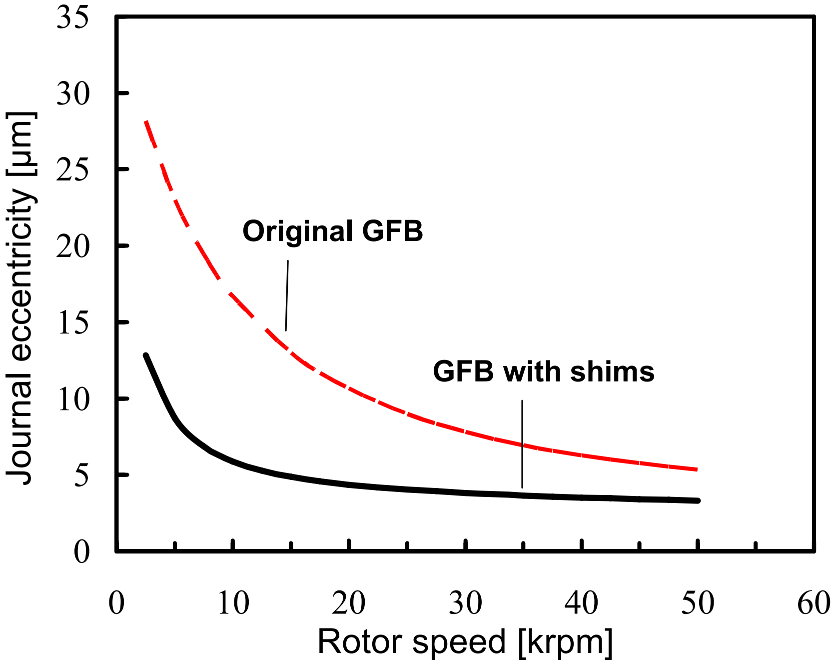

Figure 46 Predicted journal eccentricity versus rotor speed for original and shimmed GFBs. Static load of 6.6 N in vertical (*X*) direction. Drive end bearing.

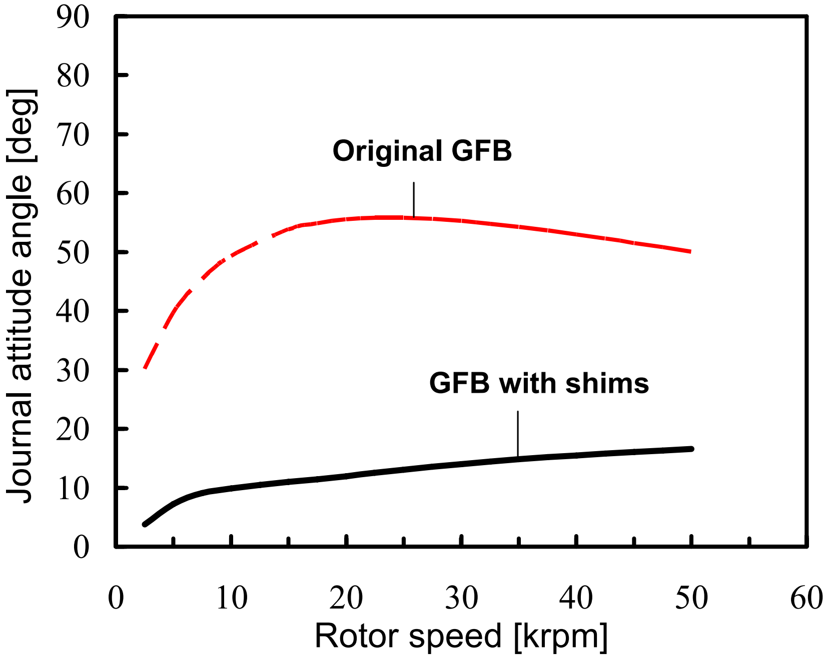

Figure 47 Predicted journal attitude angle versus rotor speed for original and shimmed GFBs. Static load of 6.6 N in vertical (*X*) direction. Drive end bearing.

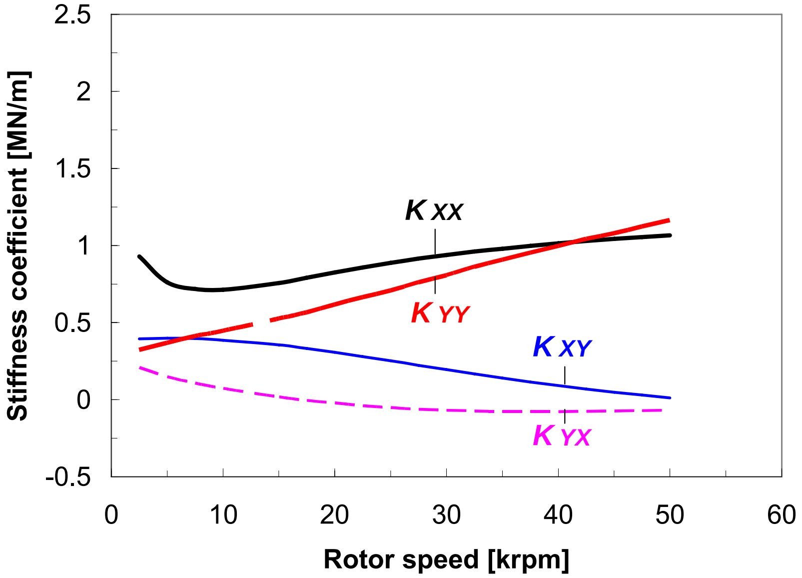

(a) Stiffness coefficients

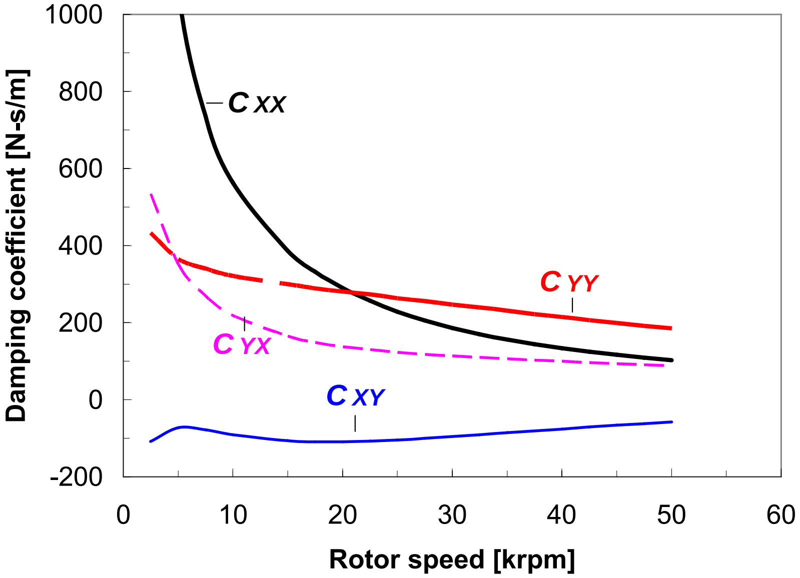

(b) Damping coefficients

Figure 48 Synchronous stiffness and damping coefficients versus rotor speed for original GFBs. Static load of 6.6 N in vertical (*X*) direction. Structural loss factor, $\gamma = 0.2$. Drive end bearing.

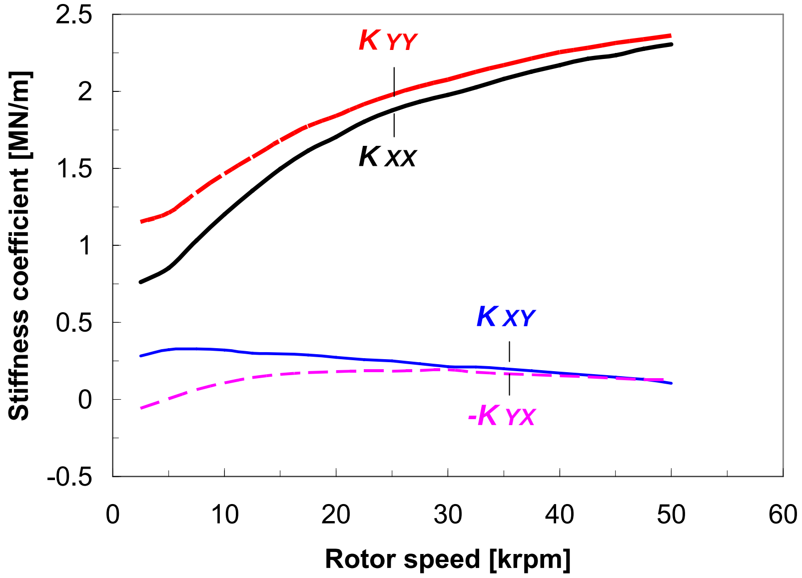

(a) Stiffness coefficients

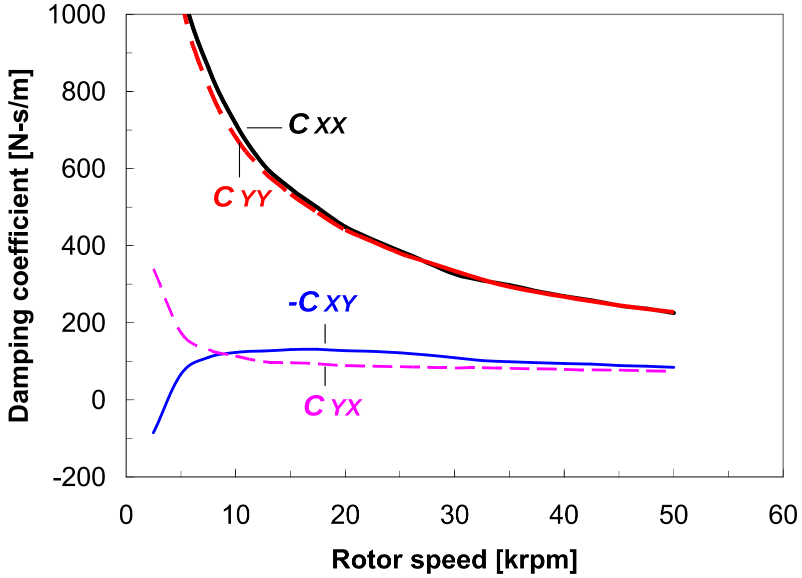

(b) Damping coefficients

Figure 49 Synchronous stiffness and damping coefficients versus rotor speed for GFBs with shims. Static load of 6.6 N in vertical (*X*) direction. Structural loss factor, $\gamma = 0.2$. Drive end bearing.

Rotor Response Predictions Compared to Test Data

Finite element model for rotor – bearing system

In Chapter IV, test measurements of rotor synchronous responses verify the linearity of the test rotor – GFBs system. A linear rotordynamics software (XLTRC^{2}$_{®}$) models the test rotor – GFBs system and predicts the rotor synchronous responses. Figure 50 shows the finite element structural model of the test rotor. The flexible coupling used in Ref. [17] is replaced with a softer one, i.e., the old and new coupling have estimated lateral stiffness coefficients of 1.63×10^{5} N/m and 1×10^{3} N/m, respectively. The connecting shaft in Ref. [17] is also replaced with a longer one of the same material, i.e., old and new connecting shafts have lengths of 30 mm and 46 mm, respectively. The modifications aid to isolate the rotor - GFB system from the drive motor system.

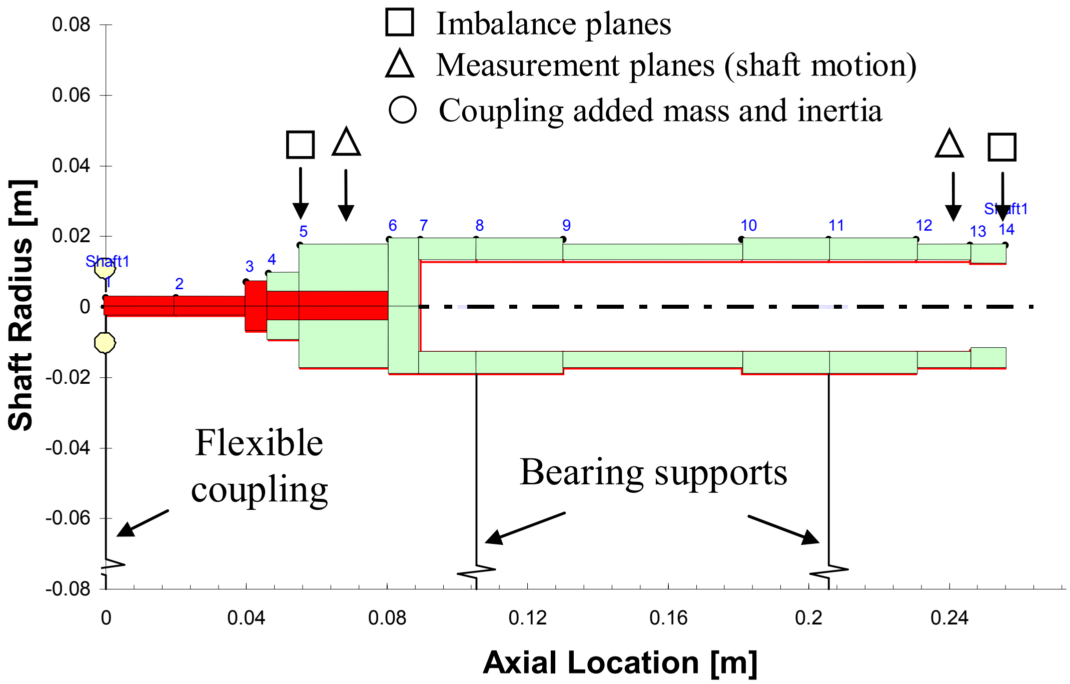

Figure 50 Finite element model of test rotor supported on two radial GFBs (with connecting shaft and flexible coupling).

Original foil gas bearings

An eigenvalue analysis predicts the rotor-GFBs system damped natural frequencies and damping ratios for the test speed range, using the predicted stiffness and damping coefficients[10] for original GFBs as shown in Figs. 48 and I1. No side end pressure is assumed for the model predictions compared to test measurements at a low side end pressure of 0.35 bar (5 psig).

Figure 51 shows the damped natural frequency map and predicted forward mode critical speeds at 3.25 krpm and 4.0 krpm, associated to cylindrical and conical modes, respectively. Figure 52 shows predicted damping ratios decreasing rapidly as rotor speed increases. A positive damping ratio indicates a stable system. Predicted damping ratios of ~ 0.5 at the critical speeds denote a well damped system.

Figures 53a and 53b compare the predicted phase angle and normalized rotor amplitude of synchronous responses to test measurements recorded during rotor speed coastdown tests from 25 krpm for in-phase and out-of-phase imbalance masses of 55 mg, 110 mg, 165 mg, and 330 mg at the drive end bearing location. The imbalance masses are added into the rotor end planes at radius (r) equal to 15.11 mm. For the smallest mass of 55 mg, imbalance displacements (u) are 1.3 μm and 2.3 μm (bases for normalization) at the drive and free end bearings, respectively. Note that the prediction based on linearized bearing force coefficients shows a unique curve. In general, the predictions are in good agreement with test data, phase angle and amplitude, for small to moderate imbalance masses, i.e. 55 mg to 165 mg, i.e. characteristic of a linear system. The rotor critical speed, where the rotor amplitude is largest, is determined at rotor speed higher than a system natural frequency, i.e. $\omega_{cr} = \omega_n / \sqrt{1-2\varsigma^2}$ [80].

On the other hand, for the largest imbalance mass of 330 mg, the comparison evidences a large discrepancy, in particular for rotor amplitudes around the system critical speed and phase angle above that speed. An increase in normalized rotor amplitude and different trend in phase angle from those obtained for small to moderate

---

[10] Predicted stiffness and damping coefficients for a nominal radial clearance of 35 μm, shown in Figs. 48, 49, I1, and I2 are used for original and shimmed GFBs.

imbalance masses are attributed to the system nonlinearity due to a reduction in viscous damping. Note that, without viscous damping, the rotor critical speed approaches the system natural frequency, i.e. $\omega_{cr} \rightarrow \omega_n$. Appendix J provides a comparison of the predicted synchronous responses to test measurements at the free end bearing. All predicted and measured synchronous rotor amplitudes approach the imbalance displacements (u) of 1.3 μm and 2.3 μm at the drive and free end bearing locations, respectively, as the rotor speed increases.

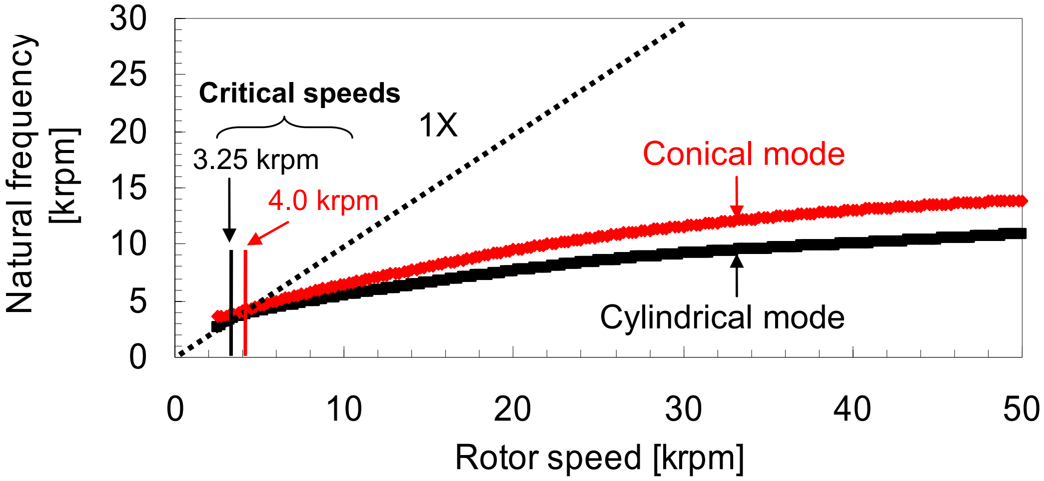

Figure 51 Predicted damped natural frequencies for rotor – GFB system (forward modes). Original GFBs.

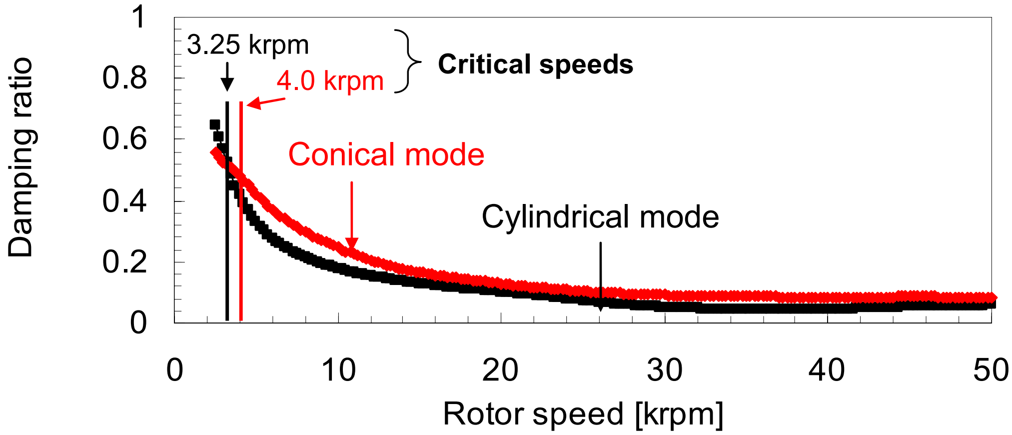

Figure 52 Predicted damping ratios (ς) for rotor – GFB system. Original GFBs.

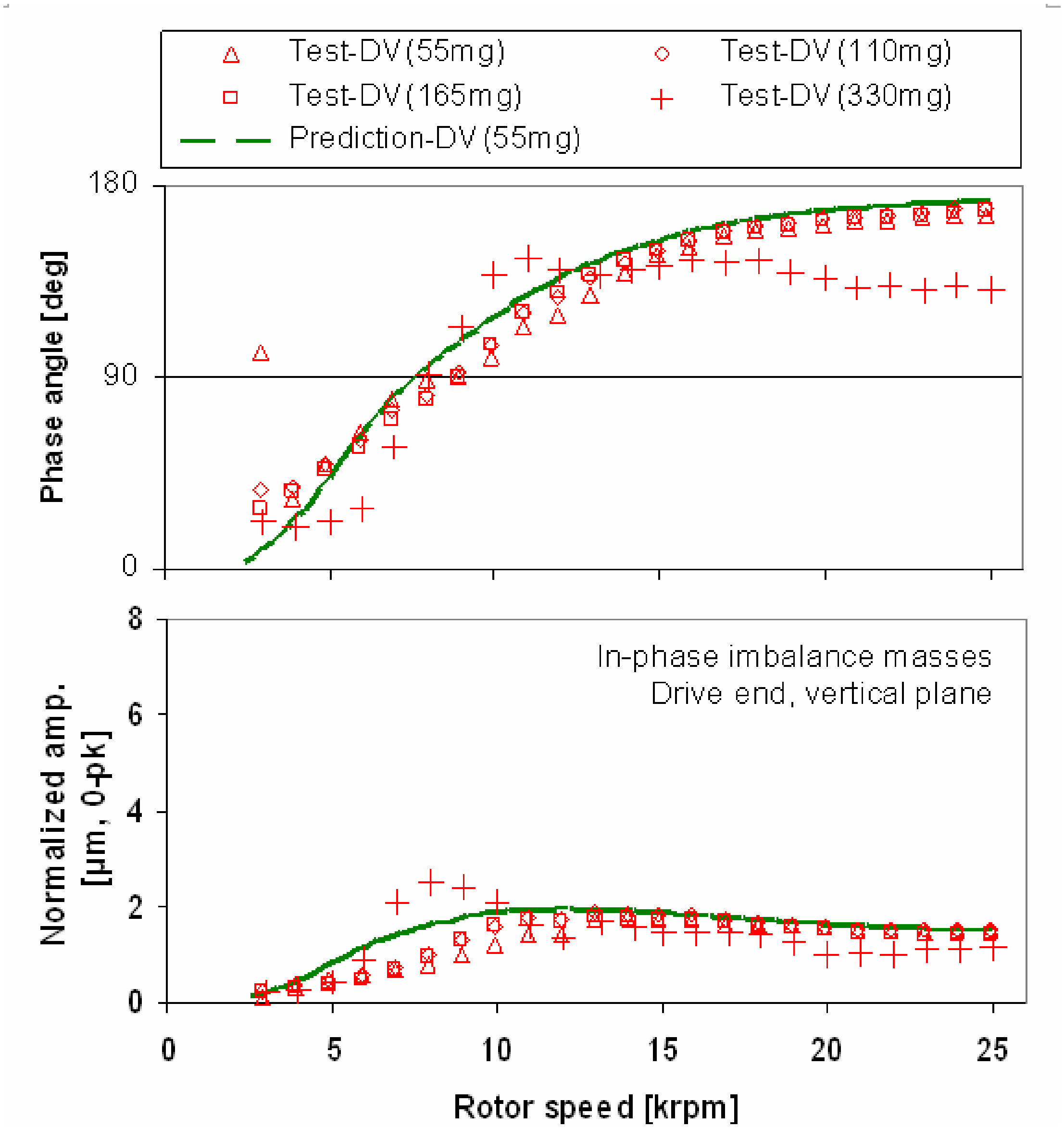

Figure 53a Phase angle and normalized rotor amplitude of synchronous response for increasing in-phase imbalance mass. Drive end, vertical plane. Predictions compared to test data. Original GFBs.

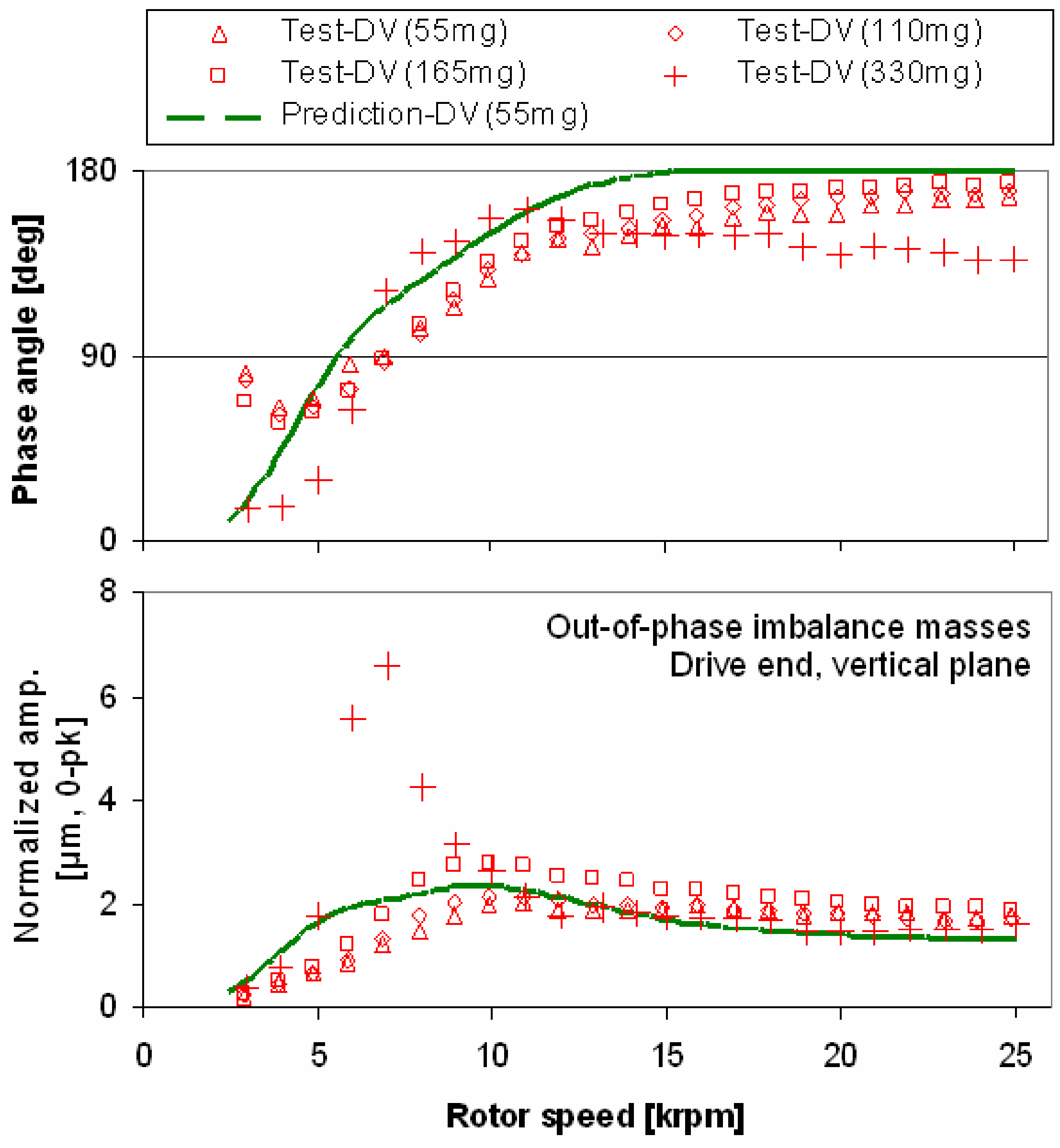

Figure 53b Phase angle and normalized rotor amplitude of synchronous response for increasing out-of-phase imbalance mass. Drive end, vertical plane. Predictions compared to test data. Original GFBs.

Shimmed foil gas bearings

Figures 54 and 55 present the damped natural frequency map with forward mode critical speeds and damping ratios, respectively, for the rotor- shimmed GFBs system. The predicted stiffness and damping coefficients in Figs. 49 and I2 are used in the rotordynamic prediction; but the damping coefficients are arbitrarily doubled[11]. The critical speeds at 7.5 krpm and 11 krpm are associated to conical and cylindrical modes, respectively. The positive damping in the speed range indicates rotordynamically stable rotor operation to 50 krpm.

Figures 56a and 56b compare the predicted phase angle and normalized rotor amplitude of synchronous responses to test measurements recorded during rotor coastdown tests from 35 krpm for in-phase and out-of-phase imbalance masses of 55 mg and 110 mg at the drive end bearing locations. In general, the predictions agree reasonably with test data, phase angle and amplitude, for small to moderate imbalance masses, i.e. 55 mg to 110 mg. See Appendix J for a comparison of the predicted synchronous responses to test measurements at the free end bearing.

---

[11] The structural loss factor for the shimmed GFBs is unknown. However, installation of shims is expected to facilitate dry-friction of the bumps, in particular at low rotor speeds, thus dissipating more energy. Presently, damping coefficients for the shimmed GFBs, predicted using a structural loss factor of 0.2, are arbitrarily doubled, i.e. $2\times C$'s for the rotordynamic analysis. Note that, for the light weight test rotor, an increase in the structural loss factor does not increase significantly the bearing damping coefficients, in particular at low rotor speeds.

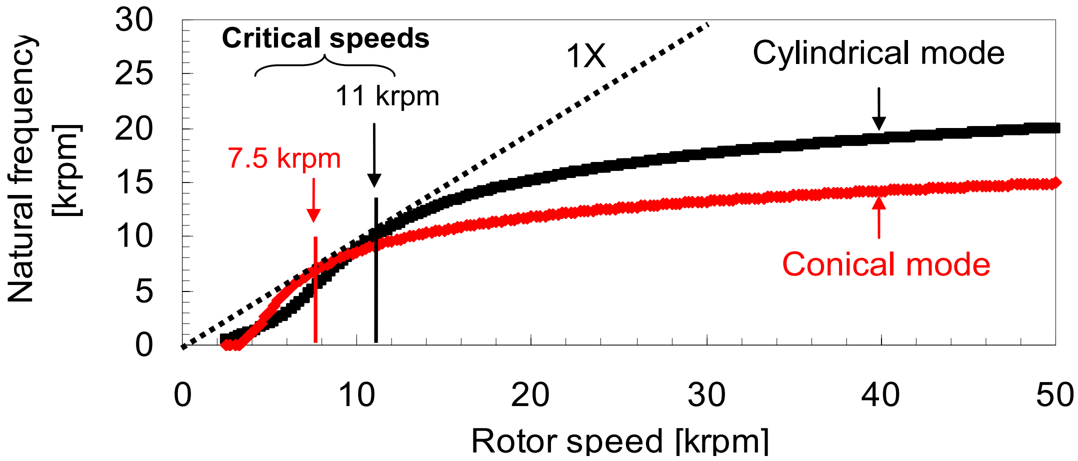

Figure 54 Predicted damped natural frequencies for rotor – GFB system (forward modes). GFBs with shims.

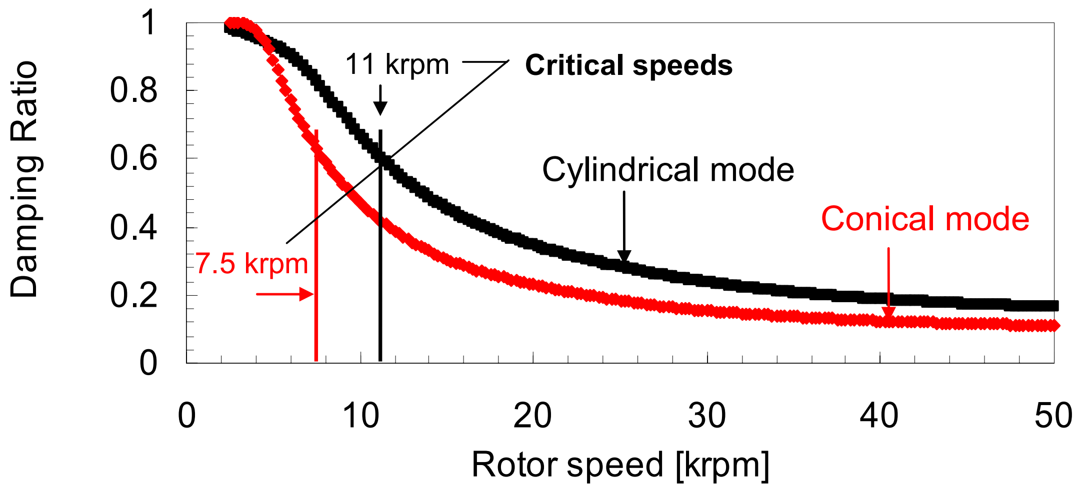

Figure 55 Predicted damping ratios for rotor – GFB system. GFBs with shims.

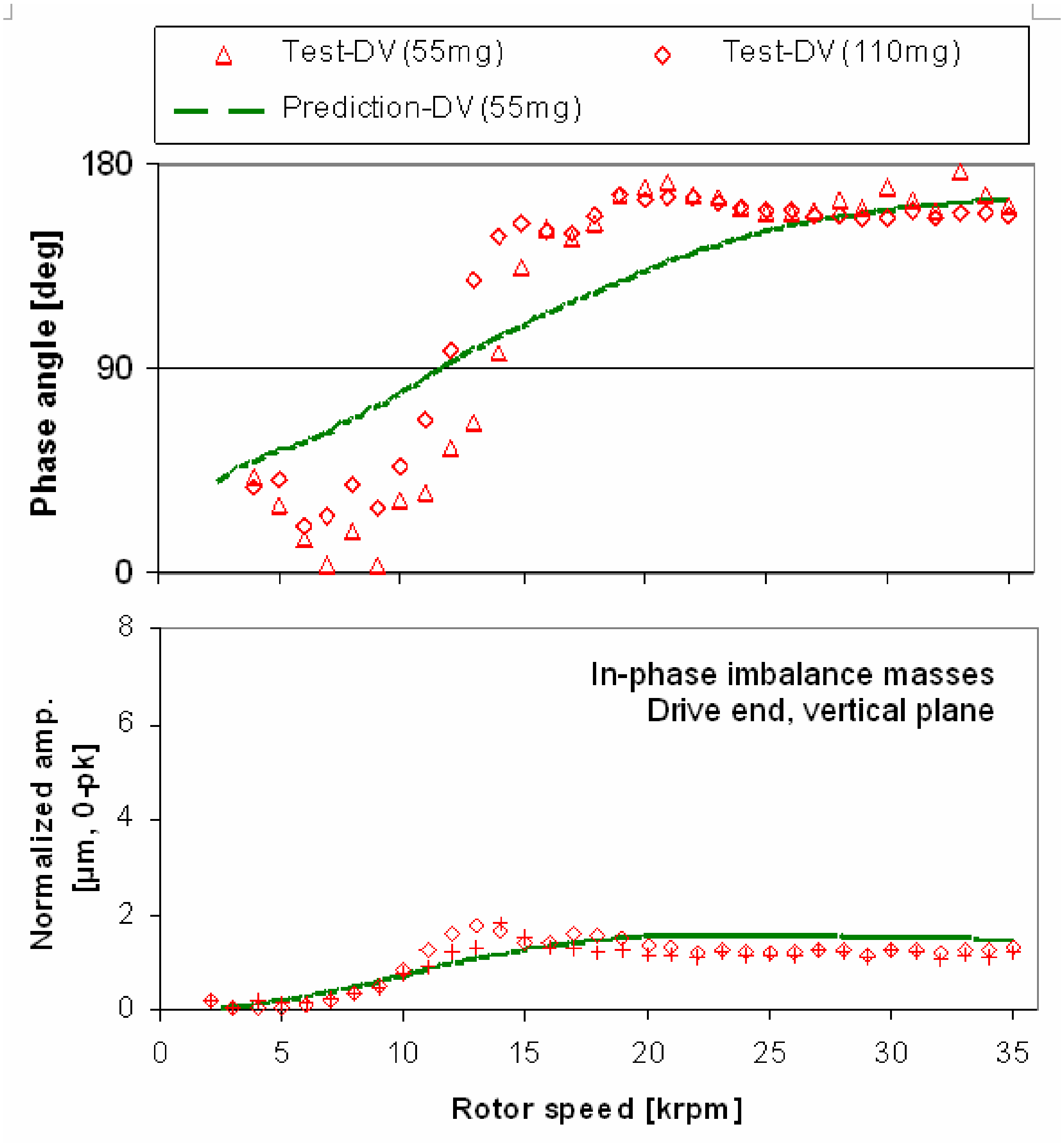

Figure 56a Phase angle and normalized rotor amplitude of synchronous response for increasing in-phase imbalance mass. Drive end, vertical plane. Predictions compared to test data.

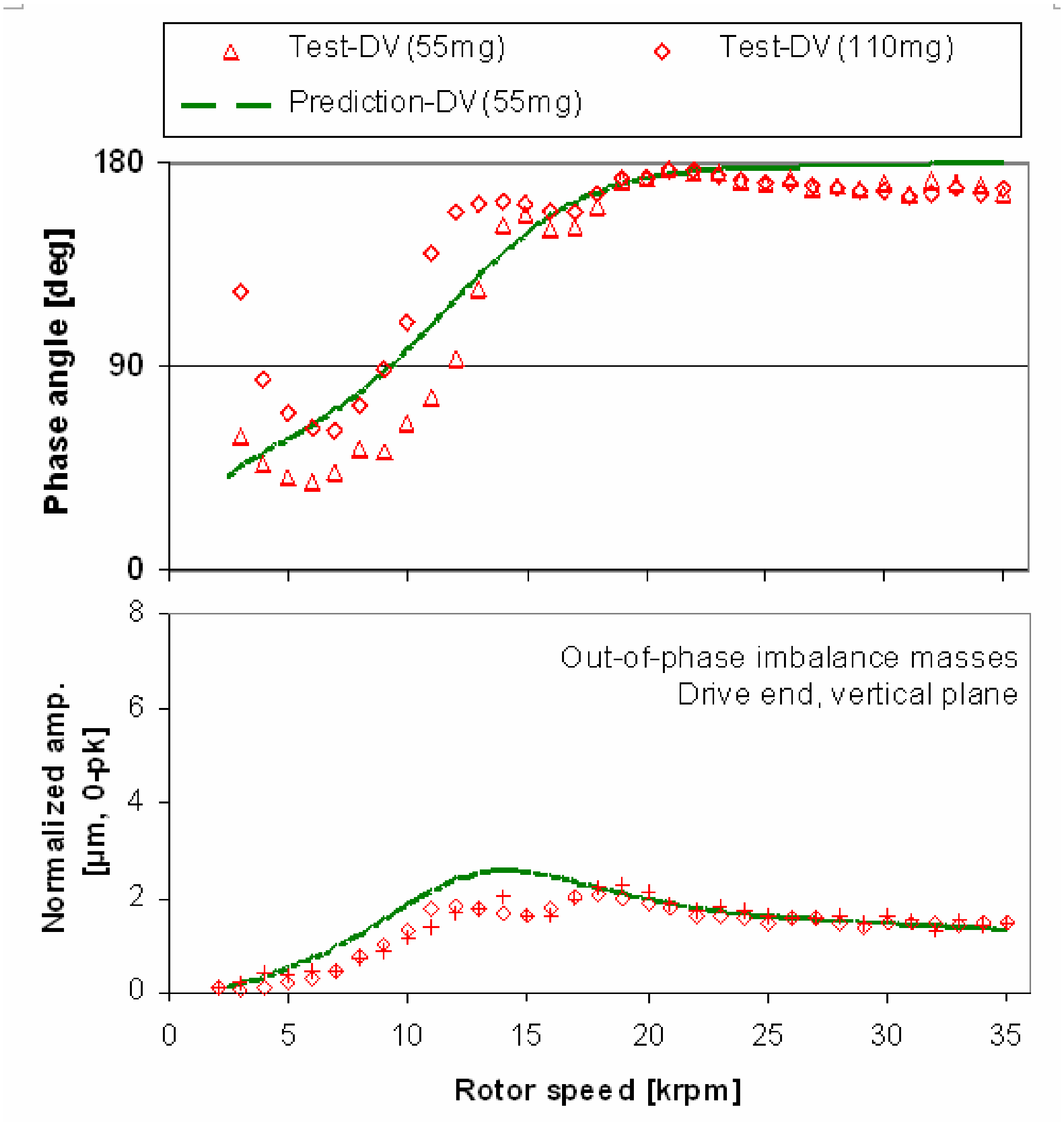

Figure 56b Phase angle and normalized rotor amplitude of synchronous response for increasing out-of-phase imbalance mass. Drive end, vertical plane. Predictions compared to test data.

Conclusions

GFBs are often pressurized at one end of the bearing to introduce cooling flow to prevent hot-spots in the GFB and extend its life. End gas pressurization, however, shows a profound effect on the performance of GFBs. The chapter first proposes a model of GFBs with side end pressurization and shows good agreement between predictions and test data. The extensive study models the test shimmed GFBs and compares the performance predictions to those of the original GFBs. The comparison reveals the unique rotordynamic performance of the shimmed GFBs. Moreover, all model predictions for the original and shimmed GFBs are in good agreement with test measurements. Thus, the present work provides design guidance of advanced rotor-GFB systems for oil-free micro turbomachinery.

The 2D FE model of the top foil supported on bump strip layers is coupled to the gas film model including the evolution of gas circumferential velocity as a function of the imposed side end pressure to model the test GFBs with side end pressurization. Model predictions show that the bearing direct stiffness and damping coefficients increase, but the difference in cross-coupled stiffnesses, K_{XY}-K_{YX}, decreases as the side end pressure increases. The analysis shows that a sufficiently high side end pressure effectively retards the evolution of the circumferential gas velocity, thus ensuring a stable rotor operation. The prediction shows good agreement with test data.

A model for GFBs with a machined mechanical preload predicts the performance of shimmed GFBs. A sinusoidal function approximately depicts the assembly radial clearance modified due to installation of three shims. A GFB with shims generates significant hydrodynamic pressures with peaks at the three shim locations, while the original GFB shows much lower pressures, irrespective of rotor speed. Note that although the GFB with shims enhances the bearing direct stiffness, a reduction in the minimum film thickness, in particular at low rotor speeds, may lead to earlier rotor touch-down, which is undesirable for top foil and shaft coating endurance.

A finite element (FE) model of the test rotor-GFB system is developed using XLTRC^2$_©$. A soft flexible coupling and connecting shaft aid to isolate the rotor –GFB system from the drive motor system. An eigenvalue analysis predicts the system critical speeds and damping ratios for the original and shimmed GFBs. In general, predicted rotor synchronous responses based on linearized bearing coefficients show good agreement with test measurements. Discrepancies between test data and predictions may be associated to uncertainties in the actual imbalance distribution.

CHAPTER VI

CONCLUSIONS

The dissertation details the modeling of bump-type gas foil bearings (GFBs) with side end pressurization and experimental validations. A computational analysis couples a 2D top foil model to a gas film flow model. Limited test data in the open literature and test data acquired from laboratory rotordynamic tests with small and moderately large imbalance masses validate the model predictions.

The major accomplishments and conclusions derived from this work are:

i) **Development of model for GFBs with side end pressurization.**

   a. The analysis models the top foil as a two dimensional (2D), finite element (FE) anisotropic shell structure supported on axially distributed linear springs.
   b. The analysis couples the 2D top foil model to the gas film flow model to predict the performance of GFBs without side end pressurization.
   c. The model predictions are validated to limited test data available in the open literature [32]. The predictions reproduce closely the experimentally observed circumferential wavy-like minimum film thickness profile.
   d. A unique model of a gas film flow in GFBs with side end pressurization is proposed. The gas film model includes the evolution of gas circumferential flow velocity along the axial plane due to the imposed side end pressure.
   e. Predicted direct stiffness and damping coefficients increase as the magnitude of side end pressure raises; while the difference in cross-coupled stiffnesses that is directly related to rotor-bearing system stability decreases.
   f. Side end pressurization delays the threshold speed of instability in a simple rotor-GFB model.

ii) **Experimental verification of the effect of side end pressurization on the rotordynamic performance of GFBs.**

  a. Rotordynamic response measurements were conducted during rotor speed run-up tests to 32 krpm for GFBs supplied with increasing end gas pressures to 2.8 bar (40 psig).
  b. Side end pressurization delays the onset rotor speed of subsynchronous motions. At a given rotor speed and for a sufficiently high feed pressure, rotor subsynchronous whirl motion disappears; i.e., the test system becomes rotordynamically stable.
  c. Test data are compared with model predictions of threshold speed of instability and whirl frequency ratio. The comparisons are in close agreement and validate the model of GFBs with side end pressurization.

iii) **Linear rotor response behavior with small and moderately large imbalance masses.**

  a. A series of rotor speed coastdown tests were conducted from 25 krpm at a side end pressure of 0.35 bar (5 psig) for in-phase and out-of-phase imbalance masses of small to large magnitudes.
  b. Test data show nearly uniform normalized amplitudes and phase angles with small and moderately large imbalance masses.
  c. A large imbalance mass causes an increase in normalized synchronous amplitudes around the rotor-bearing system critical speed and leads to a decrease in the onset rotor speed of subsynchronous whirl motions which appear at 1/3 whirl frequency ratio.
  d. Test data show that, with small and moderately large imbalance masses, test results evidence a linear rotor response behavior, i.e., characteristic of a linear system. However, a larger imbalance mass determinates a nonlinear rotor response.

iv) GFBs with mechanical preloads.

a. Inserting three metal shims under the bump strip layers and in contact with the bearing cartridge introduces mechanical preloads into the test GFBs.

b. Rotordynamic response measurements were conducted during rotor speed run-up tests to 50 krpm for the shimmed GFBs supplied with increasing end gas pressures to 4.1 bar (60 psig).

c. At a low side end pressure of 0.35 bar (5 psig), Shimmed GFBs increase the rotor-bearing system natural frequency due to an increase in bearing direct stiffness and aid to delay the threshold speed of instability where subsynchronous motions suddenly appear with large amplitudes. Increasing side end pressurization further helps to increase the threshold speed of instability.

d. The analysis models the shimmed GFBs, whose (unloaded) film clearance resembles a three lobe bearing.

e. Predictions show significantly larger hydrodynamic pressures for the shimmed GFBs when compared to those for the original GFBs. The shimmed GFBs operate with a smaller journal eccentricity and attitude angle than the original GFBs, and with increased direct stiffness and damping coefficients.

v) Test rotor – GFB system rotordynamics model.

a. A finite element rotordynamics model integrating the linearized GFB force coefficients is developed since, with small and moderately large imbalance masses, test results evidence a linear rotor-GFB system.

b. The model predictions of both rotor amplitudes and phase angles are compared to test data at a low side end pressure of 0.35 bar (5 psig) for in-phase and out-of-phase imbalance masses.

c. The comparison demonstrates an excellent correlation, thus validating the linearized GFB force coefficients for test rotor-GFB system with small and moderately large imbalance masses.

The dissertation brings significant original contributions toward the fundamental understanding of GFB rotordynamic performance.

Many GFB applications operate in high temperature environments. Therefore, further extensive analyses anchored to test data are required to improve the accuracy in performance prediction of GFBs operating under extreme temperatures. A thermal energy transport equation applied to a GFB will account for heat flux through the gas film and into the bearing structure.

The results of the GFB model, based on a linear analysis, are limited to small rotor imbalances. Recent Ref. [81] presents a GFB model predicting large amplitude subsynchronous motions at high rotor speeds due to the strong nonlinear (hardening) bump-foil structural stiffness characteristics. This research paves the way for future work.

REFERENCES

[1] Agrawal, G. L., 1997, "Foil Air/Gas Bearing Technology – an Overview," ASME Paper No. 97-GT-347.

[2] Heshmat, H., and Hermel, P., 1993, Compliant Foil Bearings Technology and Their Application to High Speed Turbomachinery. In *Thin Films in Tribology* (*19th Leeds–Lyon Symposium on Tribology*, Leeds, UK, 8–11 September 1992), ed. D. Dowson *et al.* (Elsevier Tribology Series, Vol. 25), Elsevier, Amsterdam, ISBN: 0-444-89789-5, pp. 559-575.

[3] Barnett, M. A., and Silver, A., 1970, "Application of Air Bearing to High-Speed Turbomachinery," SAE Paper No. 700720.

[4] Emerson, T. P., 1978, "The Application of Foil Air Bearing Turbomachinery in Aircraft Environmental Control Systems," ASME Paper No. 78-ENAS-18.

[5] Heshmat, C. A., Heshmat, H., 1995, "An Analysis of Gas-Lubricated, Multileaf Foil Journal Bearings with Backing Springs," J. Tribol., **117**, pp. 437-443.

[6] Braun, M. J., Choy, F. K., Dzodzo, M., and Hsu, J., 1996, "Two-Dimensional Dynamic Simulation of a Continuous Foil Bearing," Tribol. Intl., **29**(1), pp. 61-68.

[7] DellaCorte, C., and Valco, M. J., 2000, "Load Capacity Estimation of Foil Air Journal Bearings for Oil-Free Turbomachinery Applications," NASA/TM—2000-209782.

[8] Heshmat, H., 1994, "Advancements in the Performance of Aerodynamic Foil Journal Bearings: High Speed and Load Capacity," J. Tribol*.*, **116**, pp. 287-295.

[9] Heshmat, H., Walowit, J. A., and Pinkus, O., 1983, "Analysis of Gas-Lubricated Foil Journal Bearings," J. Lubr. Tech., **105**, pp. 647-655.

[10] San Andrés, L., 1995, "Turbulent Flow Foil Bearings for Cryogenic Applications," J. Tribol., **117**, pp. 185-195.

[11] Salehi, M., Heshmat, H., Walton, J. F., and Tomaszewski, M., 2007, "Operation of a Mesoscopic Gas Turbine Simulator at Speeds in Excess of 700,000 rpm on Foil Bearings," ASME J. Eng. Gas Turbines Power, **129**, pp. 170-176.

[12] TIAX LLC, 2004, “The Transit Bus Niche Market for Alternative Fuels - Module 8: Overview of Advanced Hybrid and Fuel Cell Bus Technologies,” Clean Cities Coordinator Toolkit, U.S. Department of Energy, http://www.eere.energy.gov/afdc/apps/toolkit/pdfs/mod08_zebs.pdf, accessed May 04, 2007.

[13] Kim, T.H., and L. San Andrés, 2006, “Limits for High Speed Operation of Gas Foil Bearings,” ASME J. Tribol., **128**, pp. 670-673.

[14] Chen, H. M., Howarth, R. Geren, B., Theilacker, J. C., and Soyars, W. M., 2000, “Application of Foil Bearings to Helium Turbocompressor,” *Proc. 30th Turbomachinery Symposium*, Texas A&M Univ., Houston, TX, pp. 103-113.

[15] Heshmat, H., Shapiro, W., and Gray, S., 1982, “Development of Foil Journal Bearings for High Load Capacity and High Speed Whirl Stability,” ASME J. Lubr. Tech., **104**, pp. 149-156.

[16] Bauman, S., 2005, “An Oil-Free Thrust Foil Bearing Facility Design Calibration, and Operation,” NASA/TM-2005-213568.

[17] San Andrés, L., Rubio, D., and Kim, T. H., 2007, “Rotordynamic Performance of a Rotor Supported on Bump Type Foil Gas Bearings: Experiments and Predictions,” ASME J. Eng. Gas Turbines and Power, **129**, pp. 850-857.

[18] Lund, J. W., 1968, “Calculation of Stiffness and Damping Properties of Gas Bearings,” ASME J. Lubr. Technol., **90**, pp. 793-803.

[19] Blok, H. and van Rossum, J. J., 1953, “The Foil Bearing – A New Departure In hydrodynamic Lubrication,” Lubr. Eng., December, pp. 316-320.

[20] Heshmat, H., Walowit, J. A., and Pinkus, O., 1983, “Analysis of Gas Lubricated Compliant Thrust Bearings,” J. Lubr. Tech., **105**, pp. 638-646.

[21] Peng, J.-P., and Carpino, M., 1993, “Calculation of Stiffness and Damping Coefficients for Elastically Supported Gas Foil Bearings,” J. Tribol., **115**, pp. 20-27.

[22] Peng, J.-P., and Carpino, M., 1994, “Coulomb Friction Damping Effects in Elastically Supported Gas Foil Bearings,” STLE Tribol. Trans., **37**(1), pp. 91-98.

[23] Iordanoff, I., 1999, “Analysis of an Aerodynamic Compliant Foil Thrust Bearing: Method for a Rapid Design,” J. Tribol., **121**, pp. 816-822.

[24] Heshmat, H., 1991, “Investigation of Foil Bearings for Use in High-Thrust Liquid Rocket Engines,” NASA CR-187099, April.

[25] Carpino, M., Medvetz, L. A., and Peng, J.-P., 1994, “Effects of Membrane Stresses in the Prediction of Foil Bearing Performance,” STLE Tribol. Trans., **37**, pp. 43-50.

[26] Carpino, M., Peng, J.-P., and Medvetz, L. A., 1994, “Misalignment In A Complete Shell Gas Foil Journal Bearing,” STLE Tribol. Trans., **37**, pp. 829-835.

[27] Carpino M., Talmage, G., 2003, “A Fully Coupled Finite Element Formulation for Elastically Supported Foil Journal Bearings,” STLE Tribol. Trans., **46**, pp. 560-565.

[28] Carpino M., Talmage, G., 2006, “Prediction of Rotor Dynamic Coefficients in Gas Lubricated Foil Journal Bearings with Corrugated Sub-Foils,” STLE Tribol. Trans., **49**, pp. 400-409.

[29] Heshmat, C. A., Xu, D. S., and Heshmat, H., 2000, “Analysis of Gas Lubricated Foil Thrust Bearings Using Coupled Finite Element and Finite Difference Methods,” ASME J. Tribol., **122,** pp. 199-204.

[30] Heshmat, H., Chen, H. M., and Walton, J. F., 2000, “On the Performance of Hybrid Foil-Magnetic Bearings,” ASME J. Eng. Gas Turbines Power, **122**, pp. 73-81.

[31] Kim, T. H., and San Andrés, L., 2005, “Heavily Loaded Gas Foil Bearings: A Model Anchored to Test Data,” ASME Paper No. GT2005-68486.

[32] Ruscitto, D., Mc Cormick, J., and Gray, S., 1978, “Hydrodynamic Air Lubricated Compliant Surface Bearing for an Automotive Gas Turbine Engine I-Journal Bearing Performance,” NASA CR-135368.

[33] Ku, C.-P. and Heshmat, H., 1993, “Compliant Foil Bearing Structural Stiffness Analysis – Part II: Experimental Investigation,” J. Tribol., **115**, pp. 364-369.

[34] Lee, D.–H., Kim, Y.-C., Kim, K.-W., 2004, “The Static and Dynamic Performance Analyses of Air Foil Journal Bearings for Various Bump Foil Stiffness,” J. KSTLE, **20**(5), pp. 245-251.

[35] Lee, Y.-B., Park, D.–J., and Kim, C.–H., 2006, "Numerical Analysis for Bump Foil Journal Bearing Considering Top Foil Effect and Experimental Investigation," Paper-ID 229, *7th IFToMM-Conference on Rotor Dynamics*, Vienna, Austria.

[36] Peng, Z.-C., and Khonsari, M. M., 2004, "On the Limiting Load-Carrying Capacity of Foil Bearings," ASME J. Tribol., **126**, pp. 817-818.

[37] Radil, K., Howard, S., and Dykas, B., 2002, "The Role of Radial Clearance on the Performance of Foil Air Bearings," STLE Tribol. Trans., **45**, pp. 485-490.

[38] Dykas, B., and Howard, S. A., 2004, "Journal Design Consideration for Turbomachine Shaft Supported on Foil Air Bearings," STLE Tribol. Trans. **47**, pp. 508-516.

[39] Salehi, M., Swanson, E., and Heshmat, H., 2001, "Thermal Features of Compliant Foil Bearings – Theory and Experiments," ASME J. Tribol., **123**, pp. 566-571.

[40] Pinkus, O. and Bupara, S. S., 1979, "Adiabatic Solution for Finite Journal Bearings," ASME J. Lubr. Technol., **101**, pp. 492-496.

[41] Peng, Z-C., and Khonsari, M. M., 2006, "A Thermohydrodynamic Analysis of Foil Journal Bearings," ASME J. Tribol., **128**, pp. 534-540.

[42] Radil, K., and Zeszotek, M., 2004, "An Experimental Investigation into the Temperature Profiles of a Compliant Foil Air Bearing," STLE Tribol. Trans., **47**, pp.470-479.

[43] Ku, C.-P. and Heshmat, H., 1993, "Compliant Foil Bearing Structural Stiffness Analysis – Part I: Theoretical Model Including Strip and Variable Bump Foil Geometry," ASME J. Tribol., **114,** pp. 394-400.

[44] Ku, C.-P, and Heshmat, H., 1994, "Structural Stiffness and Coulomb Damping in Compliant Foil Journal Bearing: Theoretical Considerations," STLE Tribol. Trans., **37**(3), pp. 525-533.

[45] Ku, C.-P, and Heshmat, H., 1994, "Structural Stiffness and Coulomb Damping in Compliant Foil Journal Bearing: Parametric Studies," STLE Tribol. Trans., **37**(3), pp. 455-462.

[46] Heshmat, H., and Ku, C.-P., 1994, “Structural Damping of Self-Acting Compliant Foil Journal Bearings,” ASME J. Tribol., **116**(1), pp. 76-82.

[47] Salehi, M., Heshmat, H., and Walton, J., 2003, “On the Frictional Damping Characterization of Compliant Bump Foils,” ASME J. Tribol., **125**(4), pp. 804-813.

[48] Rubio, D., and San Andrés, L., 2006, “Bump-Type Foil Bearing Structural Stiffness: Experiments and Predictions,” ASME J. Eng. Gas Turbines Power, **128**(3), pp. 653-660.

[49] Rubio, D., and San Andrés, L., 2007, “Structural Stiffness, Dry Friction Coefficient, and Equivalent Viscous Damping in a Bump-Type Foil Gas Bearing,” ASME J. Eng. Gas Turbines Power, **129**, pp. 494-502.

[50] Heshmat, H., 2000, “Operation of Foil Bearing Beyond the Bending Critical Mode,” ASME J. Tribol., **122**(1), pp. 192-198.

[51] Lee, Y. B., Kim, T. H., Kim, C. H., Lee, N. S., and Choi, D. H., 2004. “Dynamic Characteristics of a Flexible Rotor System Supported by a Viscoelastic Foil Bearing (VEFB),” Tribol. Intl., **37**, pp. 679-687.

[52] Lee, Y. B., Kim, T. H., Kim, C. H., Lee, N. S., and Choi, D. H., 2003, “Unbalance Response of a Super-Critical Rotor Supported by Foil Bearings – Comparison with Test Results,” STLE Tribol. Trans., **47**(1), pp. 54-60.

[53] Lee, Y. B., Kim, T. H., Kim, C. H., and Lee, N. S., 2003, “Suppression of Subsynchronous Vibrations Due to Aerodynamic Response to Surge in a Two-Stage Centrifugal Compressor with Air Foil Bearings,” STLE Tribol. Trans., **46**, pp. 428-434.

[54] DellaCorte, C., Zaldana, A., and Radil, K., 2003, “A System Approach to the Solid Lubrication of Foil Air Bearing for Oil-Free Turbomachinery,” ASME J. Tribol., **126**(1), pp. 200-207.

[55] Radil, K. C., and DellaCorte, C., 2000, "The Effect of Journal Roughness and Foil Coatings on the Performance of Heavily Loaded Foil Air Bearings," NASA/TM—2000-210941.

[56] Howard, S., 1999, "Preliminary Development of Characterization Method for Compliant Air Bearings," STLE Tribol. Trans., **42**(4), pp. 789-794.

[57] Howard, S., DellaCorte, C., Valco, M.-J., Prahl, J.-M., and Heshmat, H., 2001, "Steady-State Stiffness of Foil Air Journal Bearings at Elevated Temperatures," STLE Tribol. Trans., **44**(3), pp. 489-493.

[58] Howard, S., DellaCorte, C., Valco, M.-J., Prahl, J.-M., and Heshmat, H., 2001, "Dynamic Stiffness and Damping Characteristics of a High-Temperature Air Foil Journal Bearing," STLE Tribol. Trans., **44**(4), pp. 657-663.

[59] DellaCorte, C., 1997, "A New Foil Air Bearing Test Rig for Use to 700 ºC and 70,000 rpm," NASA TM-107405.

[60] DellaCorte, C., Valco, M. J., Radil, K. C., and Heshmat, H., 1999, "Performance and Durability of High Temperature Foil Air Bearings for Oil-Free Turbomachinery," NASA/TM-1999-209187.

[61] DellaCorte, C., 1998, "The Evaluation of a Modified Chrome Oxide Based High Temperature Solid Lubricant Coating for Foil Gas Bearings," NASA/TM-1998-208660.

[62] Stanford, M. K, DellaCorte, C., and Eylon, D., 2002, "Particle Morphology Effects on Flow Characteristics of PS304 Plasma Spray Coating Feedstock Powder Blend," NASA/TM-2002-211206.

[63] DellaCorte, C., 2002, "The Effects of Substrate Material and Thermal Processing Atmosphere on the Strength of PS304: A High Temperature Solid Lubricant Coating," NASA/TM-2002-211483.

[64] Stanford, M. K and DellaCorte, C., 2002, "Effects of Humidity on the Flow Characteristics of PS304 Plasma Spray Feedstock Power Blend," NASA/TM-2002-211549.

[65] Lubell, D., DellaCorte, C. and Stanford, M., 2006, "Test Evolution and Oil-Free Engine Experience of a High Temperature Foil Air Bearing Coating," ASME Paper No. GT2006-90572.

[66] Mohawk Innovative Technology, Inc., 2004, “Foil Gas Bearings Enable Oil-Free Compressor Breakthrough,” Newsletter Vol. 19, http://www.miti.cc/newsletters/19_ foil_gas _bearings_enable_oilfree_compressor_breakthrough.pdf, accessed May 04, 2007.

[67] Allaire, P. E., Lee, C. C., and Gunter, E. J., 1978, “Dynamics of Short Eccentric Plain Seals with High Axial Reynolds Numbers,” J Spacecraft and Rockets, **15**, pp. 341-347.

[68] Childs, D., 1993, *Turbomachinery Rotordynamics – Phenomena, Modeling, & Analysis*, John Wiley & Sons, New York, pp. 248–274.

[69] Black, H. F., Allaire, P. E., and Barrett, L. E., 1981, “Inlet Flow Swirl in Short Turbulent Annular Seal Dynamics,” *Proc. 9th Intl. Conf. in Fluid Sealing*, BHRA Fluid Engineering, Leeuwenborst, The Netherlands, pp. 141-152.

[70] Reddy, J. N., 1993, *An Introduction to the Finite Element Method*, McGraw-Hill, Singapore, Chapters 4, 12.

[71] Timoshenko, S. P., and Woinowsky-Krieger, S., 1959, *Theory of Plates and Shells*, McGraw-Hill, Singapore, pp. 507-514.

[72] San Andrés, L., and Kim, T. H., 2006, “Computational Analysis of Gas Foil Bearings Integrating 1D and 2D Finite Element Models for Top Foil,” Technical Report No TRC-B&C-1-06, Texas A&M Univ., College Station, TX.

[73] *Numerical Recipes in Fortran 77: The Art of Scientific Computing*, ISBN 0-521-43064-X, Cambridge University Press, pp. 89-91.

[74] Faria, M., and San Andrés, L., 2000, “On the Numerical Modeling of High Speed Hydrodynamic Gas Bearing,” J. Tribol., **122**, pp. 124-130.

[75] Walowit, J., Murray, S. F., McCabe, J., Arwas, E. B., and Moyer, T., 1973, “Gas Lubricated Foil Bearing Technology Development for Propulsion and Power System,” Technical Report No. AFAPL-TR-73-92.

[76] Ku, C-P. R., 1993, "An Experimental and Theoretical Study of the Dynamic Structural Stiffness in Compliant Foil Journal Bearings," *ASME 14th Biennial*

Conference on Mechanical Vibration and Noise, Albuquerque, NM, DE-Vol. 63, Vibration of Mechanical Systems and the History of Mechanical Design, pp. 83-88.

[77] Ku, C-P. R., 1993, "Dynamic Structural Properties in Compliant Foil Thrust Bearings – Comparisons between Experimental and Theoretical Results," ASME J. Tribol., **116**, pp. 70-75.

[78] San Andrés, L., and Kim, T. H., 2006, "Further Imbalance Response Measurements of Rotor Supported on Bump-Type Gas Foil Bearings: Operation to 50 krpm," Technical Report No. TRC-B&C-1-06, Texas A&M Univ., College Station, TX.

[79] Descriptions of Proximity Probes, Bently Nevada ™ Asset Condition Monitoring, http://www.bently.com/prod/products/transducers/proxprobes.htm, accessed Aug. 08, 2007.

[80] Ginsberg, J. H., 2001, *Mechanical and Structural Vibration – Theory and Application*, John Wiley & Sons, New York, pp. 135–139.

[81] San Andrés, L., and Kim, T. H., 2007, "Issues on Instability and Forced Nonlinearity in Gas Foil Bearing Supported Rotors," *43rd AIAA/ASME/SAE/ASEE Joint Propulsion Conference & Exhibit*, AIAA Paper No. AIAA-2007-5094, Cincinnati, OH.

APPENDIX A

GOVERNING EQUATIONS OF AN ANISOTROPIC SHEAR DEFORMABLE PLATE

The present analysis retakes the anisotropic, shear deformable plate model based on first-order shear deformation theory. As given in [70], the governing equations are

$$\frac{\partial M_x}{\partial x}+\frac{\partial M_{zx}}{\partial z}-Q_x=0 \quad ; \quad \frac{\partial M_{zx}}{\partial x}+\frac{\partial M_z}{\partial z}-Q_z=0 \quad ; \quad \frac{\partial Q_x}{\partial x}+\frac{\partial Q_z}{\partial z}-q=0 \qquad \text{(A.1)}$$

where

$$M_z=D_{33}\frac{\partial \phi_z}{\partial z}+D_{13}\frac{\partial \phi_x}{\partial x} \ ; \ M_x=D_{11}\frac{\partial \phi_x}{\partial x}+D_{13}\frac{\partial \phi_z}{\partial z} \ ; \ M_{xz}=D_{66}\left(\frac{\partial \phi_x}{\partial z}+\frac{\partial \phi_z}{\partial x}\right) \ ;$$

$$Q_x=A_{55}\left(\phi_x+\frac{\partial v}{\partial x}\right) \ ; \ Q_z=A_{44}\left(\phi_z+\frac{\partial v}{\partial z}\right) \qquad \text{(A.2)}$$

and

$$D_{11}=\frac{E_{t1}h_t^3}{12\left(1-\nu_{t13}\nu_{t31}\right)} \ ; \ D_{33}=\frac{E_{t3}h_t^3}{12\left(1-\nu_{t13}\nu_{t31}\right)} \ ; \ D_{13}=\frac{\nu_{t13}E_{t3}h_t^3}{12\left(1-\nu_{t13}\nu_{t31}\right)} \ ;$$

$$D_{66}=\frac{E_{t13}h_t^3}{24\left(1-\nu_{t13}\right)} \ ; \ A_{44}=k_t\frac{E_{t32}h_t}{2\left(1-\nu_{t32}\right)} \ ; \ A_{55}=k_t\frac{E_{t12}h_t}{2\left(1-\nu_{t12}\right)} \qquad \text{(A.3)}$$

ϕ_x and ϕ_z in Eq. (A.2) denote rotation angles about the z and x axes, respectively. h_t, E_{tij}, $\nu_{tij,\, i,j=1,2,3}$ in Eq. (A.3) represent the shell thickness, anisotropic elastic modulii and Poisson's ratios, respectively. k_t (=5/6) is a shear correction coefficient, introduced to account for the discrepancy between the distribution of transverse shear stresses of the first-order theory and actual distribution [70]. Note that, in Eqs. (A.1–A.3), neglecting the deflections (v, ϕ_z) along the z axis leads to the governing equations for Timoshenko's beam theory [71].

Reference [70] details the week form of Eqs. (A.1–A.3) when integrated over a two-dimensional finite element domain.

APPENDIX B

NORMALIZED AMPLITUDE AND PHASE ANGLE OF SYNCHRONOUS RESPONSE AT FREE END BEARING, VERTICAL PLANE: ORIGINAL GFBS

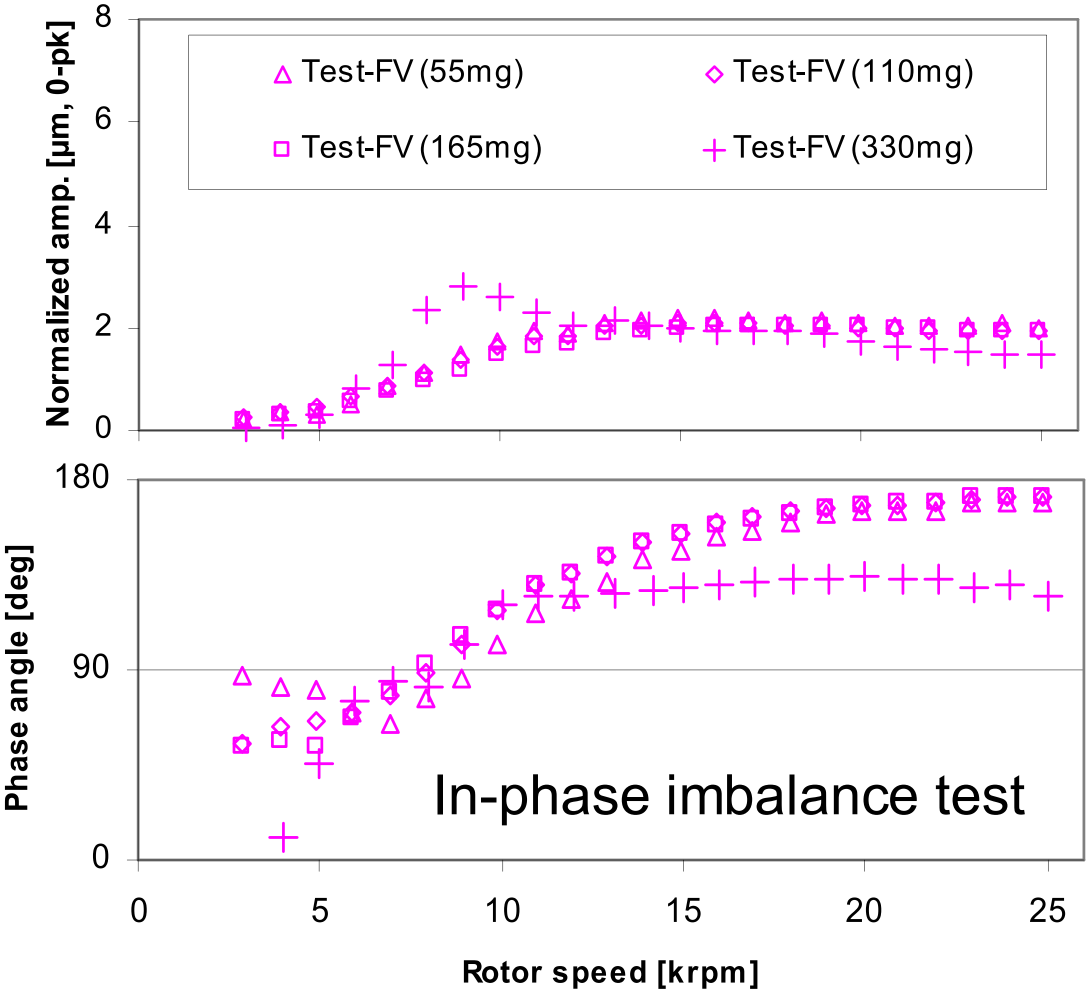

Figure B1a Influence of large imbalance mass on normalized amplitude and phase angle of synchronous response. In-phase imbalance masses of 55mg, 110mg, 165mg, and 330mg. Measurement at free end bearing, vertical plane with baseline subtraction. Side end gauge pressure at 0.34 bar (5 psig). Original GFBs.

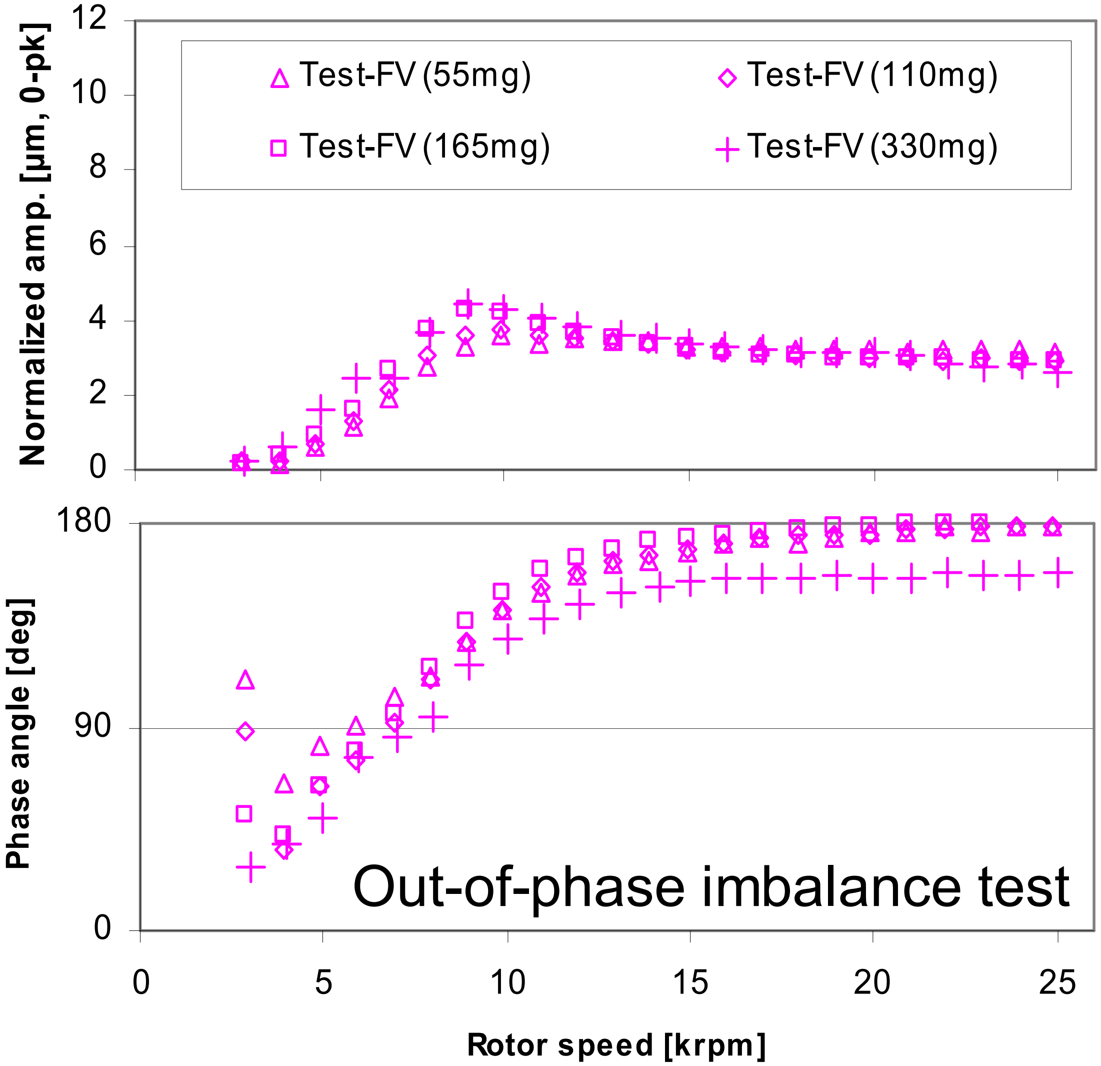

Figure B1b Influence of large imbalance mass on normalized amplitude and phase angle of synchronous response. Out-of-phase imbalance masses of 55mg, 110mg, 165mg, and 330mg. Measurement at free end bearing, vertical plane with baseline subtraction. Side end gauge pressure at 0.34 bar (5 psig). Original GFBs.

APPENDIX C

NORMALIZED AMPLITUDE AND PHASE ANGLE OF SYNCHRONOUS RESPONSE AT DRIVE END BEARING, VERTICAL PLANE FOR INCREASING SIDE END PRESSURES: ORIGINAL GFBS

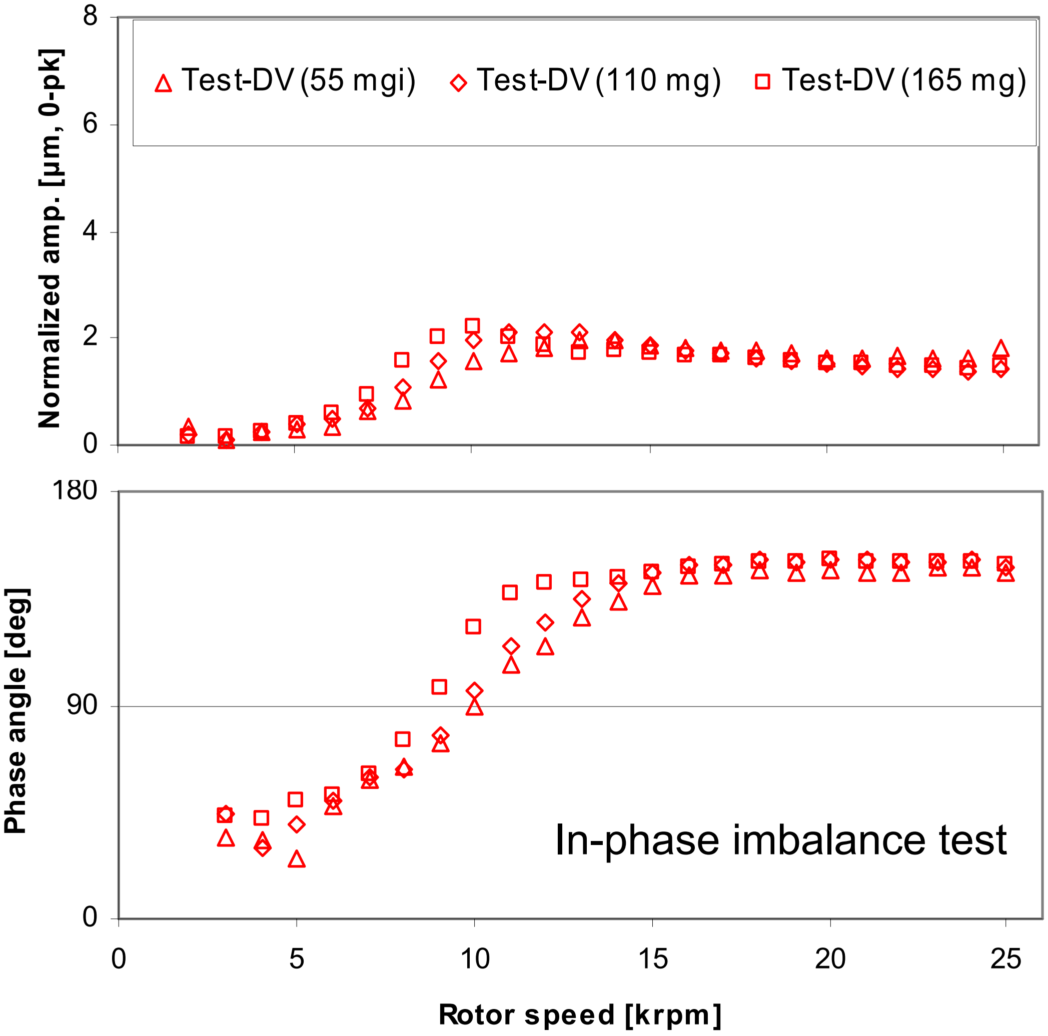

Figure C1a Normalized amplitude and phase angle of synchronous response for side end gauge pressure at 1.4 bar (20 psig). In-phase imbalance masses of 55mg, 110mg, and 165mg. Measurement at drive end bearing, vertical plane with baseline subtraction. Original GFBs.

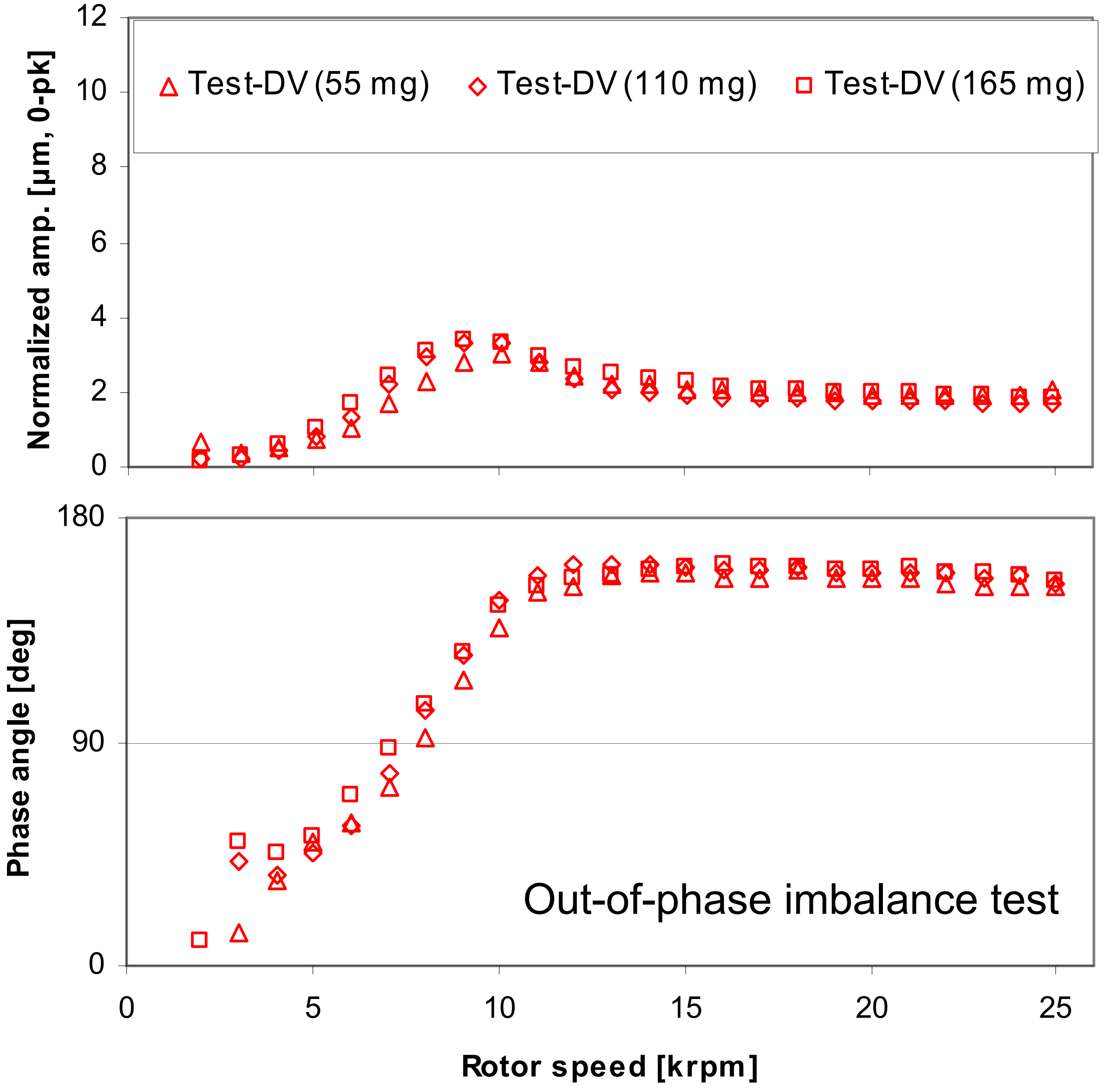

Figure C1b Normalized amplitude and phase angle of synchronous response for side end gauge pressure at 1.4 bar (20 psig). Out-of-phase imbalance masses of 55mg, 110mg, and 165mg. Measurement at drive end bearing, vertical plane with baseline subtraction. Original GFBs.

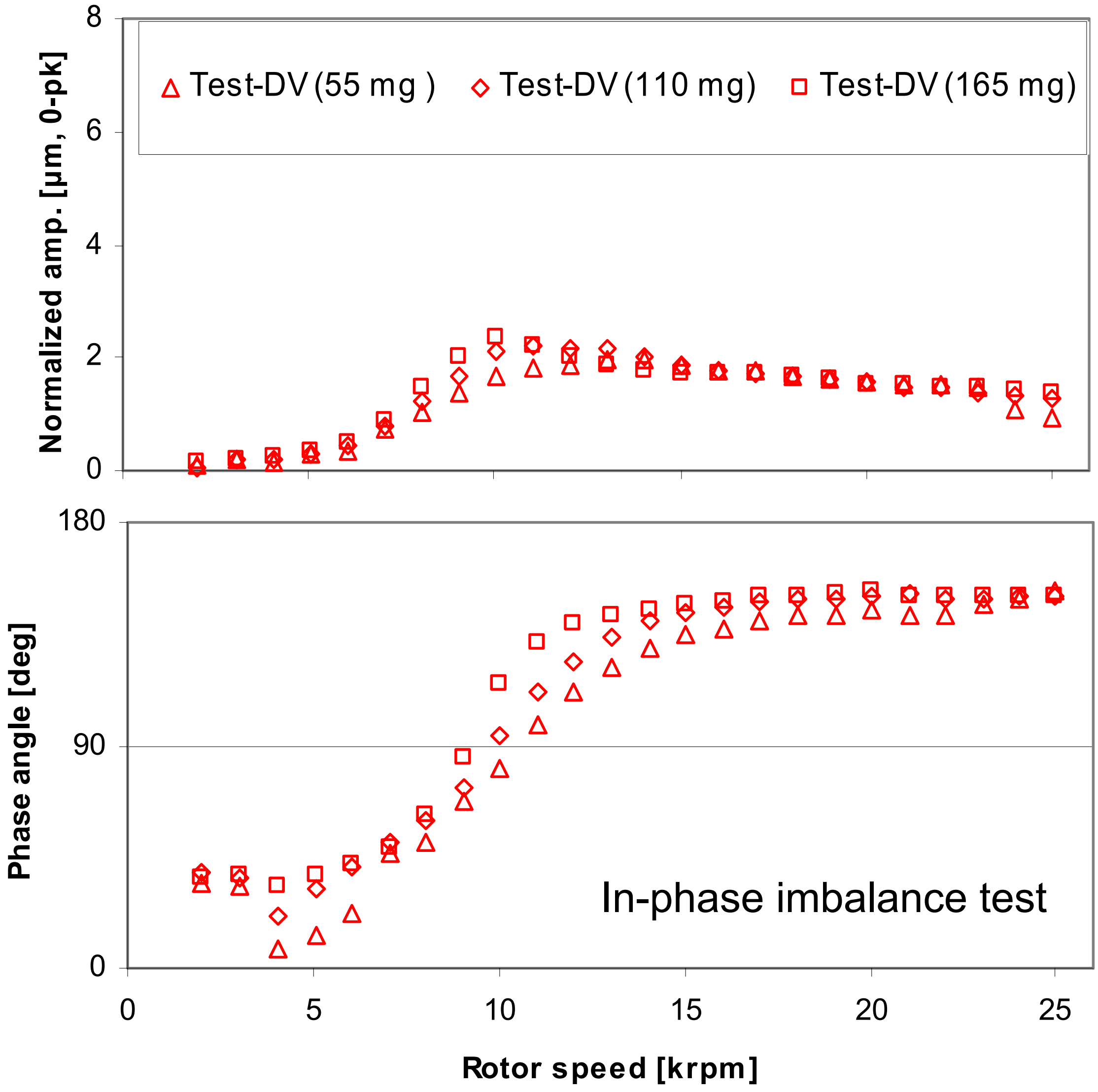

Figure C2a Normalized amplitude and phase angle of synchronous response for side end gauge pressure at 2.8 bar (40 psig). In-phase imbalance masses of 55mg, 110mg, and 165mg. Measurement at drive end bearing, vertical plane with baseline subtraction. Original GFBs.

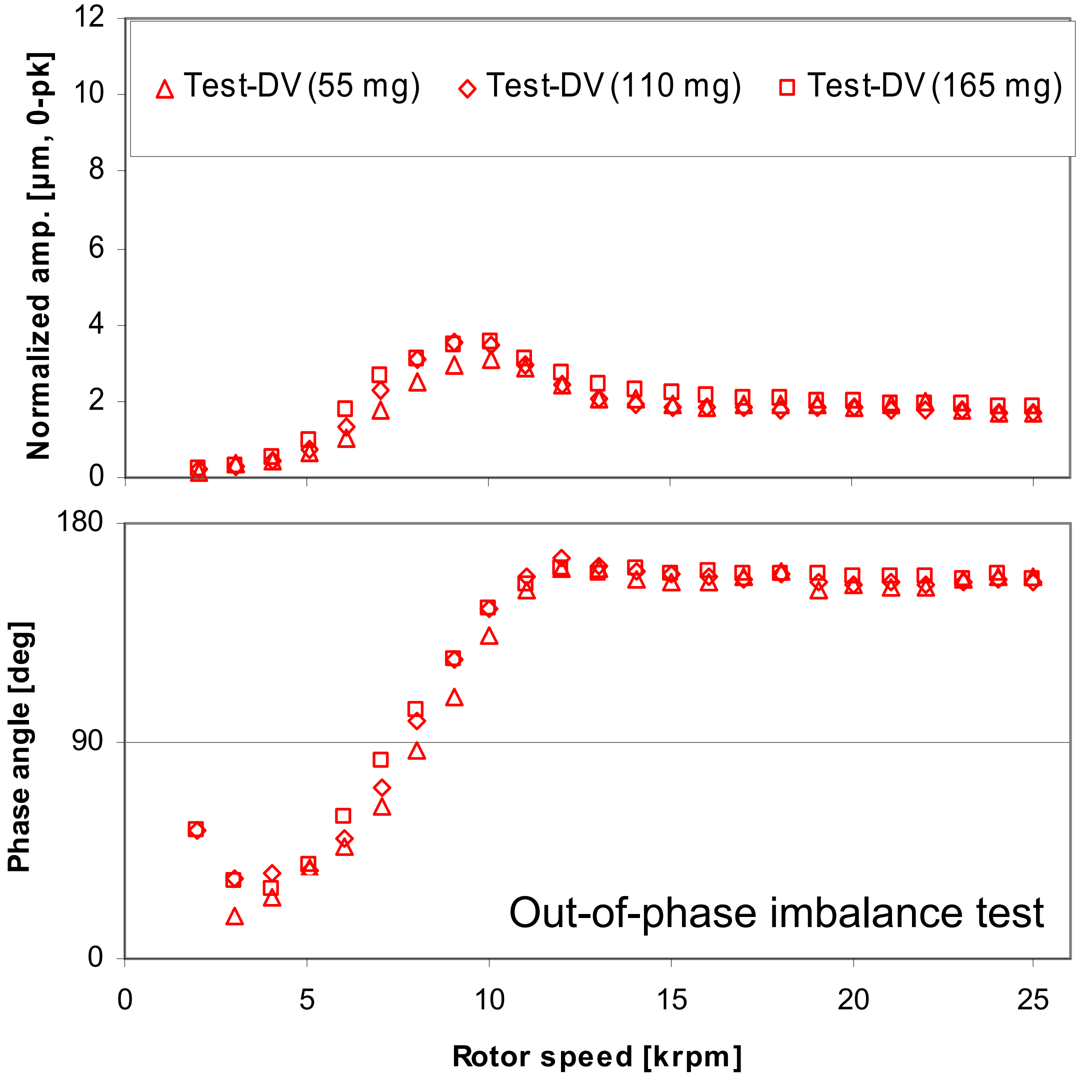

Figure C2b Normalized amplitude and phase angle of synchronous response for side end gauge pressure at 2.8 bar (40 psig). Out-of-phase imbalance masses of 55mg, 110mg, and 165mg. Measurement at drive end bearing, vertical plane with baseline subtraction. Original GFBs.

APPENDIX D

ROTOR SPEED-UP RESPONSE FROM 10 KRPM TO 50 KRPM FOR GFBS WITH SHIMS: BASELINE IMBALANCE CONDITION

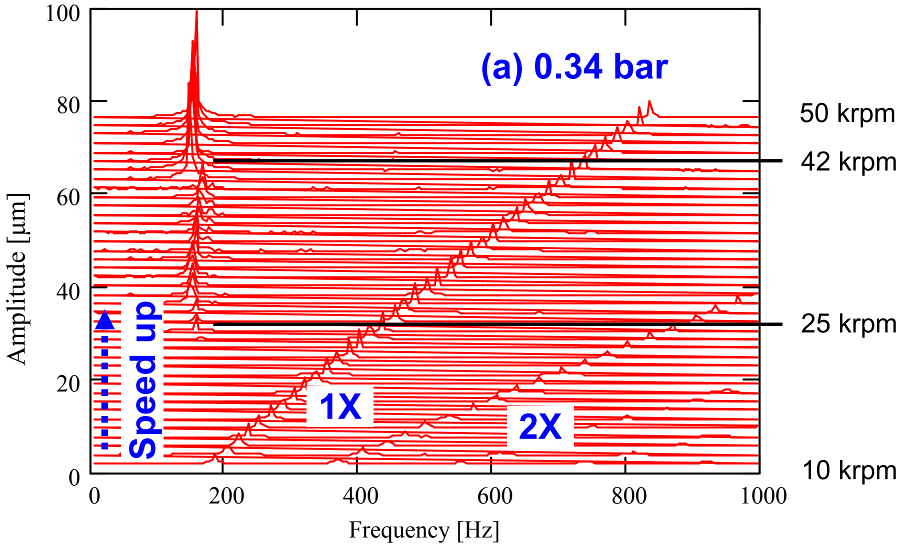

(a) Waterfall

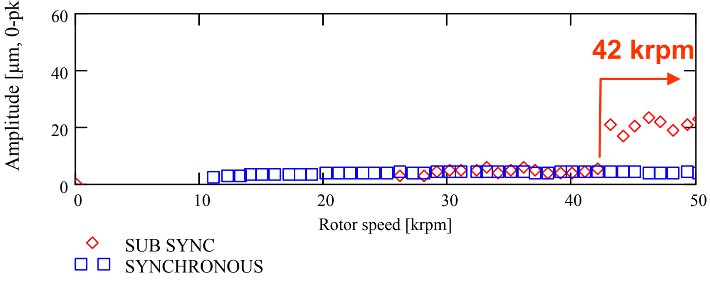

(b) Synchronous and subsynchronous components

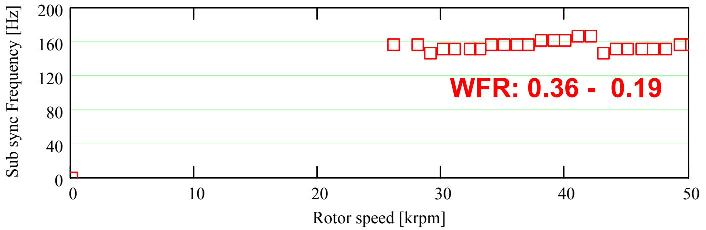

(c) Subsynchronous whirl frequency

Figure D1 Rotor speed-up response from 10 krpm to 50 krpm. Baseline imbalance condition, side end air pressure of 0.34 bar (5 psig). Measurement at rotor free end, vertical plane. GFBs with shims.

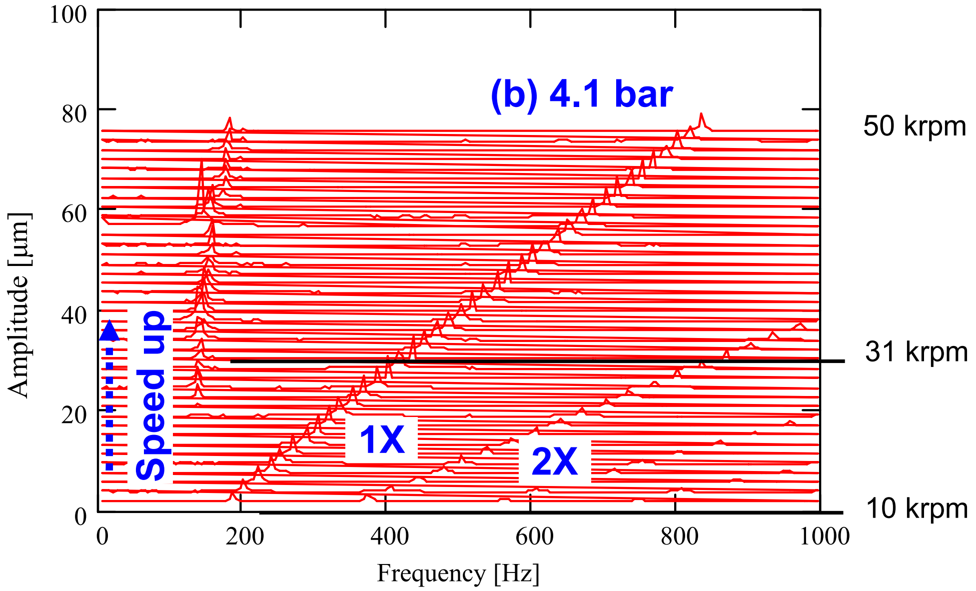

(a) Waterfall

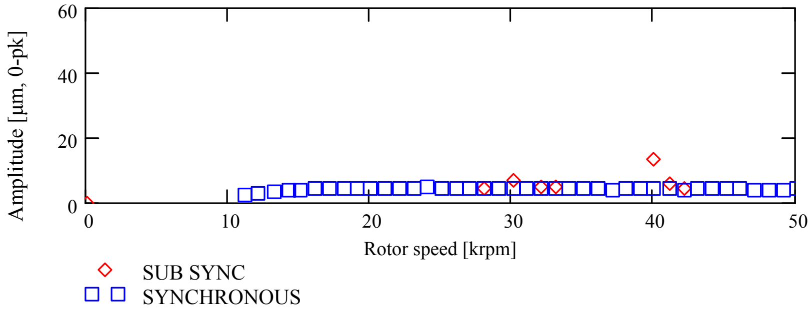

(b) Synchronous and subsynchronous components

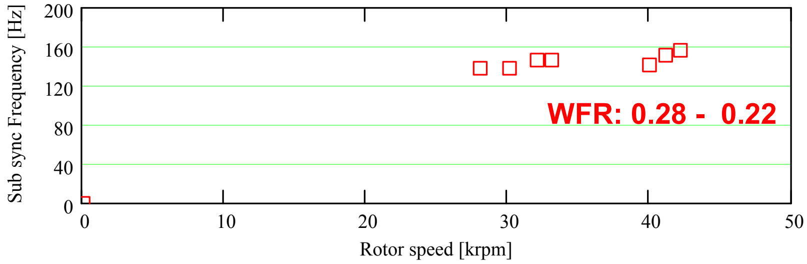

(c) Subsynchronous whirl frequency

Figure D2 Rotor speed-up response from 10 krpm to 50 krpm. Baseline imbalance condition, side end air pressure of 4.1 bar (60 psig). Measurement at rotor free end, vertical plane. GFBs with shims.

APPENDIX E

NORMALIZED AMPLITUDE AND PHASE ANGLE OF SYNCHRONOUS RESPONSE AT FREE END BEARING, VERTICAL PLANE: GFBS WITH SHIMS

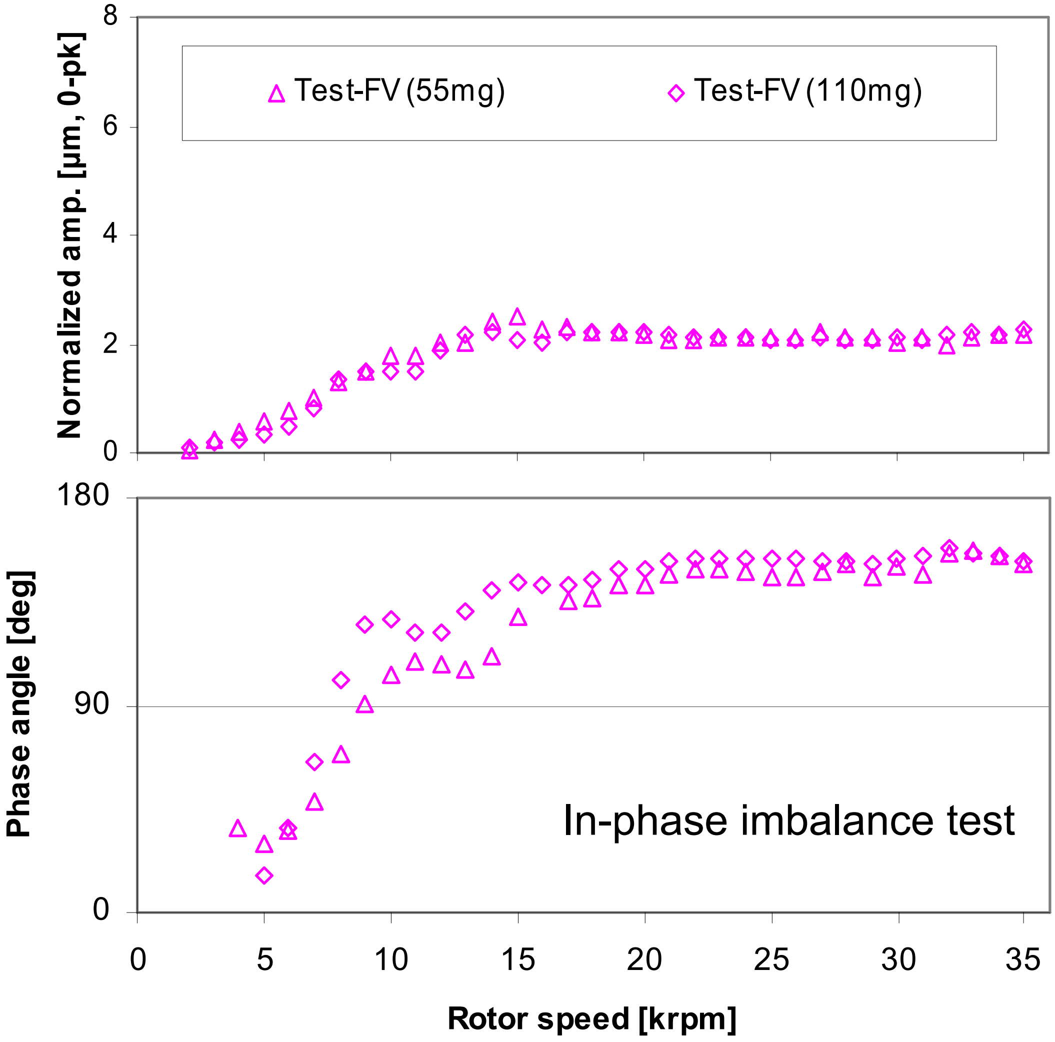

Figure E1a Normalized amplitude of synchronous response and phase angle for in-phase imbalance masses of 55mg and 110mg. Measurements at free end bearing, vertical plane with baseline subtraction. Side end gauge pressure at 0.34 bar (5 psig). GFBs with shims.

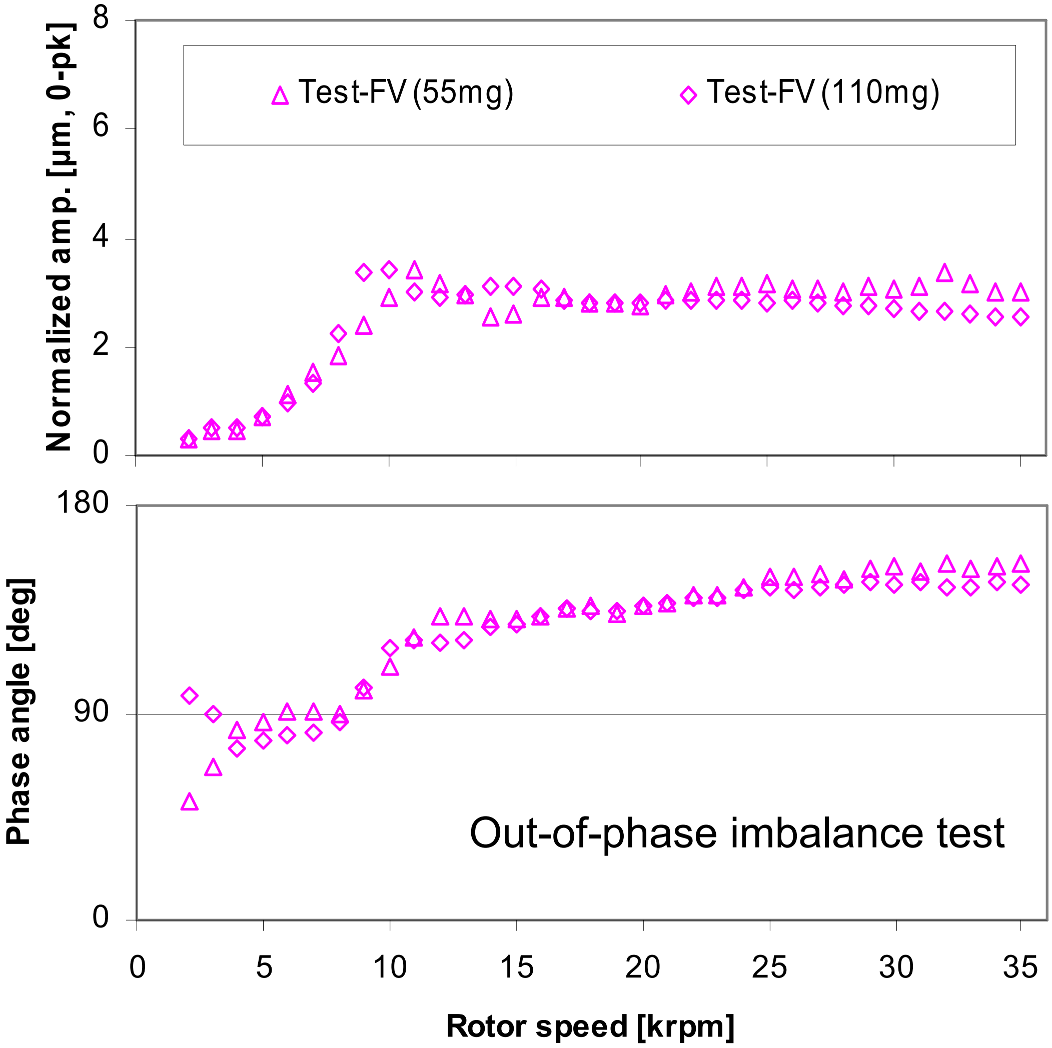

Figure E1b Normalized amplitude of synchronous response and phase angle for out-of-phase imbalance masses of 55mg and 110mg. Measurements at free end bearing, vertical plane with baseline subtraction. Side end gauge pressure at 0.34 bar (5 psig). GFBs with shims.

APPENDIX F

ROTORDYNAMIC PARAMETERS OF ROTOR AND GFBS WITH SHIMS

Table F1 Estimated rotordynamic parameters of the rotor-GFB system obtained from synchronous coastdown responses. Side end air gauge pressure at 0.34 bar (5 psig). GFB with shims.

Location		Imbalance Condition	Natural frequency, $\omega_n \times (30/\pi)$ [rpm]	Critical Speed, $\omega_{cr} \times (30/\pi)$ [rpm]	Effective stiffness, K_{eff} [MN/m]	Damping ratio, ξ	Effective damping, C_{eff} [N-s/m]
Imbalance mass (55 mg) , u_{DE} = 1.26 μm and u_{FE} = 2.34 μm							
Drive end	X_{DE}	in phase	13,800	14,000	1.38	0.12	227
		out of phase	12,000	19,000	1.04	0.55	909
	Y_{DE}	in phase	15,500	16,000	1.74	0.18	376
		out of phase	13,500	15,000	1.32	0.31	575
Free End	X_{FE}	in phase	9,000	15,000	0.32	0.57	384
		out of phase	8,000	11,000	0.25	0.49	293
	Y_{FE}	in phase	11,000	16,000	0.48	0.51	426
		out of phase	11,500	13,000	0.52	0.33	286
Imbalance mass (110 mg) , u_{DE} = 2.52 μm and u_{FE} = 4.67 μm							
Drive end	X_{DE}	in phase	12,000	13,000	1.04	0.27	451
		out of phase	9,000	18,000	0.59	0.61	762
	Y_{DE}	in phase	14,500	14,000	1.52	-	-
		out of phase	11,500	13,000	0.96	0.33	524
Free End	X_{FE}	in phase	7,500	18,000	0.22	0.64	363
		out of phase	8,000	10,000	0.25	0.42	256
	Y_{FE}	in phase	9,800	16,000	0.38	0.56	413
		out of phase	10,800	11,000	0.46	0.13	109

X: vertical, Y: horizontal. ω_n and ω_{cr} are determined from synchronous rotor responses with uncertainty of ±500 rpm.

Rotor masses supported on the drive end and free end bearings are 0.66 kg and 0.36 kg, respectively.

APPENDIX G

ESTIMATION OF RADIAL CLEARANCES IN ORIGINAL GFBS AND STIFFNESS COEFFICIENT OF THE FLEXIBLE COUPLING

A series of static load – deflection tests aids to estimate the nominal radial clearances in the test GFBs. Figure G1 shows the schematic view of the test setup. The test rotor is mounted on a lathe, and the drive and free end GFBs are installed on the rotor at the same axial locations as in the rotordynamic test rig. A strain gauge type load cell is mounted on the lathe table and connected to the test GFBs through an adapter. Moving the lathe table forward and backward provides compression and tension forces, respectively, to the GFBs through the adapter. The load cell and an eddy current displacement sensor measure the applied static load and the bearing displacement, respectively. The orientation of the spot weld in the test GFB is 45 º away from the load direction.

With the test GFB resting on the test rotor, moving forward (1) the lathe table incrementally increases the static load on the bearing at 45 º from the spot weld, and then moving it backward (2) decreases the load. When the recorded load becomes zero, moving the table backward (2) incrementally increases the load on the bearing at -135 º from the spot weld, and then moving it forward (1) reduces the load. This procedure is repeated twice for both the drive and free end GFBs, and the static load and bearing displacement are all recorded. Table G1 provides lathe table moving directions for each loading and unloading tests. Figure G2 illustrates the recorded bearing displacement versus static load.

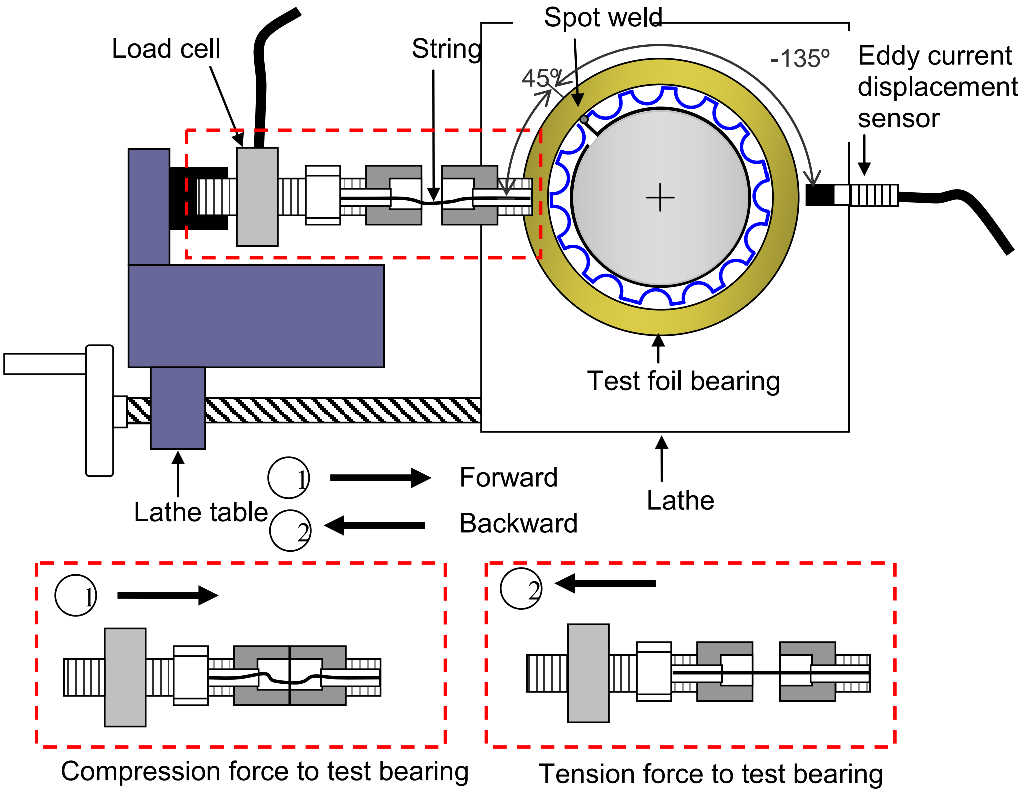

Figure G1 Schematic view of a test setup for GFB load-deflection tests.

Table G1 Load – deflection test procedure and test numbers.

Test No.	Table moving direction	Loading / Unloading
Test 1	① →	Loading
Test 2	② ←	Unloading
Test 3	② ←	Loading
Test 4	① →	Unloading
Test 5	① →	Loading
Test 6	② ←	Unloading
Test 7	② ←	Loading
Test 8	① →	Unloading

The test results in Fig. G2 show a typical nonlinear load – deflection relationship for consecutive tests conducted with the (a) drive and (b) free end GFBs. The overall behavior of the load – deflection curves seems consistent for each GFB, showing a typical hysteresis loop.

Dividing small changes in static load by the corresponding changes in bearing displacements determines the static stiffness coefficient of the foil bearings. Figure G3 shows the estimated stiffness coefficient versus bearing displacement for tests 2 – 3 and 4 – 5 with the drive and free end GFBs. Irregularly distributed preloads in the GFBs (due to fabrication inaccuracy) may cause very low stiffness around the origin in bearing displacement. Thus, the nominal radial clearances are determined as 40 μm and 70 μm for the drive (c_{DE}) and free (c_{FE}) end GFBs, respectively. With the higher bearing displacements, the support bumps start to react to the applied loads and the stiffness coefficients increase. Note that the zoomed photo of the drive end GFB in Fig. G4 evidences vividly the loose contact of the top foil to the bump strip layers due to fabrication inaccuracy in the radii of curvature of the formed top foil and bump strip layer.

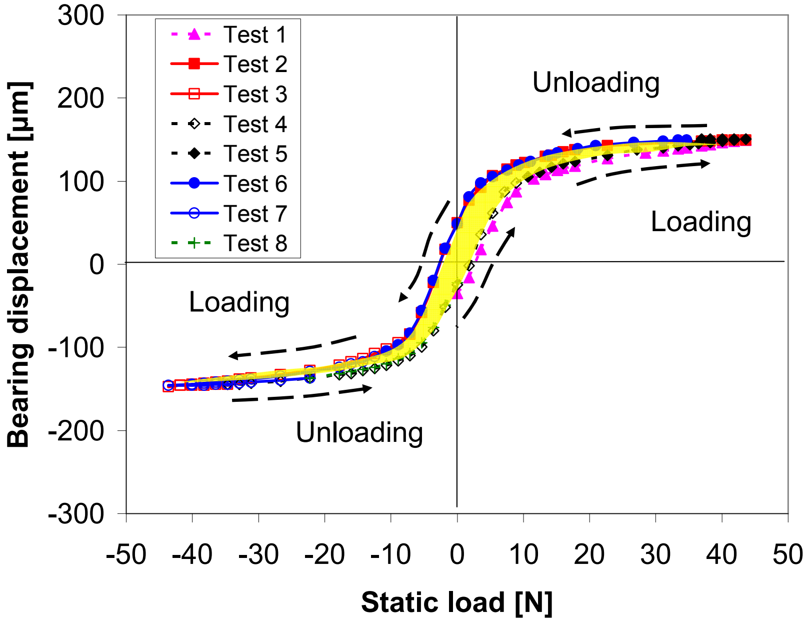

(a) Drive end foil bearing

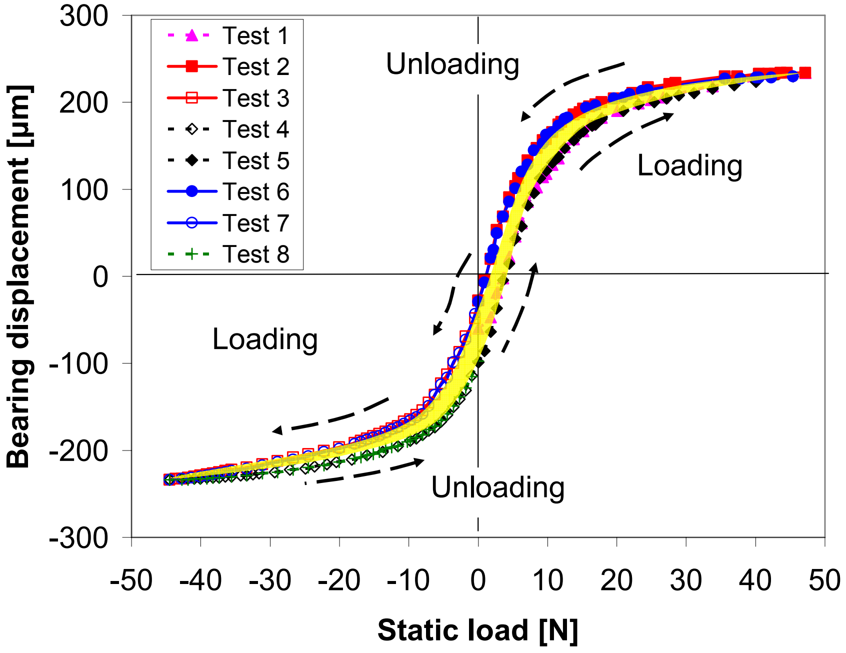

(b) Free end foil bearing

Figure G2 Measured bearing displacement versus static load for eight consecutive loading - unloading tests. (a) Drive end foil bearing, (b) Free end foil bearing. Original GFBs.

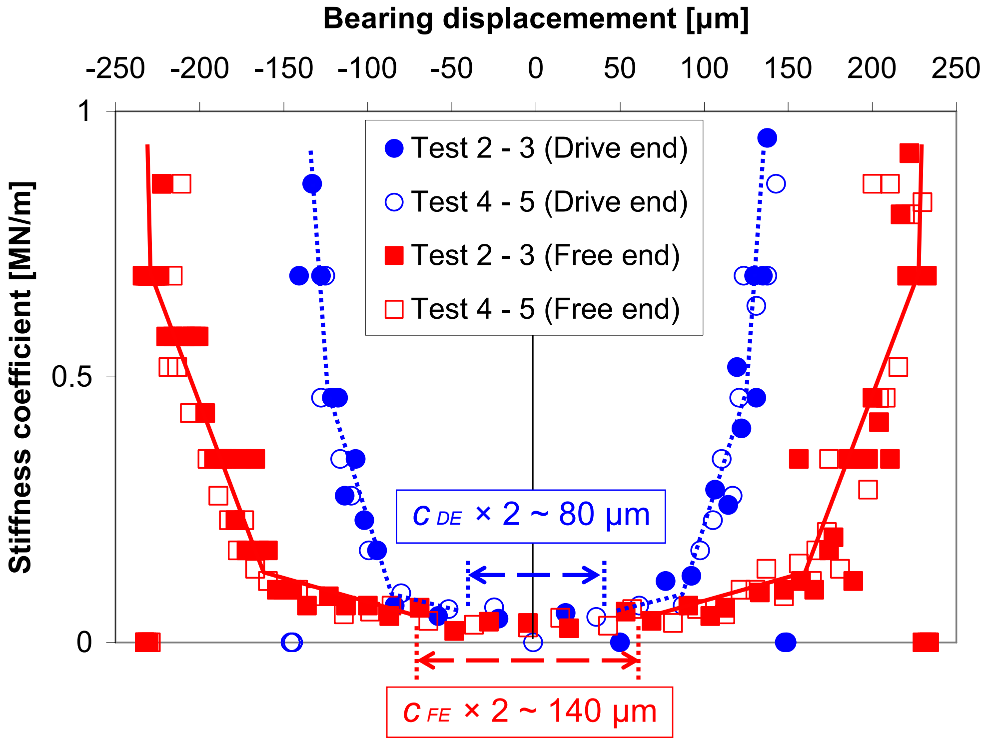

Figure G3 Stiffness coefficient versus bearing displacement for tests 2 – 3 and 4 - 5. Drive and free end bearings. Original GFBs.

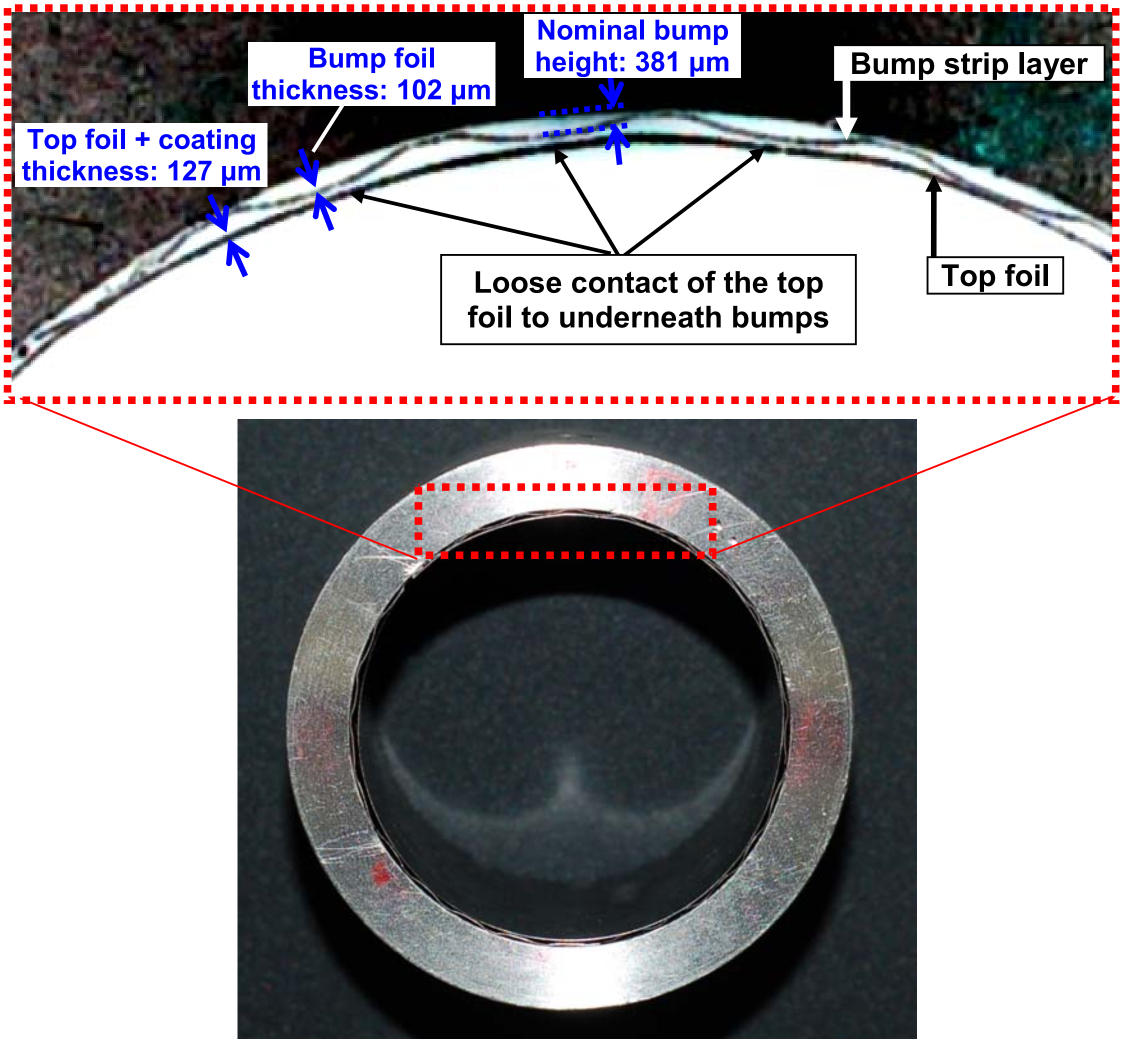

Figure G4 Zoomed photo of test (drive end) GFB. Nominal dimensions of top foil thickness, bump foil thickness, and bump height denoted. Original GFBs.

A static load – deflection test on the flexible coupling aids to estimate its stiffness coefficient. Figures G5 and G6 present the measured coupling displacement versus static load for two different dead weight locations and the estimated stiffness coefficient versus coupling displacement, respectively. Note that the averaged coupling stiffness coefficient of ~1000 N/m is an order of magnitude smaller than the least GFB stiffness coefficient (within the nominal clearance, c_{FE}) of ~ 30,000 N/m.

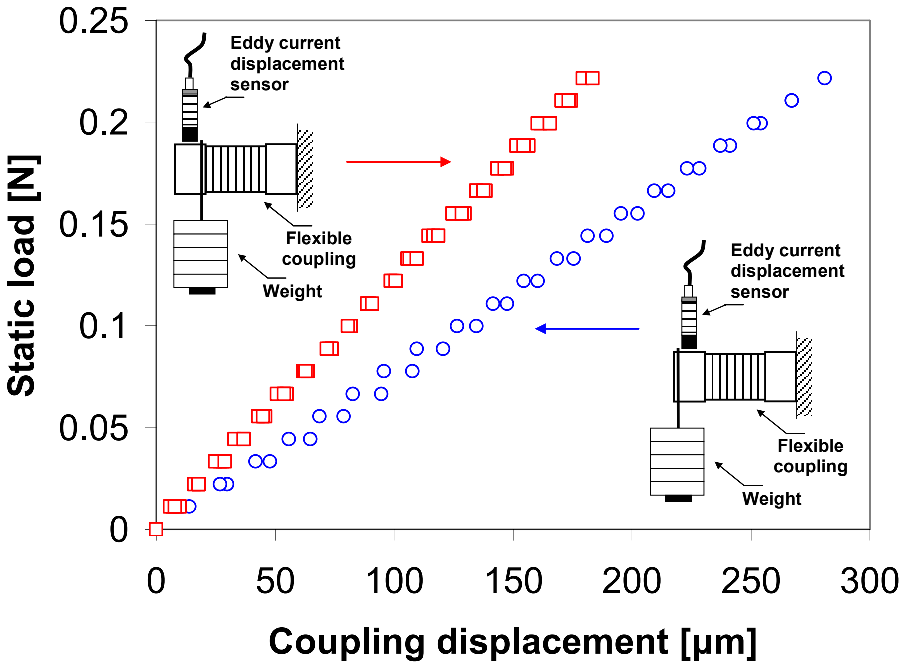

Figure G5 Measured coupling displacement versus static load for two different dead weight locations.

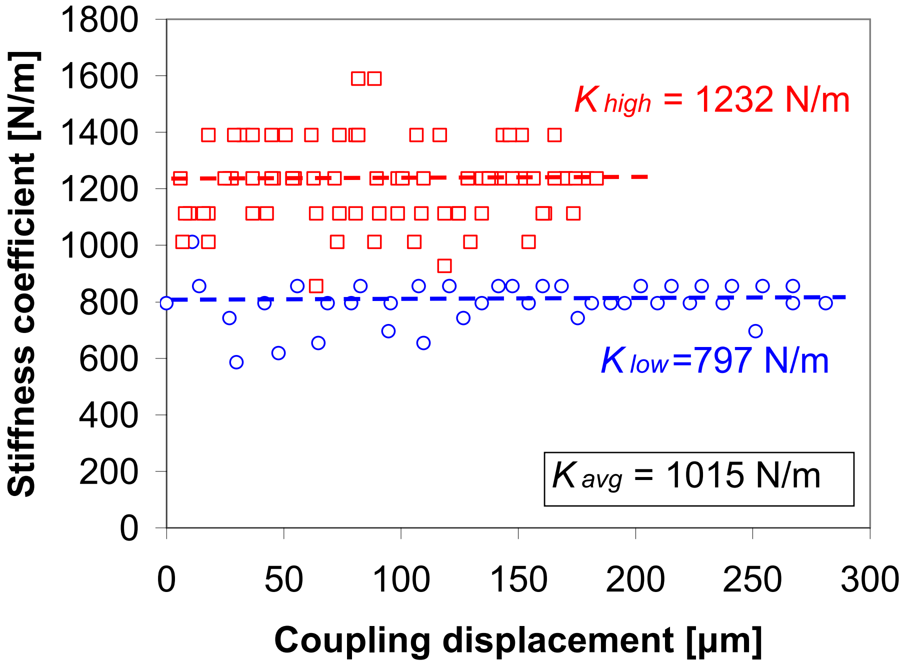

Figure G6 Estimated coupling stiffness coefficient versus coupling displacement for two different dead weight locations.

APPENDIX H

PREDICTED JOURNAL ECCENTRICITY AND ATTITUDE ANGLE VERSUS ROTOR SPEED FOR ORIGINAL AND SHIMMED GFBS: FREE END BEARING

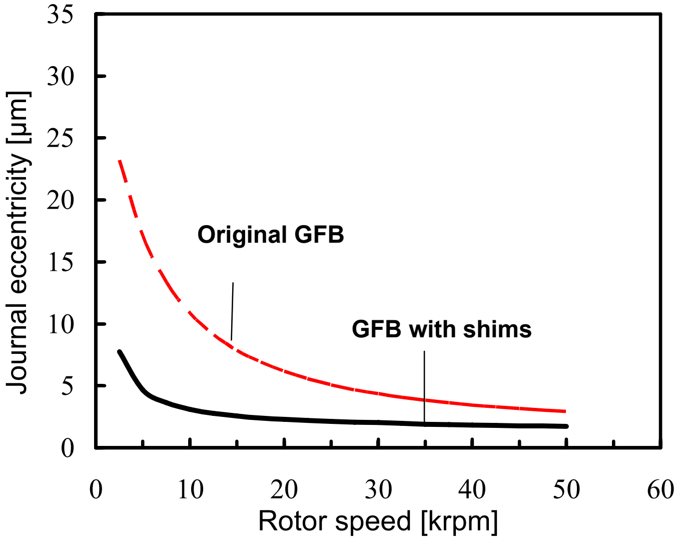

Figure H1 Predicted journal eccentricity versus rotor speed for original and shimmed GFBs. Static load of 6.6 N in vertical (*X*) direction. Free end bearing.

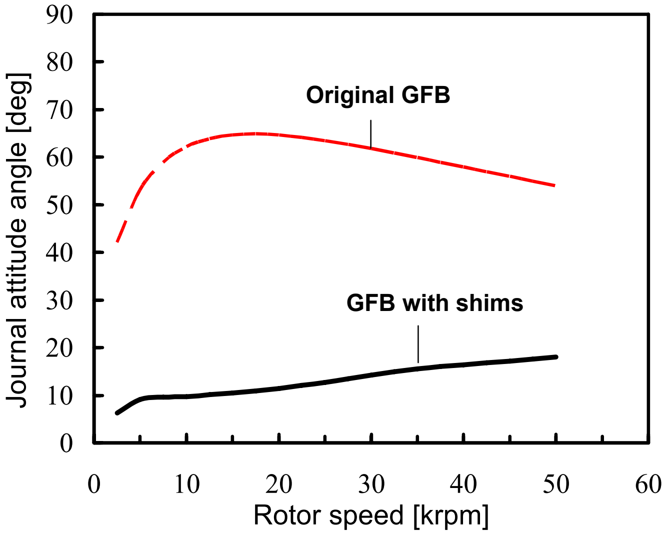

Figure H2 Predicted journal attitude angle versus rotor speed for original and shimmed GFBs. Static load of 6.6 N in vertical (*X*) direction. Free end bearing.

APPENDIX I

PREDICTED STIFFNESS AND DAMPING COEFFICIENTS VERSUS ROTOR SPEED: FREE END BEARING

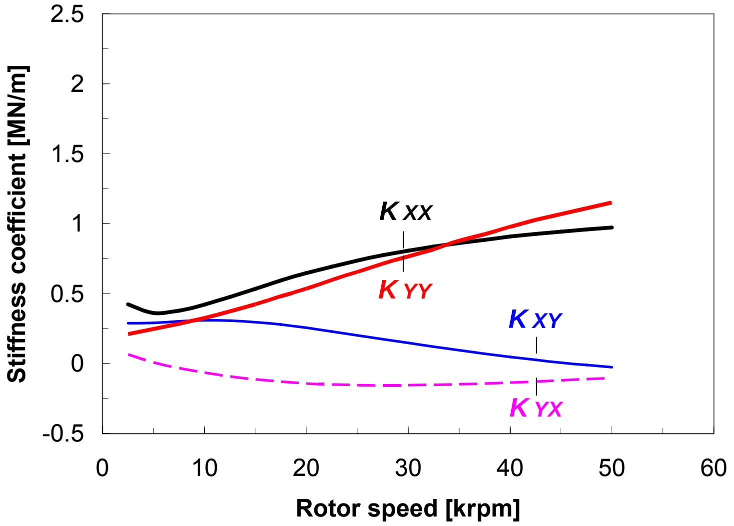

(a) Stiffness coefficients

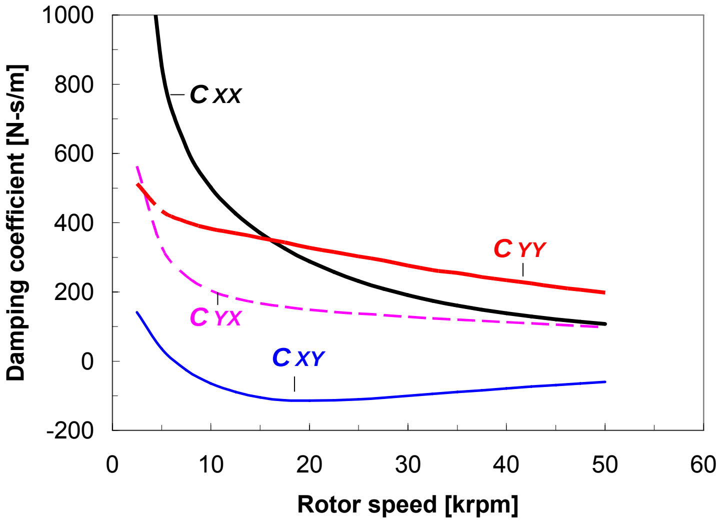

(b) Damping coefficients

Figure I1 Synchronous stiffness and damping coefficients versus rotor speed for original GFBs. Static load of 3.6 N in vertical (*X*) direction. Structural loss factor, $\gamma = 0.2$. Free end bearing.

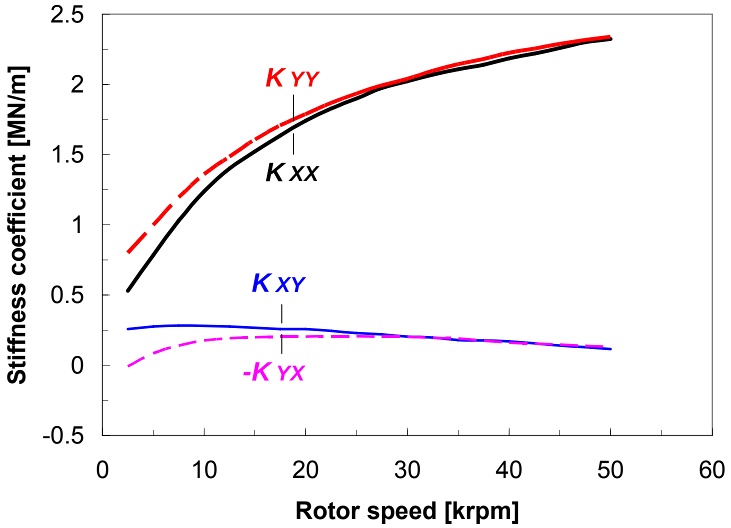

(a) Stiffness coefficients

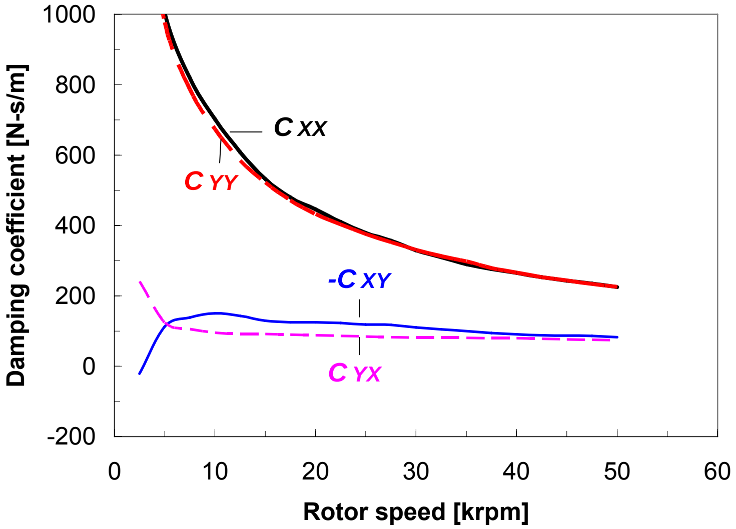

(b) Damping coefficients

Figure I2 Synchronous stiffness and damping coefficients versus rotor speed for GFBs with shims. Static load of 3.6 N in vertical (*X*) direction. Structural loss factor, $\gamma = 0.2$. Free end bearing.

APPENDIX J

COMPARISONS OF PREDICTED SYNCHRONOUS RESPONSES TO TEST MEASUREMENTS: FREE END BEARING

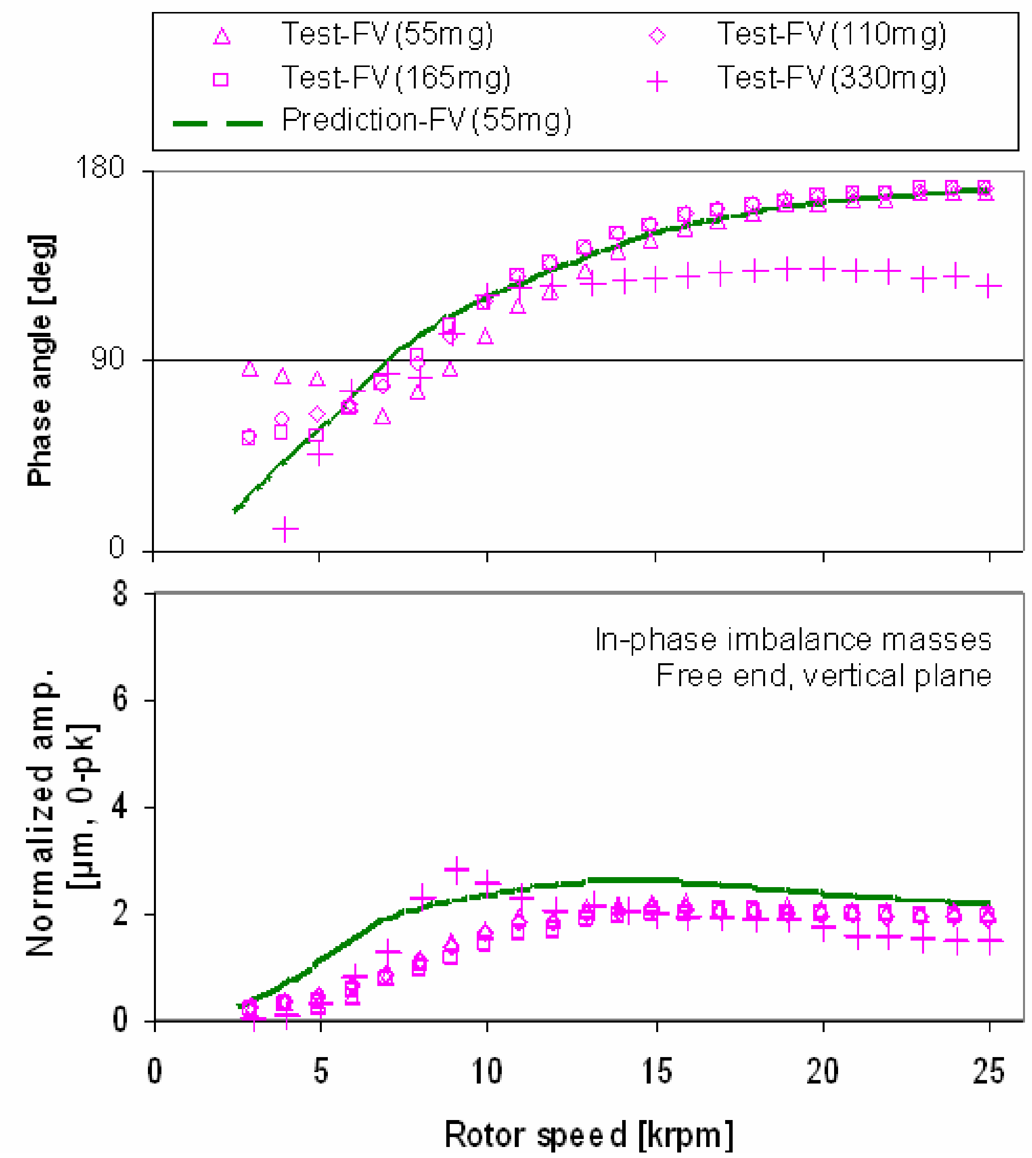

Figure J1 Phase angle and normalized rotor amplitude of synchronous response for increasing in-phase imbalance mass. Free end, vertical plane. Predictions compared to test data. Original GFBs.

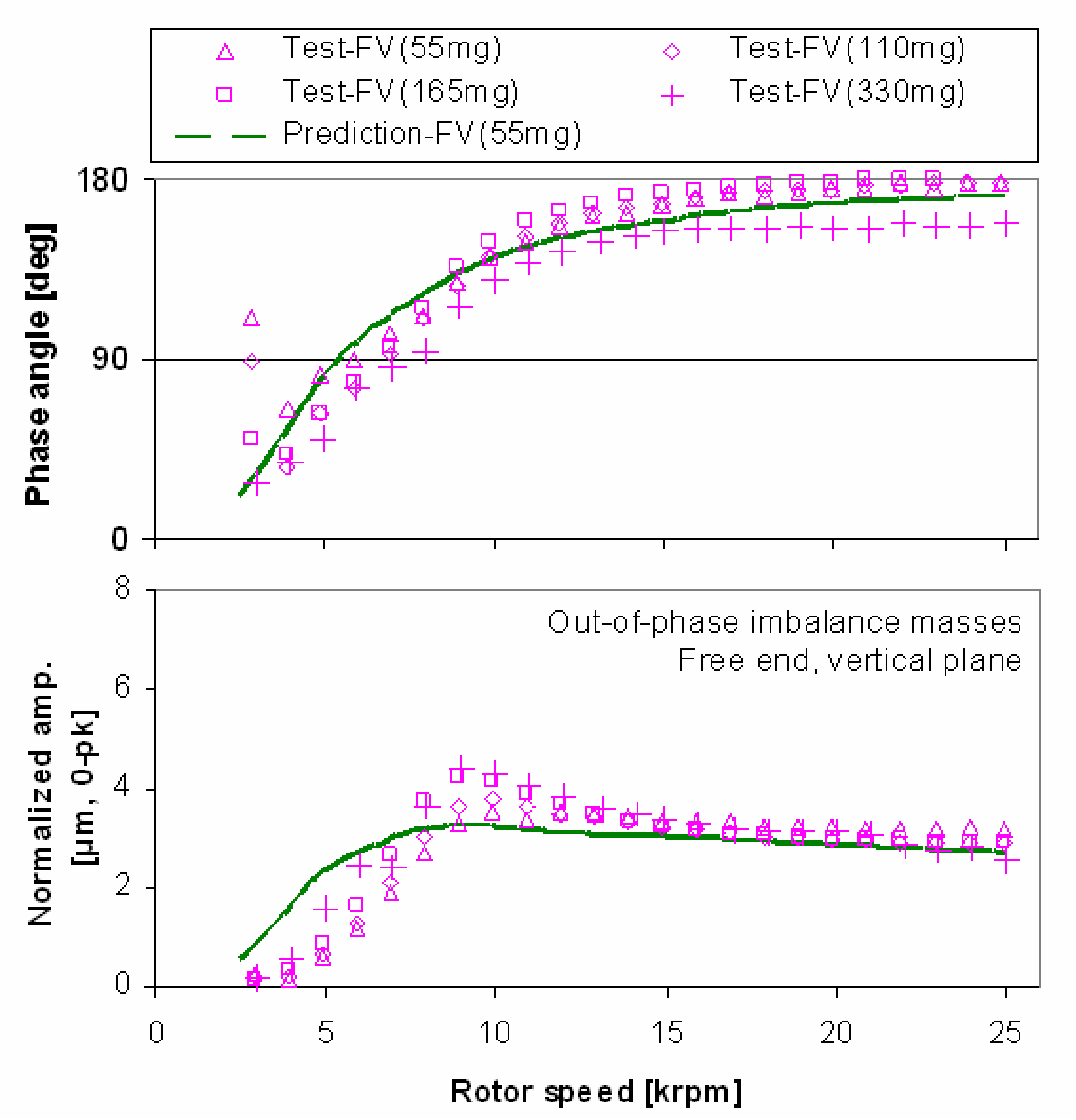

Figure J2 Phase angle and normalized rotor amplitude of synchronous response for increasing out-of-phase imbalance mass. Free end, vertical plane. Predictions compared to test data. Original GFBs.

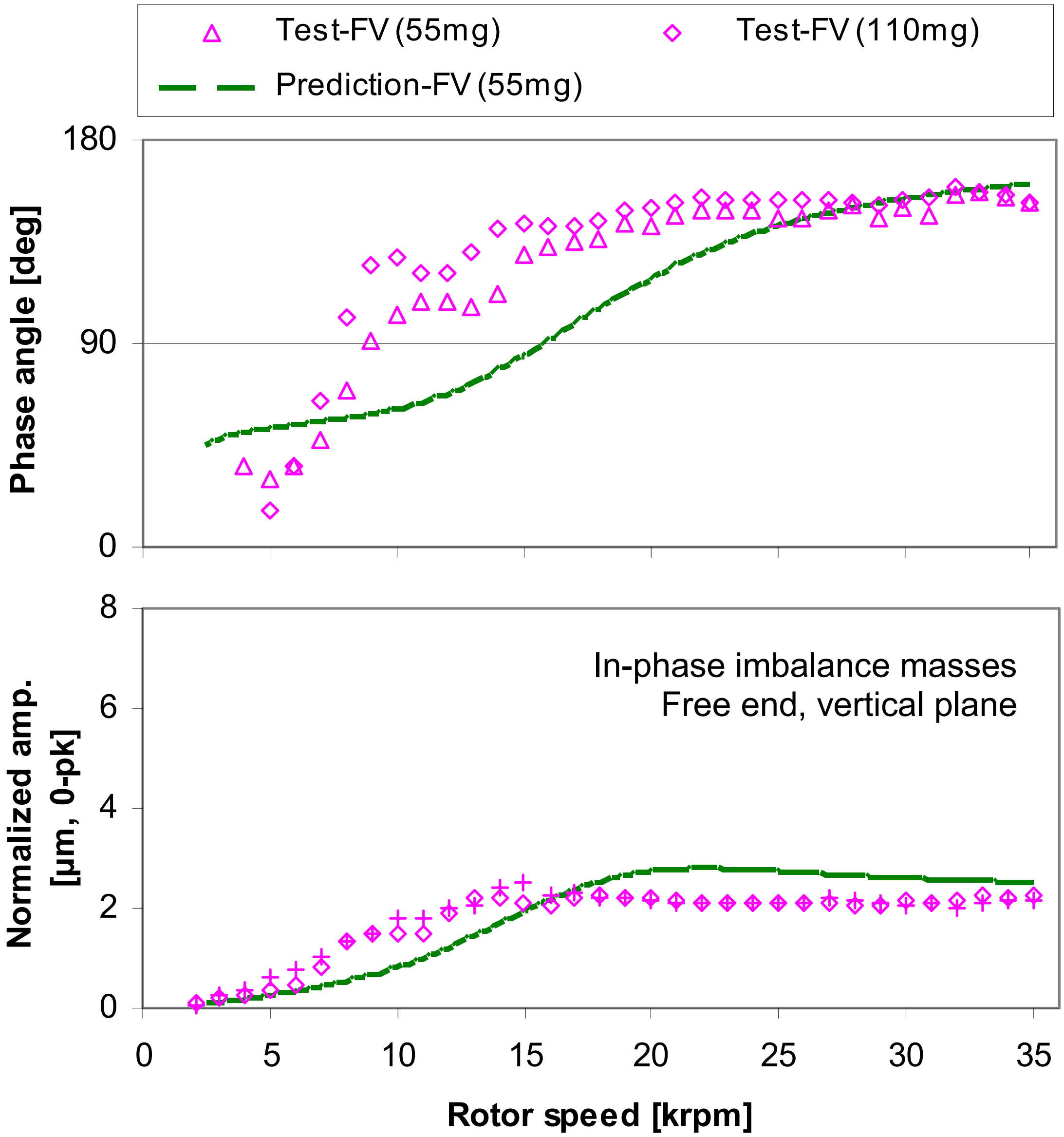

Figure J3 Phase angle and normalized rotor amplitude of synchronous response for increasing in-phase imbalance mass. Free end, vertical plane. Predictions compared to test data. Increased damping coefficients (=2×*C*'s) are used for prediction. GFBs with shims.

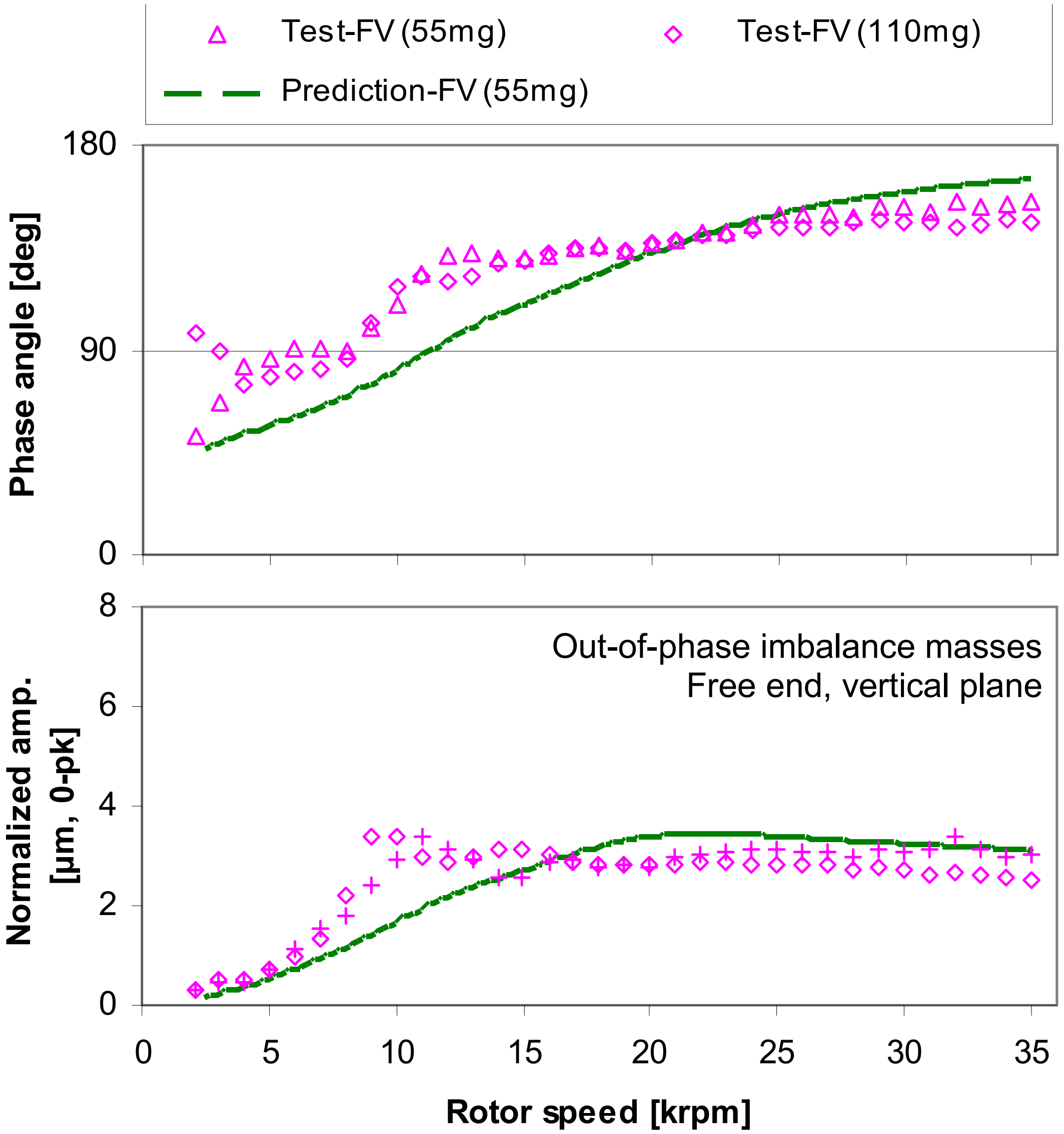

Figure J4 Phase angle and normalized rotor amplitude of synchronous response for increasing out-of-phase imbalance mass. Free end, vertical plane. Predictions compared to test data. Increased damping coefficients (=2×*C*'s) are used for prediction. GFBs with shims.

VITA

Tae Ho Kim was born in Yongin city (Republic of Korea) in 1975. He graduated with his Bachelor of Science degree in mechanical engineering from Hanyang University (Seoul) in 2000, and was subsequently awarded his Master of Science degree by the same university in 2002 for his study of the dynamic characteristics and durability of foil bearings. He was a graduate studying fellow and a commissioned research scientist at the Korea Institute of Science and Technology (KIST) from 1999 to 2003. While there, he spent three and half years working mainly on the development of foil bearings for high speed rotating machinery. In 2003, he moved to the United States to pursue his doctorate at Texas A&M University in College Station, Texas and immediately started working as a graduate research assistant at the Turbomachinery Laboratory under the direction of Dr. Luis San Andrés. Tae Ho's research has focused on the computational physical model of gas foil bearings for oil-free turbomachinery and validation of the rotordynamic predictions by performing experimental tests. He is expected to receive a Doctor of Philosophy in 2007 in mechanical engineering from Texas A&M University. Immediately after completing his Ph.D research, he will begin the next chapter in his academic career as a postdoctoral research associate at Texas A&M University from September of 2007. Tae Ho Kim can be contacted through Texas A&M University's Department of Mechanical Engineering at the following address:

Texas A&M University
Department of Mechanical Engineering
3123 TAMU
College Station, TX 77843-3123